Ultrafast pulse shaping applied to multi-dimensional spectroscopy and novel microscopy methods

By

Miriam Bohlmann Kunz

A dissertation submitted in partial fulfillment of the requirements for the degree of

Doctor of Philosophy

(Chemistry)

At the

UNIVERSITY OF WISCONSIN-MADISON

2022

Date of final oral examination: 08/26/2022

This dissertation is approved by the following members of the Final Oral Committee:
Martin T. Zanni, Professor, Chemistry
J.R. Schmidt, Professor, Chemistry
Michael S. Arnold, Professor, Materials Science and Engineering
Susanna Widicus Weaver, Professor, Chemistry

Abstract

Semiconducting thin films are the building blocks of next generation photovoltaic devices. In many of these devices, energy transfer is necessary for creating a photocurrent from the initially excited electrons. Studying the energy transfer is a difficult task as it happens on the femtosecond to picosecond time scales and between grains that are 10 nanometers to 1 micrometer in diameter and layers that are hundreds of nanometers thick. The tools with both adequate spatial resolution and time resolution to resolve the energy transfer are limited. In this dissertation I will describe the use and development of methods to study the energy transfer within semiconducting thin films.

Three projects are presented. In the first project I use a quartz acousto-optic modulator (AOM) pulse shaper to compensate for the temporal dispersion of a white-light laser pulse. The spectral phase of the pulse is measured with frequency resolved optical gating. In addition, the spatial dispersion of the pulse was measured for different applied temporal dispersions. When the AOM applies a Bragg mask to the pulse, all the light is deflected at the same angle, and there is zero spatial dispersion. The temporal dispersion of the optical path was manipulated so that the acoustic wave needed to correct for the temporal dispersion was nearly identical to the waveform of the Bragg mask. Next, I used the AOM pulse shaper to create the pump-pulse for two-dimensional white-light spectroscopy (2D WL). With 2D WL, I characterized the ultrafast free-carrier thermalization in various lead-halide perovskites. In the last study, I used the AOM pulse shaper to create a pulse-pair for a novel atomic force microscopy (AFM) detected time-domain microscopy experiment, Fourier transform photothermal spectroscopy (FTPT). In FTPT, an AFM tip measures the fast expansion of the sample due to the absorption of light. If the sample absorbs the light from the laser pulse, the energy is conserved mostly through heating of the sample. The increase in temperature causes the sample to expand. Using the AFM tip as the detection method

yields sub-diffraction limit spatial resolution that is not possible for optically detected microscopy. Combining FTPT with an ultrafast pump pulse could allow for measurements with ultrafast time resolution and nanoscale spatial resolution to an extent that has not yet been achieved.

Acknowledgments

I could never have imagined how much I would enjoy my time as a graduate student living in Madison. With all that joy, there were also many ups and downs. It is thanks to the following people that this degree has been possible, by bringing positivity to the difficult times in lab and new perspective to solving the many problems.

First, I must start with thanking my advisor, Marty Zanni. I am so grateful for the many ways you have helped me become a better scientist. Thank you for the opportunity to work in a lab with the resources necessary for the crazy work of multi-dimensional spectroscopy. Both the physical resources, but also your wealth of knowledge and impeccable scientific intuition. I appreciate that you maintained an environment where I felt comfortable asking you questions, no matter how fundamental. I'm especially grateful for all you do to make the members of your group better scientific communicators and writers. Not only have I come away from this group an expert in multi-dimensional spectroscopy, but you have taught us to sell our science and to tell a story.

Thank you to my committee, Professors JR Schmidt, Michael Arnold, and Susanna Widicus Weaver. The feedback and guidance I have received from you over the past five years has given me much needed perspective on my work and made me a better scientist.

I have to thank all of the teachers who have helped me get to this point, especially the ones who pushed me academically and also helped me grow as a person. My 2nd/3rd grade teacher Mr. Lyons and my 4th/5th grade teacher Mrs. Hammerschmidt who went out of their way to push me in mathematics. My high school English teacher Ms. Brewster, who helped teach me to read critically and apply for the schools of my dreams. Ms. Moore, whose Women and Gender class better prepared me for college and what would come next in life better than any science or math class I ever took.

Next, I have to thank Professor Emily Weiss, Dr. Ken Aruda and the rest of the Weiss Group at Northwestern University. Emily gave me my first opportunity to do science research. She was generous with her time and resources and taught me how to organize a larger experiment and set high standards for research. Ken was a great mentor and teacher, and gave me my first taste of multi-dimensional spectroscopy. I'm grateful for his mentorship both in lab and in preparing for graduate school.

There are countless people to thank at UW-Madison and in the Chemistry Department that make all of this crazy research possible. Those who served as Chair during my time, and had to deal with multiple issues to keep our building running, Professors Judith Burstyn and Clark Landis. Jeff Nielsen, our building manager, who is the most important person to have as a friend in the entire department. Nothing gets done without Jeff and the countless hours he devotes to our work. The administrative folks who have helped me navigate graduate school, the absolute bomb.com Mary Hanson, Cheri Stephens, Arrietta Clauss, and Taylor Mathewson. The staff in the machine shop who make our home-built experiments possible, Steve Myers, Kendall Schneider, and Blaise Thompson.

Of course, the NSF-GRFP program afforded me the time to do this research, as well the NSF and AFOSR for funding the research I got to undertake.

I had the opportunity to work with many great people in the Zanni Group. Michal Maj and Justin Lomont were great examples of what it meant to be part of the Zanni Group: hard workers who knew how to also have fun. I'm grateful for their kindness during my first year. Kacie Rich, who did so much for the lab in terms of culture, both socially and safety wise, so that even though we never worked together, I can still call her a good friend to this day.

I was lucky to have two amazing mentors, Nick Kearns and Andy Jones. Nick, thank you so much for your gentle teaching of optics and spectroscopy. Your calmness and encouragement made me feel comfortable from my first day in lab. After five years of doing spectroscopy, I am even more amazed by what you achieved in this group. I'm grateful for your LabView programs, which I kept learning from long after you had left. I was sad to see your expertise and dark sense of humor leave, but am so grateful for the foundation you built amongst the materials side of the group. Andy, you taught me so much about being a good scientist every single day, the importance of paying attention to the littlest details, but also maintaining perspective. You are such a creative scientist and a good teacher, which is why you are such a great mentor. But most importantly, you were a kind and supportive mentor, and have continued to be. I can never thank you enough for your time and generosity.

I got to overlap in the Zanni Group with four all-star senior graduate students. Josh, you are such a great teacher and kind human. You taught me so much about spectroscopy and made me feel like a valued person in the group anytime you asked me for advice, even as a first-year. You were a great teacher of humility, as you are maybe the smartest person I have ever met, but you would deny it to the end. What can I say, you'll always be a legend in your field. Ariel, you taught me what it means to be a well-rounded scientist. I learned so much from you during journal and lit clubs, and you are someone who always was engaging and asking questions, which is an example I have tried to follow. I love that you are ambitious and a hard-worker, but always do your best to bring lightness to your work place, either with a laugh or a dance move. I'm so excited to see how you change the world as a professor and mentor. Megan, you were maybe my favorite person to bounce ideas off. I admired your curiosity across so many fields and your breadth of knowledge. You asked the hardest questions and therefore made me and everyone else in the group

better scientist, and you made sure that the group had the proper pop culture IQ. Thanks for being a good coworker and great friend. The last of the senior graduate students, Jessi. I'm so grateful that we got the chance to work together on the perovskites. I got to see just how much of a baller you were, mastering the fabrication in another country. You were always down for a new challenge in the lab either learning a new fabrication or wrestling a laser, or in life moving to a new country or picking up a new sport. Thank you for sharing your wealth of knowledge with me, for being the best dog sitter we've ever had, and for being an all-around amazing person who made graduate school better.

To the junior graduate students in the Zanni group, thank you for teaching me so much as well. Sid, the energy you bring to the office every day has made working in the Zanni Group a pleasure. I love that you're down to talk science with me even though we work on such different things. Ryan, teaching you your first summer really helped me understand our spectroscopy in a way I hadn't before. You're always down to talk through a problem and ask the tough questions that really take some thinking through. And I appreciate that you have kept your wet labs skills up brewing beer, even though you live in that laser lab. Kieran, I have learned so much from you about spectroscopy, both experimentally and theoretically. I have had so much fun talking about the most ridiculous ideas of how you could use a pulse shaper, but in the process actually solving a problem as well. You're also always down for some JDen and a laugh, which I greatly appreciate. I'm so excited for all three of you and whatever comes next.

Matt, you're such a diligent worker and smart, which is a winning combination. I'm grateful for your dark sense of humor, and I regret we didn't get to work together more. You're a great student and coworker. Yuzhe and Zac, it has been a great honor to mentor both of you to different extents. Yuzhe, from day one I've been amazed with how quickly you learn the optical

setup and how focused you are on achieving your goals. Not mention you have been very kind and respectful along the way. Zac, I think you have taught me just as much as I have taught you. Thank you for your help during the final months of my PhD, it was really fun to combine our strengths to solve some problems. The amount that I've gotten to see you grow as a scientist even in the last 6 months tells me that you are going to do great things as a graduate student, and to top it all off you have a genuine interest and appreciation for the people in this group that I really admire. I'm excited to see what is in store for both you and Yuzhe.

Yulia, I'm grateful for our time together on the 4th floor. I will miss the random pop culture knowledge you teach me and I'm afraid I will be very out of touch with gen z because of it. Thanks for your support and friendship, and I'm excited to see what you do next as a scientist, because you're crazy smart.

To my cohort of Zanni Group members, Erin and Cat. I don't think any of us would have survived the last five years without the support of each other. You both have taught me so much about being a consistent scientist and good coworker. Cat, we worked on such different things, but you were a great person to share tribulations of research and life with. Our coffee breaks kept me sane at many points. Erin, you were the best office mate, always down to discuss the finer points of spectroscopy that we both felt we should have understood. Thank you for sharing an enthusiasm for trivia and millennial pop culture, and for holding all your coworkers to the highest standards. Erin and Cat, you made the people around you better scientists and thank you both for your friendship.

Zach, thanks for being the best partner is science crime a person could ask for. My favorite times in graduate school have been sitting in the office reasoning through some bit of spectroscopy on the chalk board with you and whoever else is around. You have such a breadth of knowledge

and also the ability to understand deeply. Thank you for sharing some of that knowledge with me and teaching me the past four years. More importantly, thank you for the many beers and backyard hangs that make it so very hard to leave.

I also must thank the many friends in Chemistry Department that have made this a place I enjoy coming to work and am proud to be a part of. My roommates Ceci and Lydia, many teammates on various sports team such as Hammersonly.com, Bucky Balls, and Yellow Bananas. The wonderful hockey teams that made winter in Madison not only tolerable, but my favorite time of the year, UWC and MGHA. Thank you to all my Madison friends who have been understanding and supportive of my pursuit of this degree.

Lastly, I have to thank my family whose unconditional love and support is all I've ever known. My Grandpa Mel, I've so much enjoyed being able to share this love of physical sciences with you. Knowing that a love for science is something that we share has motivated me when sometimes I didn't love science quite as much. All the Bohlmann's and Kunz's who have supported my education throughout the years and opened their homes to me when that education has taken me to new places. My brothers, John and Adam, it was competition with you that first convinced me I wanted to be a chemist, but your support has sustained me well past the point that I cared about any competition. Hayden and Athena, your interest and curiosity has motivated me to make sure that science is accessible to all, regardless of age, race or gender. And of course my parents, Michael and Deborah, none of this is possible without your love and support.

Lastly, I have to thank my partner, Lindsay. These last three years have been unprecedented, but thanks to you and our family they have been the best three years of my life. This dissertation does not get written without your help and support. Let's go kick some science ass in Pittsburgh.

Table of Contents

List of Figures

List of Tables

1. Introduction

1.1 Motivation

In my research I have been interested in semiconducting materials that have applications to photovoltaics. In a photovoltaic device, there are typically many layers of semiconductors, including a photoactive layer that generates an excited electron-hole pair from the incoming light, and donor or acceptor layers to separate or transport the excited electron or hole. The transfer of energy within and between these semiconducting layers is crucial to photovoltaic device efficiency; there can be no electricity created if the excited charges are stuck in place where they are excited.[1] The focus of my research has been developing and utilizing methods to study energy transfer within and between semiconducting thin films.

There are many exciting new materials with potential for photovoltaic applications, such as lead-halide perovskites (Chapter 4),[2] organic photovoltaics,[3] and a further class of organic photovoltaics: singlet fission materials.[4] An advantage of all these materials is the process for making them is much simpler than that of traditional silicon devices. Lead-halide perovskites and organic photovoltaic thin films can be solution processable.[5–7] The thin films, both the solution processable organics and perovskites, and films of polycrystalline silicon, are made up of small grains, that can be tens of nanometers to micrometers in size.[1,6,8,9]

Grain boundaries and the differences in electronic structure between grains are difficult to characterize due to their small size. Many techniques such as scanning probe microscopies and electron-beam microscopies can provide structural information on the nanoscale,[6,9] but in few cases is spectroscopic information that can provide information on the electronic structure also

accessible.[10,11] Conversely, almost all spectroscopic techniques are limited in their spatial resolution by the diffraction-limit of light.[12–14] The diffraction-limit for visible wavelengths of light, which is the region of the electromagnetic spectrum that is most relevant for photovoltaic materials, is approximately 200-300 nm. One of the methods I discuss is two-dimensional electronic spectroscopy (2DES). 2DES can measure energy transfer in semiconducting thin films, but the best spatial resolution that has been achieved with 2DES is 1 μm.[15,16] For a film that has grains that are on the order of 100 nm in diameter, 1 μm spatial resolution is insufficient for direct measurement of the heterogeneity of the sample. With the combination of atomic force microscopy and an ultrafast white-light laser pulse pair, I circumvented the constraints of the diffraction-limit to measure linear absorption spectra with 50 nm spatial resolution. I developed this method, Fourier transform photothermal spectroscopy (FTPT), as a tool to study the heterogeneity of semiconducting thin films, with the goal of extending the method to measure energy transfer between individual grains via non-linear spectroscopy with sub-diffraction limit spatial resolution.

In this introduction, I will give the relevant background information on linear and non-linear spectroscopy. Then, I will describe the concept and implementation of pulse-shaping for broadband pulses. I will then describe atomic force microscopy and how it can be used in combination with pulse-shaping for FTPT. Lastly, I will give a summary of the projects in the following chapters.

1.2 Linear absorption spectroscopy

1.2.1 Applications of linear absorption spectroscopy

The linear absorption spectrum of a molecule in the visible and ultraviolent wavelength range represents the energy needed for an electron to be excited from a ground electronic state to an excited electronic state.[17] For semiconductors, the electron is promoted from a valence band to

a conduction band, as shown in Figure 1.1. The smallest energy difference between these two bands is defined as the bandgap, which is an important material characteristic as it determines what part of the solar spectrum can be used to convert light into electricity in a photovoltaic device, and sets the maximum efficiency of converting light from the sun into electricity.[18]

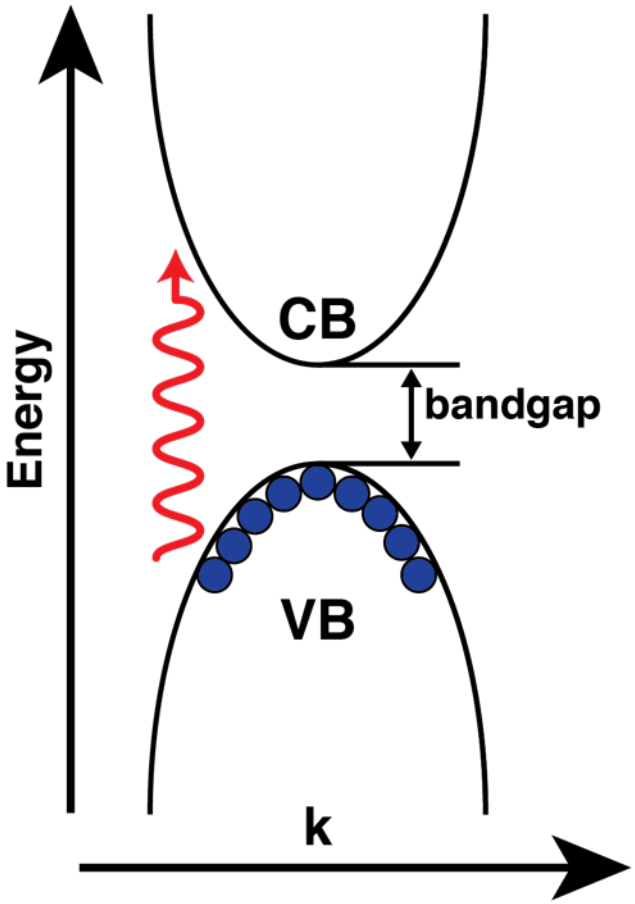

Figure 1.1 A simplified band diagram for a semiconductor showing the valence band (VB) and conduction band (CB). If the energy of the light is larger than the bandgap, electrons can be excited from the valence band to the conduction band.

In addition to the bandgap, the linear absorption spectrum can give insight to the electronic coupling between molecules.[19] In the molecular picture, if two molecular orbitals are overlapped to some extent, the two molecular orbitals can couple together. The coupling causes the energies to split and the intensity of the peaks to vary depending on the strength and orientation of the

interaction.[20] For example, previous work in the Zanni Group showed that slight shifts in the packing of TIPS-pentacene (6,13-bis(triisopropylsilylethynyl)pentacene, TIPS-Pn) microcrystals causes significant changes to the coupling between the molecules. The changes to the coupling were observed spectroscopically with 2DES and transient absorption spectroscopy,[15,21] but the new peak assigned to the change in coupling was observed in a spectrum that has the same transition dipole dependence (μ^2) as linear absorption spectroscopy.

1.2.2 Frequency vs. time-domain

The linear absorption spectrum is a straightforward concept: it represents how much light is absorbed by a material at a given wavelength. The equation to communicate this is:

$$A(\lambda) = -log\frac{I(\lambda)}{I_0(\lambda)} \tag{1.1}$$

Where A is the absorption, I is the intensity of light after the sample, and I_0 is the intensity of light before the sample. To measure the absorption spectrum, the intensity of light before the sample and after the sample must be known as a function of wavelength. Measuring these two quantities can be implemented experimentally in a variety of ways, both in the method of determining absorption as a function of frequency (wavelength) and in the method of detection.

The two methods of determining the absorption as a function of frequency are the frequency and the time-domain. In the frequency-domain, the absorption is directly measured as a function of frequency. One method for frequency-domain linear absorption spectroscopy is to use a light source that is narrow in bandwidth and the frequency of the light source is scanned.[22] The intensity of the light can be measured with and without the sample present at each frequency. A second method of frequency-domain linear absorption spectroscopy is to use a broadband light source and after the sample disperse the light with a diffraction grating. After the light is dispersed in the frequency domain, it can be focused onto a line scan camera so that the intensity at each frequency

is measured simultaneously, or the grating can be rotated so that the intensity of each frequency in turn is measured on a single-pixel detector. In the frequency-domain, the only data processing necessary to retrieve the absorption spectrum is to plug the intensities of light before and after the sample into equation 1.1. Frequency-domain linear absorption spectroscopy is the most common method used by commercial UV-vis spectrometers.

In time-domain linear absorption spectroscopy, instead of scanning the frequency of the light source, the time between two laser pulses is scanned.[23] Since time is the Fourier inverse of frequency, the time-domain signal can be Fourier transformed to retrieve the spectrum. For a full description and derivation of the linear (and two-dimensional) signal in the time-domain, I would refer the reader to Hamm and Zanni (Cambridge Univ. Press), whose notation I will use throughout this dissertation.[20] In summary, the first laser pulse excites the sample into a coherence. Once in the coherence, the sample returns to a population state and emits the signal field. The signal field interferes with the second laser pulse, called the local oscillator. The local oscillator is measured, and the interference of the local oscillator and the emitted signal oscillates and decays as the time between the first laser pulse and the local oscillator is increased. The equation for the detected signal in the time-domain is:

$$S(t) \propto I_0 e^{it(\omega_c - \omega_{ge})} e^{i(+\phi_1 - \phi_2)} {\mu_{ge}}^2 \tag{1.2}$$

Where t is the time between the pulses, called the coherence time, ω_c is the carrier frequency of the electric field, ω_{ge} is the frequency corresponding to the transition from the ground to the excited state, ϕ_n is the phase of the pulse, and μ_{ge} is the magnitude of the transition dipole from the ground to the excited state. The signal as a function of the frequency is then

$$S(\omega) = \int_0^\infty S(t) e^{i\omega t} dt \tag{1.3}$$

The signal in the time-domain is called a free-induction decay (FID), an example of which is shown in Figure 1.2a. A common linear time-domain experiment is Fourier transform infrared (FTIR) spectroscopy.[24]

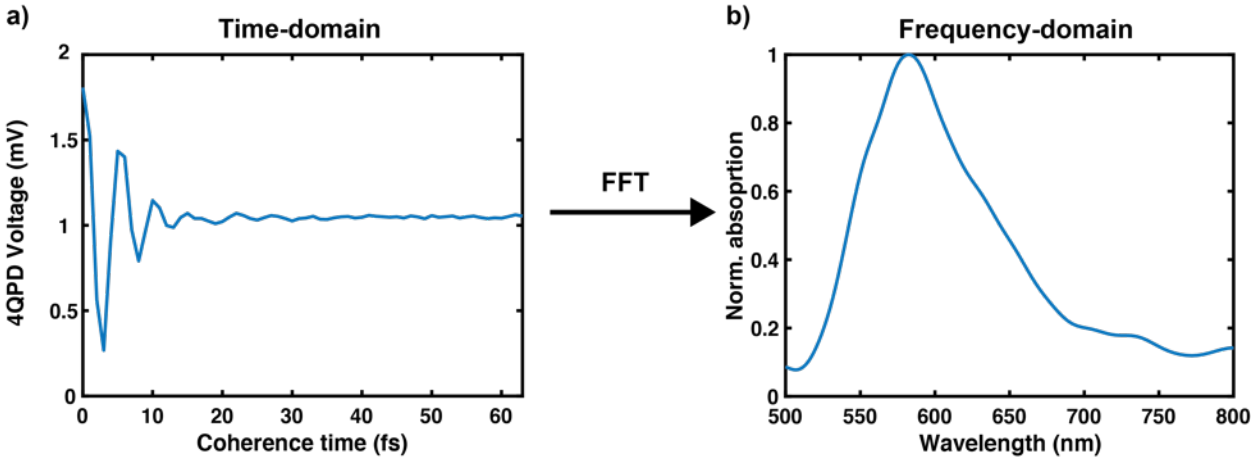

Figure 1.2. An example FID measured via Fourier transform photothermal spectroscopy is shown in (a). An FID is a time-domain measurement that can be Fourier transformed to retrieve the spectrum in the frequency-domain (b).

1.2.3 Optical vs. action detection

The second experimental condition that I will consider is the method of detecting the signal. Traditional spectroscopy methods measure the light transmitted through the sample, which will be called optical detection. For a frequency-domain experiment, optical detection can be done with either a single-pixel photodetector or a line scan camera if using a broadband source.[17] For visible light, the detectors are generally made from silicon, as silicon has a bandgap at 1100 nm.[1] Detectors for the near infrared are often made from InGaAs,[25] which has a bandgap near 1650 nm.[26]

An alternative to optical detection is action detection. Action detection measures some secondary event that is a result of the absorption of light. The most common methods of action detected spectroscopy are photocurrent,[27,28] fluorescence,[29] and photothermal.[30] The relation between the action and the magnitude of light absorbed must be known to retrieve an absorption spectrum from an action measurement. In addition, any light that is absorbed but does not

contribute to the action is not accounted for. Using photocurrent as an example, if a sample absorbs light and the excited charge becomes trapped in a defect state that can then not be transported to an electrode, that absorbed light will not contribute to the measured photocurrent. The efficiency of photovoltaic cells at converting absorbed light to current is one method of benchmarking photovoltaic cells.[6] For photothermal measurements, which is the action detection method used in Chapter 5, any light that decays radiatively and does not decay via vibrations or phonons heating the crystal will not contribute to the photothermal signal.

Action detected measurements can be conducted in either the frequency or time-domain. However, the action detection essentially functions as a single-pixel detector, so if the experiment is done in the frequency-domain, a narrowband source is required.

1.3 Two-dimensional spectroscopy

Two-dimensional spectroscopy can provide the same insight to a materials electronic structure as linear spectroscopy but has the added advantages of time resolution and correlation between a pump and a probe frequency. The correlation between pump and probe can provide further information on coupling within the material and the energy transfer between states.[31,32] Three or four ultrafast (~40 fs) pulses are used in a 2D experiment, which by scanning the time between the second and third laser pulse (waiting time, t_2) can give kinetic information on the energy transfer within a material with sub-100 fs time resolution.[33,34] This time resolution is fast enough to resolve hot-carrier cooling in lead-halide perovskite thin films (Chapter 4), singlet fission in organic microcrystals,[15,21] and energy transfer in semiconducting carbon nanotube thin films.[25]

1.3.1 Interpreting 2D spectra

One way to think about 2D spectroscopy is to start from the framework of transient absorption (TA). For a transient absorption experiment, there are two laser pulses, the pump and the probe. The pump pulse excites the system, and the probe pulse measures that state of the excited system some specified amount of time after the pump. Transient data is plotted as differential absorption: the absorption spectrum from the probe pulse going through the sample is measured in the pump-on case and the pump-off case. The pump-off case is subtracted from the pump-on case so that the differential absorption can be expressed as:

$$\Delta OD = -log \frac{I_{pump-on}}{I_{pump-off}} \tag{1.4}$$

Where $I_{pump-on/off}$ is the wavelength dependent intensity of the probe with the pump on or off. Most transient signals are on the order of 0.1-10 mOD, or 100 to 10,000 times smaller than a linear signal. Conveniently, the light source used for the laser pulses operates at 100 kHz for all the experiments in this dissertation,[35] which allows averaging of thousands of transient spectra in one second to achieve adequate signal-to-noise.

There are three general features that can contribute to a TA spectrum. The first is a ground state bleach (GSB). GSB occurs when the pump excites an electron and there is then decreased absorption of the probe light due to the decrease in the number of possible electrons that can be excited. GSB appears as a negative signal in a TA spectrum as more probe light is transmitted through the sample when the pump is on. The second feature is stimulated emission (SE). SE occurs when the excited electron returns to the ground state, emitting light in the process due to the interaction with the probe pulse. Since additional light is emitted due to the excitation from the pump pulse, SE also appears as a negative signal in a TA spectrum. The third feature is excited state absorption (ESA). ESA occurs when the pump excites an electron, and then the probe further excites the electron to a high lying state. ESA appears as a positive feature in a TA spectrum, as

there is additional absorption of the probe light due to the excited electron from the pump pulse. Example Feynman diagrams and energy level diagrams for the three pathways are shown in Figure 1.3. In the time between the pump and probe pulses, the excited system can evolve. The excited electron can recombine, which would decrease the intensity of any transient feature. The excited electron or corresponding hole can move to another state. The electron in this newly occupied state can then have new SE or ESA.

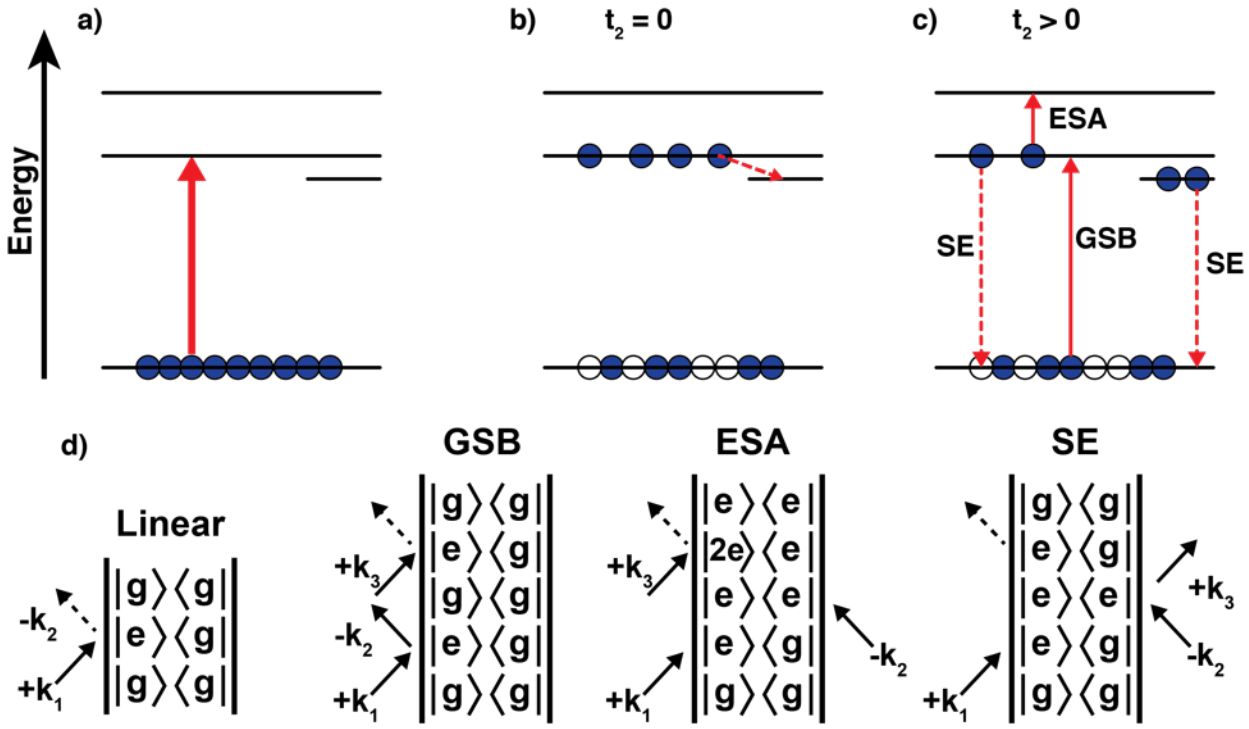

Figure 1.3. Demonstrates an example of transitions that can happen in a TA or 2DES experiment. The solid lines correspond to light being absorbed and dashed lines correspond to light being emitted. a) shows the system with all the electron (blue circles) in the ground state, and when the pump pulse arrives, some of those electrons can be promoted to an excited state, shown in b), leaving holes (white circles) in the ground electronic state. Once excited, the electrons can remain in the same state or move to other energy states before the probe pulse arrives. When the probe pulse arrives, shown in c), additional electrons can be promoted to the excited state, but now there are fewer electrons that can be excited, which results in a ground state bleach (GSB). The electrons that are in excited states can radiatively decay back to the ground state by stimulated emission (SE), or the excited electrons can be promoted to an even higher energy state (ESA). Example Feynman diagrams d) are also shown for the different types of pathways.

The same three features that are present in TA spectra are also present in 2D spectra. TA can be done with a pump pulse that is either narrow[36–38] or broad in bandwidth.[21,39] Narrow band pump TA provides information on the system of interest corresponding to a single pump excitation. Broad band TA is equivalent to summing the narrow band spectra for a continuum of pump wavelengths. One way to imagine a 2D spectrum is many narrow band TA spectra plotted together. An example 2D spectrum is shown in Figure 1.4. For all the 2D spectra plotted in this dissertation, the pump wavelength is plotted on the Y-axis and the probe wavelength is plotted on the X-axis. In the example in Figure 1.4, a film of methylammonium lead iodide is measured with a delay of 300 fs between the pump and the probe. The blue negative feature seen at the probe wavelength of 750 nm is the GSB and SE emission at the bandgap of the perovskite. That the peak is seen at all pump wavelengths means that within the first 300 fs any electrons and holes excited above the bandgap relax down to the band edge. The red positive feature at shorter probe wavelengths (higher energy) than the GSB is an ESA. The ESA corresponds to the electrons at the band edge being excited to a higher lying band.

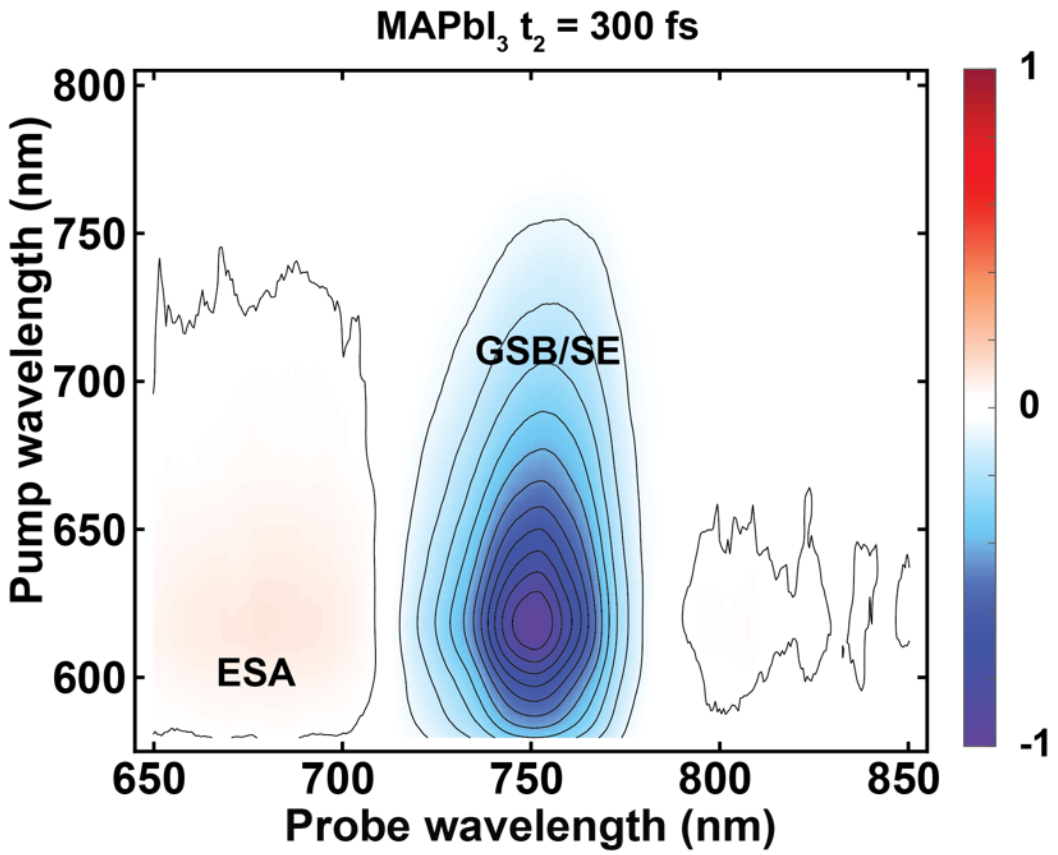

Figure 1.4. An example 2D spectrum of $MAPbI_3$ at a waiting time of 300 fs. The large blue feature corresponds to GSB and SE from excited carriers relaxing to the bandgap within the first 300 fs, and the red ESA feature corresponds to the carriers at the band edge being excited to a higher lying band.

1.3.2 Experimental considerations for 2D spectroscopy

Frequency vs. time-domain

Transition from TA spectroscopy to 2D spectroscopy requires an experimental method for resolving the pump frequencies. Just like linear absorption spectroscopy, 2D spectroscopy can be done in either the frequency-domain[40] or the time-domain.[41] 2D spectroscopy requires three light-matter interactions, two with the pump and one with the probe. After the third interaction, the emitted signal is measured, usually by interfering the emitted signal with a local oscillator, as described in section 1.1 and illustrated by Figure 1.5a. The two pump interactions can either come from two interactions with a single pulse, which is what happens in TA spectroscopy, or two pump

pulses can be used. A single pump pulse would be used for a frequency-domain 2D spectroscopy experiment, where the transient spectrum is collected for many narrowband pump frequencies.[40] Scanning the pump in the frequency domain is not common for 2DES as using narrow band pulses reduces the minimum time-resolution possible. The more common approach, and the one used for all 2D spectra in this dissertation, is to use two broad bandwidth pump pulses and scan the time between the two, thus creating the pump frequency dimension in the time-domain.[42]

The probe axis can also be generated in the frequency or time-domain. Just as in frequency-domain linear spectroscopy, if the local oscillator is broad bandwidth and overlapped with the emitted signal onto a diffraction grating and dispersed on a camera, only one probe condition is needed for a 2D spectrum: no frequencies or times need to be scanned. This is the method used for the 2D spectra in this dissertation: creating the pump axis in the time domain and the probe axis in the frequency domain. A simple diagram of the pump-probe beam geometry used for the 2D experiments is shown in Figure 1.5b. It is also possible to create the probe axis in the time-domain by scanning the time between the probe pulse and the local oscillator. This method requires a separate local oscillator beam compared to the pump-probe geometry used here but is necessary when using a single-pixel detector or detecting the signal via action-detection.[16,43]

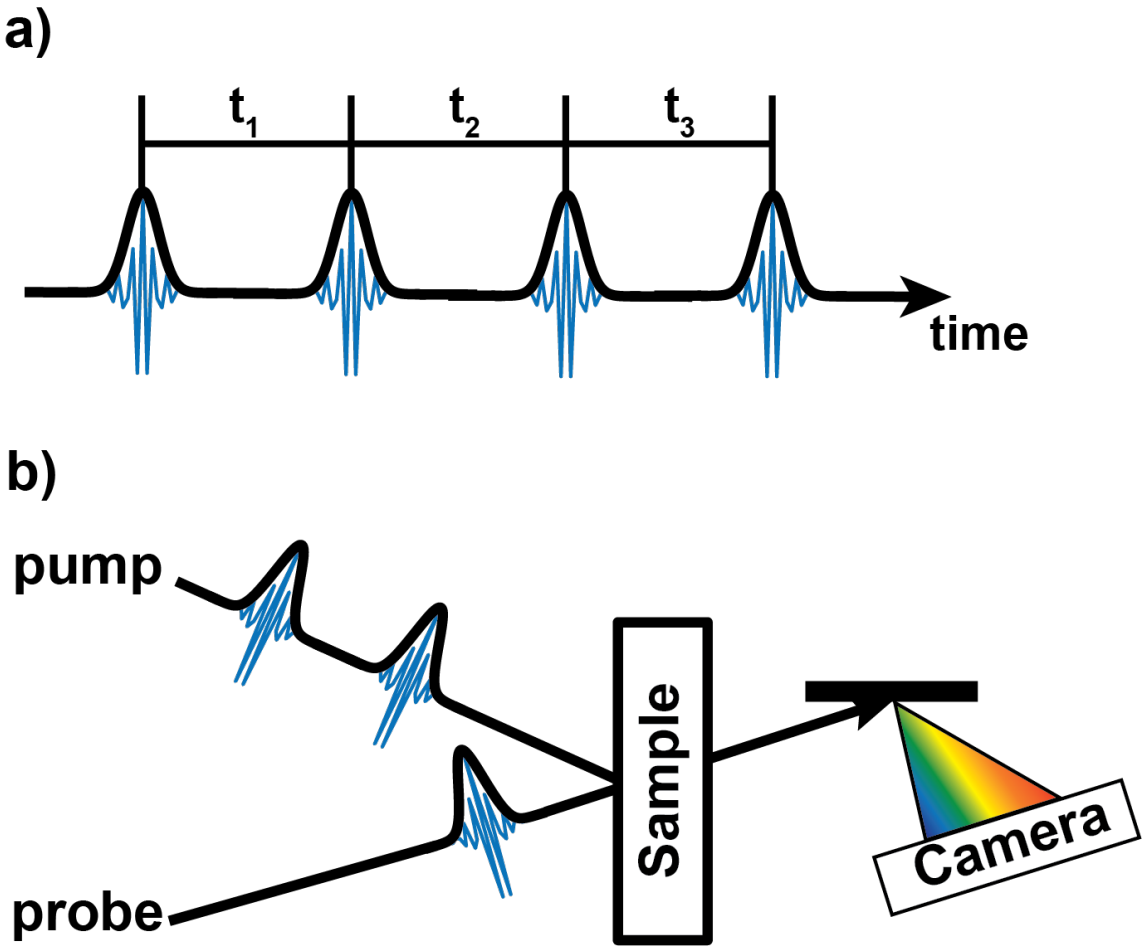

Figure 1.5. a) A fully time-domain pulse sequence for 2D spectroscopy, where the first two pulses are the pump-pulses, the third pulse is the probe, and the fourth is the emitted signal that is overlapped with the local oscillator, b) the pump-probe geometry used for the experiments in Chapter 4, where the pump axis is created in the time-domain by scanning the time between two collinear pulses, and the probe is dispersed in the frequency domain after the sample onto a camera.

Phase-matching

When using multiple laser pulses for the experiment, a parameter that can be changed is the direction at which the pulses are overlapping at the sample. The expression for the third-order emitted signal, $E_{sig}^{(3)}$, is

$$E_{sig}^{(3)}(t_1, t_2, t_3) \propto e^{i(\mp\vec{k}_1 \pm \vec{k}_2 + \vec{k}_3)\cdot\vec{r}} e^{i(\mp\phi_1 \pm \phi_2 + \phi_3)} \sum_n R_n(t_1, t_2, t_3) \quad (1.5)$$

Where $\vec{k}_n$ is the wavevector for pulse n, ϕ_n is the phase of pulse n, and R_n are all the possible response functions due to the interactions with the three pulses. Details and derivations of response functions can be found in Hamm and Zanni.[20] One relevant aspect of this expression when considering the experimental conditions necessary to measure the third-order signal is that the direction of the emitted signal is dependent on the wavevectors of the three interacting pulses. Ensuring that the local oscillator is overlapped spatially with the emitted signal at the detector is called phase-matching. One way to ensure that the emitted signal is phase-matched is to have $\vec{k}_1 = \vec{k}_2$, as is the case in the pump-probe geometry. In this scenario, the wavevectors from the two pump pulses cancel out, and the signal is emitted in the same direction as the probe pulse, which also acts as the local oscillator.[44] If $\vec{k}_1 \neq \vec{k}_2$, the signal is emitted in a direction that is spatially separated from the three interacting pulses. This is called a boxcar geometry, and although it can be experimentally difficult to align, it can be convenient as the polarizations of all four pulses can be controlled separately and the signal is isolated from transient backgrounds due to two interactions with a single pump pulse.[42]

The pump-probe geometry is most convenient to implement when there is a way to create the pump-pair so that the pulses are inherently collinear. One method that can be used to create a collinear pump-pair is with two sets of birefringent wedge pairs via a method called Translating-Wedge-Based Identical Pulses eNcoding System (TWINS).[45] TWINS is experimentally simple to implement and creates an intrinsically phase-matched pulse-pair. However, the time-delay between the two pump pulses, called the coherence time, is scanned by moving the position of two of the wedges, which cannot be done on a shot-to-shot basis.[35] Another method to create the collinear pump-pair is to use a pulse shaper,[44] which is the method I have utilized for the entirety of my research and describe in the section 1.3.

Phase-cycling and rotating frame

In addition to the emitted signal depending on the wavevectors of the interacting pulses, equation (1.5) shows that the emitted signal also depends on the phase of the three pulses. With a method called phase-cycling, the phase dependence of the emitted signal can be used to isolate specific third-order pathways or remove transient background, similarly to the way that phase-matching can be used to isolate the third-order signal spatially.[46,47] Phase-cycling measures the transient signal for various cases of the pump phase. For example, a common phase-cycling scheme is 4-frame phase cycling, meaning four different pump phase combinations are used for each coherence time. The pump phases are $\phi_1 = 0\ \phi_2 = 0, \phi_1 = \pi\ \phi_2 = 0, \phi_1 = \pi\ \phi_2 = \pi$, and $\phi_1 = 0\ \phi_2 = \pi$. The transient signals due to the two interactions with a single pump pulse are not dependent on the phase of the pump pulses ($+\phi_n - \phi_n = 0$), and the scatter from each pump pulse is dependent on the phase from that pulse (ϕ_1 or ϕ_2). Therefore, 4-frame phase-cycling can remove the pump scatter and transients when combing the shots as:

$$+ S(\phi_1 = 0\ \phi_2 = 0) - S(\phi_1 = 0\ \phi_2 = \pi) + S(\phi_1 = \pi\ \phi_2 = \pi) - S(\phi_1 = \pi\ \phi_2 = 0) \quad (1.6)$$

The phase of the pump pulses can also be manipulated to shift the observed frequency of the emitted signal with a rotating frame.[44,48] The emitted signal can be written as oscillating at the frequency of the transition plus the relative phase between the pump pulses:

$$\mathrm{S}(t_1, \omega_3) \propto \cos(\omega t_1 + \Delta\phi_{12}) \quad (1.7)$$

Where ω_3 is the probe frequency and $\Delta\phi_{12}$ is the relative phase between the two pump pulses. The relative phase can be changed as a function of t_1 so that the observed frequency is shifted to lower frequencies. Use of the rotating frame allows for means of under-sampling the time-domain signal so that fewer laser shots are needed to measure a full 2D spectrum.[44]

Pulse compression

The final practical consideration I will discuss for 2D spectroscopy is compression of the ultrafast pulses. The goal of 2D spectroscopy for the applications described above is to measure dynamics of semiconductor systems with ultrafast time-resolution. The electronic transitions and energy transfer can happen on the timescale of femtoseconds to picoseconds.[49–51] An advantage of using broad bandwidth laser pulses is the transform-limit of the pulses can be shorter than 10 fs.[52,53] However, in a 2D experiment, the pulses must pass through transmissive optics of various thickness, such as polarizers, waveplates, or acousto-optic modulators (AOM). These optics contribute dispersion to the laser pulses, such that the longer wavelength light arrives earlier at the sample than the shorter wavelength light, called positive dispersion. Without proper compensation the pulse can be as long as 1 ps at the sample position.

One approach to minimize the dispersion is to limit the number of transmissive optics in the experiment. Another common approach is to use chirped mirrors, which are mirrors with coatings that apply a negative dispersion to the pulse to compensate for the positive dispersion from the transmissive optics. Additionally, pulse shapers can be used to apply arbitrary phase to the pulse as a function of wavelength. A combination of chirped mirrors and pulse shaping is used to compress the pulse pair used for the experiments in this dissertation (Chapter 3).

1.4 Pulse shaping

Pulse shaping is a method that can implement all the experimental conditions described in the previous section: create a phase-matched pulse pair, cycle the phase of the pulses, apply a rotating frame, and correct for dispersion. There are different kinds of pulse shapers, such as spatial light modulators, which utilize liquid crystals, and AOM pulse shapers.[54] The pulse shapers used in all my research projects and in the Zanni Group are AOM pulse shapers in the 4-f geometry.

The premise of an AOM based pulse shaper is a function, $M(\omega)$, is created with an arbitrary waveform generator (AWG) and is sent to the AOM. The AOM is comprised of a crystal and a piezo-electric transducer, which converts the electrical radio frequency wave from the AWG into an acoustic wave in the crystal. The AOM works by means of the acousto-optic effect, where the acoustic wave modifies the refractive index of the material due to the mechanical strain.[55–57] If the timing is such that the laser pulse is passing through the crystal at the same time as the acoustic wave, the light will be diffracted at a different angle due to the modified refractive index. One method of AOM based pulse shaping is acousto-optic programable dispersive filters (AOPDF), which send the acoustic wave collinearly with the laser pulse.[56] Although an AOPDF does not require the use of gratings, it is limited in the bandwidth that can be shaped at one time and the repetition rate is limited to only a few kHz. In the 4-f geometry, the laser pulse is first incident on a diffraction grating to disperse the pulse into the frequency-domain, see Figure 1.6. The pulse is then collimated and passes through the AOM crystal, so that each wavelength corresponds to a different position (time) in the mask function. After the AOM, the light is focused and directed to a second diffraction grating to convert the pulse back into the time-domain. The experimental details of the 4-f geometry AOM pulse shaper are described in Chapter 2, as well as its capabilities for dispersion and spatial chirp compression being discussed in Chapter 3.

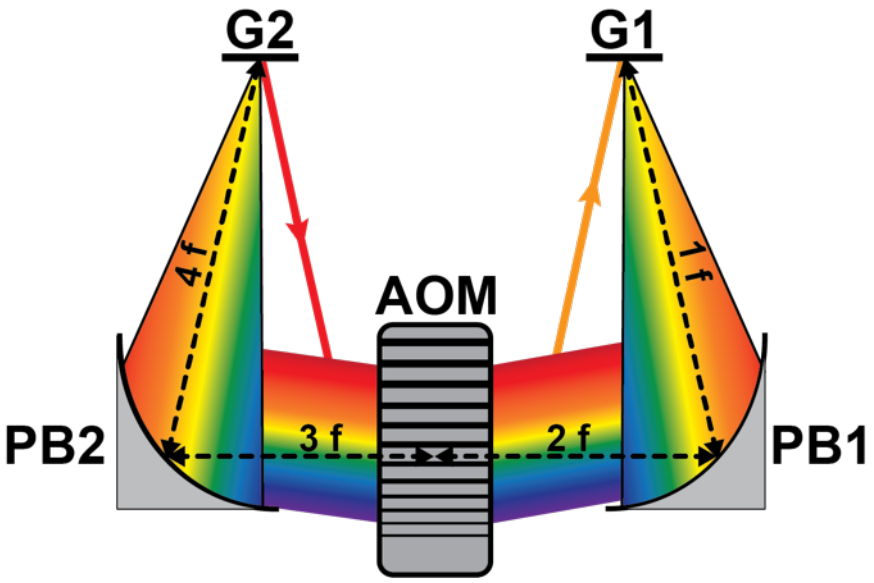

Figure 1.6 AOM based pulse shaper, G: grating, PB: 1D parabolic mirror.

1.5 Fourier transform photothermal spectroscopy

As described above, 2D spectroscopy is a method that can provide electronic structure information of semiconducting materials with ultrafast time resolution. This is one aspect of understanding energy transfer within and between photovoltaic device layers. The other aspect discussed above is spatial resolution. Fourier transform photothermal spectroscopy (FTPT) is a method I developed that can obtain electronic structure information with ~50 nm spatial resolution. This method performs linear spectroscopy in the time-domain and detects the signal with an atomic force microscope (AFM).

1.5.1 Atomic Force Microscopy

AFM is a form of scanning probe microscopy that has been a common tool for studying the morphology of material and biological samples.[58] Unlike most microscopy methods, scanning probe microscopies do not use a focused beam of light or electrons to create the image. In AFM, an extremely sharp tip at the end of a cantilever is lowered above the sample of interest, until it is

touching the sample, pushing down on the sample with a small amount of force. While the tip is in contact with the sample, the sample is scanned beneath the tip. As the sample is scanned, the z-position of the tip follows the height of the sample. By monitoring the z-position of the tip, the topography of the sample is imaged. Although the concept of AFM is straight forward, sophisticated solutions and electronics for monitoring and controlling the position of the AFM cantilever are needed. A diagram of the common AFM components is shown in Figure 1.7. The most essential component are the AFM cantilever, which interacts with the sample, a continuous wave laser that reflects off the back of the cantilever onto a four quadrant photodetector (4QPD) to monitor the z-position of the cantilever, a piezo-electric stage in the AFM head to control the z-position of the cantilever, a piezo-electric stage that the sample sits on to control the position of the sample in all three dimensions, and control and feedback electronics that communicate with the 4QPD and piezo-electric stages.

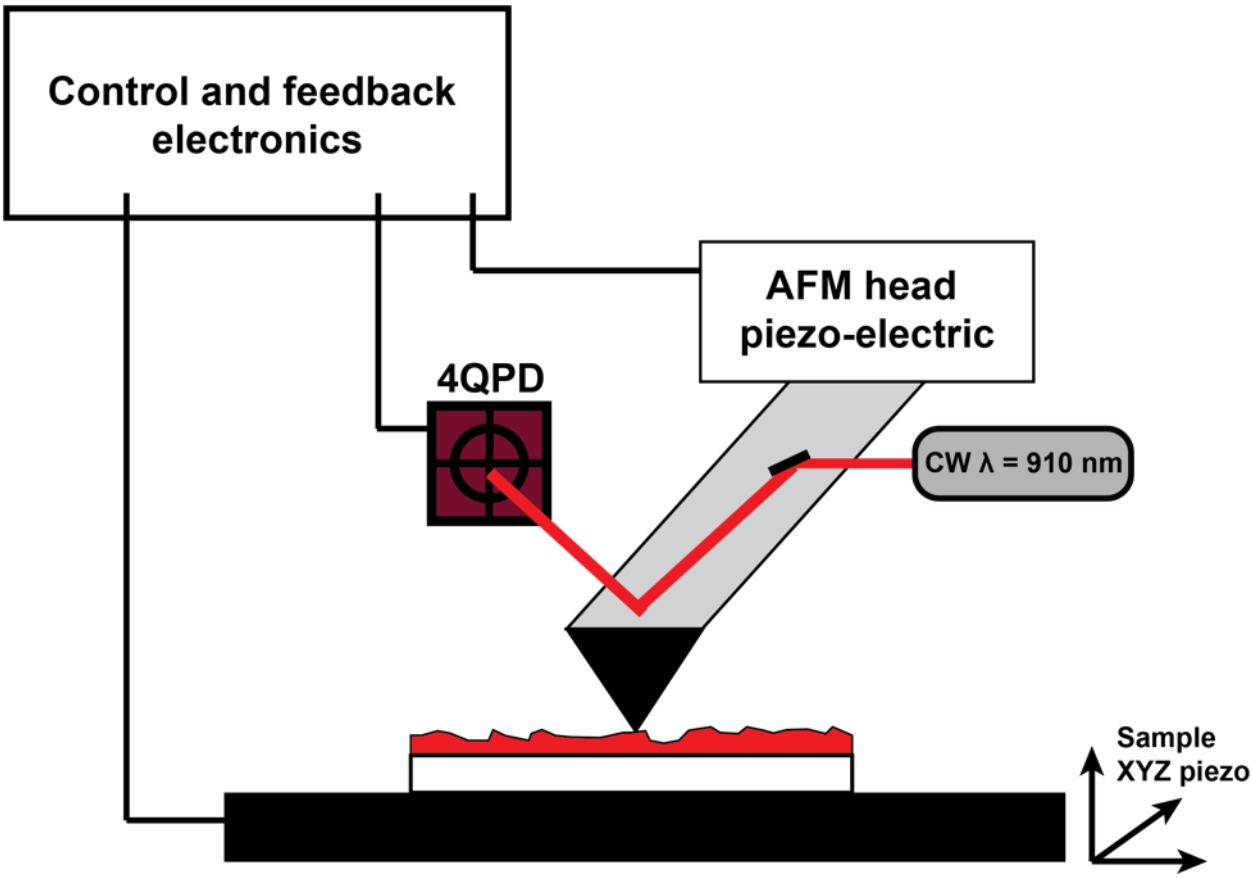

Figure 1.7. AFM diagram showing the essential components needed. The AFM tip extends from a cantilever, whose z-position is controlled by a piezo-electric stage. The z-position of the AFM tip is monitored by reflecting a continuous wave laser off the back of the cantilever onto a 4QPD. The sample is scanned beneath the AFM tip by a separate X-Y-Z piezo-electric stage. The voltage of the 4QPD is routed to the control electronics, which then communicates with the piezo-electric stages to maintain a constant force or position of the AFM tip.

There are a variety of methods for imaging with AFM, but the two used in this work are contact and tapping mode. The difference in these two methods is how the tip interacts with the sample. In tapping mode, the AFM cantilever is driven by the AFM head piezo-electric at a set amplitude so that at the lowest point in the oscillation of the cantilever the tip briefly touches the sample. The cantilever is a damped harmonic oscillator, and as such has specific frequencies at which it will oscillate, called the mechanical resonances.[59,60] The cantilever is driven at one of these frequencies. As the sample is scanned beneath the tip, the feedback electronics will adjust the height of the sample and AFM tip to maintain the AFM oscillation amplitude as close to the

defined constant value as possible. The amount that the two piezo-electric stages must be adjusted as the sample is scanned is how the topography of the sample is determined.

The method for determining the topography in contact mode is almost identical to the tapping mode method. The key difference is that instead of driving the cantilever at a resonance frequency so that the tip is only briefly in contact with the sample, in contact mode the tip is stationary, so that it is always in contact with the sample. The feedback electronics attempt to keep the deflection of the continuous wave laser constant instead of striving to keep the cantilever oscillating at a constant amplitude. It is convenient for the tip to always be in contact with the sample when attempting to measure specific properties of the sample, such as photocurrent or photothermal expansion (Chapter 5), however contact mode imaging can be destructive to fragile samples due to the lateral forces exerted by the tip when scanning the sample.[58] The experimental details of the AFM used in my research are discussed in Chapter 2.

1.5.2 Photothermal detection

In FTPT the spectroscopic signal is measured via action detection. The action that is detected is a photothermal expansion. The pulse pair from the pulse shaper is directed beneath the AFM tip. If the sample absorbs the light, the energy from the light must be conserved. One way the energy is conserved is through heat, which creates an increase in temperature and causes the sample to expand. The expansion is small, on the order of picometers, and below the noise of many AFMs.[60] However, since the pulses are very short the temperature increase and expansion is very fast, resulting in a large upward force on the AFM tip. The deflection of the AFM cantilever causes the continuous wave laser reflecting off the cantilever to deflect from its stationary position on the 4QPD. The photothermal signal can be expressed as:

$$S(\lambda) = \frac{\alpha_{th}{\nu_s}^2}{C_p}\eta_{th}\alpha_{abs}(\lambda)I \tag{1.8}$$

Where α_{th} is the thermal expansion coefficient, v_s is the speed of sound in the material, C_p is the heat capacity at constant pressure, η_{th} is the heat conversion efficiency, α_{abs} is the absorption coefficient, and I is the intensity of the light.[61] The key information from this expression is that the signal is linearly proportional to the absorption. Early theoretical research explicitly derived the linear proportionality of the photothermal signal to the amount of light absorbed,[60] and experimental work has confirmed this statement, including my work in Chapter 5.

1.6 Summary of projects

In Chapter 2 I will discuss the experimental details of the spectroscopy and microscopy methods I used in my research. I will start by describing the optical setup of the white-light generation and of the quartz AOM pulse shaper. I will also provide alignment tips for maximizing the through-put of the pulse shaper. I will then describe the remaining optical setup necessary for ultrafast TA and 2D WL spectroscopy, as well as the standard parameters used for the corresponding measurements. In addition, I will describe the experimental process for characterizing ultrafast laser pulses for the optical setup I worked with. Finally, in Chapter 2 I will describe the experimental layout for FTPT and provide details on the practical aspects of the experiment.

In Chapter 3 I will present the implementation of a quartz AOM pulse shaper for spatial and temporal control of a broadband femtosecond laser pulse. The experiments demonstrating the application of spectral phase to the laser pulse to temporally chirp the pulse, so that given wavelengths of light arrive earlier than others within the pulse envelope, are shown. I was able to demonstrate that by using chirped mirrors to negatively chirp the pulse so that the bluer light would arrive at the AOM ahead of the redder light, the phase necessary to temporally compress the pulse

was such that all the light was also diffracted at the Bragg angle. When all the light is diffracted at the Bragg angle, all the wavelengths are evenly distributed spatially in the beam.

In Chapter 4 I illustrate how pulse shaping can be used for ultrafast spectroscopy through characterization of lead-halide perovskites. Lead-halide perovskite photovoltaic devices continue to increase in efficiency. One route to improved performance is the inclusion of cations and halides of mixed composition. In Chapter 4 I show the 2D WL spectra of mixed lead-halide perovskite films using combinations of the organic-cations methylammonium, formamidinium, and Br^-/Cs^+. Linear absorption spectra of all the samples are smooth and vary only in the position of their bandgaps, but they have different 2D WL spectra. There are features in the samples containing only organic large cations (methylammonium and formamidinium), that are not present in the sample containing Br^- and Cs^+, which suggests the Br^- and Cs^+ are altering the electronic structure of the films to impact efficiency, helping to explain why the bandgap alone is insufficient to explain perovskite solar cell efficiencies.

In Chapter 5 I demonstrate another use of a pulse shaper for microscopy with sub-diffraction limit spatial resolution. I present a time-domain version of photothermal microscopy using an AFM, which I call Fourier transform photothermal (FTPT) spectroscopy. The pulse shaper sets the delay and phases of the pulses shot-to-shot at 100 kHz, enabling background subtraction and data collection in the rotating frame. The pulse shaper is also used to flatten the pulse spectrum, thereby eliminating the need for normalization by the laser spectrum. I demonstrate the method on TIPS-pentacene microcrystals and Mn-phthalocyanine islands, confirming sub-diffraction spatial resolution, and providing new spectroscopic insights likely linked to structural defects in the crystals. FTPT is a method that can resolve electronic structure information from individual grains in a semiconducting thin film.

1.7 References

(1) Nelson, J. *The Physics of Solar Cells*; Imperial College Press, 2003.
(2) Green, M. A.; Ho-Baillie, A.; Snaith, H. J. The Emergence of Perovskite Solar Cells. *Nature Photonics* **2014**, *8* (7), 506–514. https://doi.org/10.1038/nphoton.2014.134.
(3) Leo, K. Organic Photovoltaics. *Nat Rev Mater* **2016**, *1* (8), 1–2. https://doi.org/10.1038/natrevmats.2016.56.
(4) Congreve, D. N.; Lee, J.; Thompson, N. J.; Hontz, E.; Yost, S. R.; Reusswig, P. D.; Bahlke, M. E.; Reineke, S.; Van Voorhis, T.; Baldo, M. A. External Quantum Efficiency Above 100% in a Singlet-Exciton-Fission–Based Organic Photovoltaic Cell. *Science* **2013**, *340* (6130), 334–337. https://doi.org/10.1126/science.1232994.
(5) Yang, L.; Tabachnyk, M.; Bayliss, S. L.; Böhm, M. L.; Broch, K.; Greenham, N. C.; Friend, R. H.; Ehrler, B. Solution-Processable Singlet Fission Photovoltaic Devices. *Nano Lett.* **2015**, *15* (1), 354–358. https://doi.org/10.1021/nl503650a.
(6) Jacobsson, T. J.; Correa-Baena, J.-P.; Pazoki, M.; Saliba, M.; Schenk, K.; Grätzel, M.; Hagfeldt, A. Exploration of the Compositional Space for Mixed Lead Halogen Perovskites for High Efficiency Solar Cells. *Energy & Environmental Science* **2016**, *9* (5), 1706–1724. https://doi.org/10.1039/C6EE00030D.
(7) Zhao, J.; Li, Y.; Yang, G.; Jiang, K.; Lin, H.; Ade, H.; Ma, W.; Yan, H. Efficient Organic Solar Cells Processed from Hydrocarbon Solvents. *Nat Energy* **2016**, *1* (2), 1–7. https://doi.org/10.1038/nenergy.2015.27.
(8) Nah, S.; Spokoyny, B.; Stoumpos, C.; Soe, C. M. M.; Kanatzidis, M.; Harel, E. Spatially Segregated Free-Carrier and Exciton Populations in Individual Lead Halide Perovskite Grains. *Nature Photon* **2017**, *11* (5), 285–288. https://doi.org/10.1038/nphoton.2017.36.
(9) Karki, A.; Vollbrecht, J.; J. Gillett, A.; Shuyong Xiao, S.; Yang, Y.; Peng, Z.; Schopp, N.; L. Dixon, A.; Yoon, S.; Schrock, M.; Ade, H.; Manjunatha Reddy, G. N.; H. Friend, R.; Nguyen, T.-Q. The Role of Bulk and Interfacial Morphology in Charge Generation, Recombination, and Extraction in Non-Fullerene Acceptor Organic Solar Cells. *Energy & Environmental Science* **2020**, *13* (10), 3679–3692. https://doi.org/10.1039/D0EE01896A.
(10) Kim, B.; Khan, R. M.; Fast, A.; Fishman, D. A.; Potma, E. O. Nanoscale Excitation Dynamics of Carbon Nanotubes Probed with Photoinduced Force Microscopy. *J. Phys. Chem. C* **2020**, *124* (21), 11694–11700. https://doi.org/10.1021/acs.jpcc.0c01776.
(11) Katzenmeyer, A. M.; Canivet, J.; Holland, G.; Farrusseng, D.; Centrone, A. Assessing Chemical Heterogeneity at the Nanoscale in Mixed-Ligand Metal–Organic Frameworks with the PTIR Technique. *Angewandte Chemie International Edition* **2014**, *53* (11), 2852–2856. https://doi.org/10.1002/anie.201309295.
(12) Wong, C. Y.; Penwell, S. B.; Cotts, B. L.; Noriega, R.; Wu, H.; Ginsberg, N. S. Revealing Exciton Dynamics in a Small-Molecule Organic Semiconducting Film with Subdomain Transient Absorption Microscopy. *J. Phys. Chem. C* **2013**, *117* (42), 22111–22122. https://doi.org/10.1021/jp407645k.
(13) Guo, Z.; Zhou, N.; Williams, O. F.; Hu, J.; You, W.; Moran, A. M. Imaging Carrier Diffusion in Perovskites with a Diffractive Optic-Based Transient Absorption Microscope. *J. Phys. Chem. C* **2018**, *122* (19), 10650–10656. https://doi.org/10.1021/acs.jpcc.8b03643.
(14) Guo, Z.; Wan, Y.; Yang, M.; Snaider, J.; Zhu, K.; Huang, L. Long-Range Hot-Carrier Transport in Hybrid Perovskites Visualized by Ultrafast Microscopy. *Science* **2017**, *356* (6333), 59–62. https://doi.org/10.1126/science.aam7744.

(15) Jones, A. C.; Kearns, N. M.; Ho, J.-J.; Flach, J. T.; Zanni, M. T. Impact of Non-Equilibrium Molecular Packings on Singlet Fission in Microcrystals Observed Using 2D White-Light Microscopy. *Nature Chemistry* **2019**, 1–8. https://doi.org/10.1038/s41557-019-0368-9.
(16) Purz, T. L.; Martin, E. W.; Rivera, P.; Holtzmann, W. G.; Xu, X.; Cundiff, S. T. Coherent Exciton-Exciton Interactions and Exciton Dynamics in a ${\mathrm{MoSe}}_{2}/{\mathrm{WSe}}_{2}$ Heterostructure. *Phys. Rev. B* **2021**, *104* (24), L241302. https://doi.org/10.1103/PhysRevB.104.L241302.
(17) J. Michael Hollas. *Modern Spectroscopy*; Wiley: Chichester, 2004; Vol. 4th ed.
(18) Shockley, W.; Queisser, H. J. Detailed Balance Limit of Efficiency of P-n Junction Solar Cells. 11.
(19) Spano, F. C. The Spectral Signatures of Frenkel Polarons in H- and J-Aggregates. *Acc. Chem. Res.* **2010**, *43* (3), 429–439. https://doi.org/10.1021/ar900233v.
(20) Hamm, P.; Zanni, M. T. *Concepts and Methods of 2d Infrared Spectroscopy*; Cambridge University Pres: Cambridge ; New York, 2011.
(21) Armstrong, Z. T.; Kunz, M. B.; Jones, A. C.; Zanni, M. T. Thermal Annealing of Singlet Fission Microcrystals Reveals the Benefits of Charge Transfer Couplings and Slip-Stacked Packing. *J. Phys. Chem. C* **2020**, *124* (28), 15123–15131. https://doi.org/10.1021/acs.jpcc.0c05277.
(22) Katzenmeyer, A. M.; Holland, G.; Kjoller, K.; Centrone, A. Absorption Spectroscopy and Imaging from the Visible through Mid-Infrared with 20 Nm Resolution. *Anal. Chem.* **2015**, *87* (6), 3154–3159. https://doi.org/10.1021/ac504672t.
(23) Bell, R. J. CHAPTER ONE - Fourier Transform Spectroscopy. In *Introductory Fourier Transform Spectroscopy*; Bell, R. J., Ed.; Academic Press, 1972; pp 1–15. https://doi.org/10.1016/B978-0-12-085150-8.50006-1.
(24) edited by John R. Ferraro, L. J. B. *Fourier Transform Infrared Spectroscopy : Applications to Chemical Systems. Volume 4*; Academic Press: Orlando, 1985.
(25) Mehlenbacher, R. D.; McDonough, T. J.; Grechko, M.; Wu, M.-Y.; Arnold, M. S.; Zanni, M. T. Energy Transfer Pathways in Semiconducting Carbon Nanotubes Revealed Using Two-Dimensional White-Light Spectroscopy. *Nature Communications* **2015**, *6* (1). https://doi.org/10.1038/ncomms7732.
(26) Takeda, Y.; Sasaki, A.; Imamura, Y.; Takagi, T. Electron Mobility and Energy Gap of In0.53Ga0.47As on InP Substrate. *Journal of Applied Physics* **1976**, *47* (12), 5405–5408. https://doi.org/10.1063/1.322570.
(27) Vanecek, M.; Poruba, A. Fourier-Transform Photocurrent Spectroscopy of Microcrystalline Silicon for Solar Cells. *Appl. Phys. Lett.* **2002**, *80* (5), 719–721. https://doi.org/10.1063/1.1446207.
(28) Nardin, G.; Autry, T. M.; Silverman, K. L.; Cundiff, S. T. Multidimensional Coherent Photocurrent Spectroscopy of a Semiconductor Nanostructure. *Opt. Express, OE* **2013**, *21* (23), 28617–28627. https://doi.org/10.1364/OE.21.028617.
(29) Tekavec, P. F.; Lott, G. A.; Marcus, A. H. Fluorescence-Detected Two-Dimensional Electronic Coherence Spectroscopy by Acousto-Optic Phase Modulation. *The Journal of Chemical Physics* **2007**, *127* (21), 214307. https://doi.org/10.1063/1.2800560.
(30) Dazzi, A.; Prazeres, R.; Glotin, F.; Ortega, J. M. Local Infrared Microspectroscopy with Subwavelength Spatial Resolution with an Atomic Force Microscope Tip Used as a Photothermal Sensor. *Opt. Lett., OL* **2005**, *30* (18), 2388–2390. https://doi.org/10.1364/OL.30.002388.

(31) Petti, M. K.; Lomont, J. P.; Maj, M.; Zanni, M. T. Two-Dimensional Spectroscopy Is Being Used to Address Core Scientific Questions in Biology and Materials Science. *J. Phys. Chem. B* **2018**, *122* (6), 1771–1780. https://doi.org/10.1021/acs.jpcb.7b11370.
(32) Biswas, S.; Kim, J.; Zhang, X.; Scholes, G. D. Coherent Two-Dimensional and Broadband Electronic Spectroscopies. *Chem. Rev.* **2022**, *122* (3), 4257–4321. https://doi.org/10.1021/acs.chemrev.1c00623.
(33) Richter, J. M.; Branchi, F.; Camargo, F. V. de A.; Zhao, B.; Friend, R. H.; Cerullo, G.; Deschler, F. Ultrafast Carrier Thermalization in Lead Iodide Perovskite Probed with Two-Dimensional Electronic Spectroscopy. *Nature Communications* **2017**, *8* (1), 376. https://doi.org/10.1038/s41467-017-00546-z.
(34) Armstrong, Z. T.; Kunz, M. B.; Zanni, M. T. Ultrafast Fluctuations in PM6 Domains of Binary and Ternary Organic Photovoltaic Thin Films Probed with Two-Dimensional White-Light Spectroscopy. *J. Phys. Chem. Lett.* **2021**, *12* (37), 8972–8979. https://doi.org/10.1021/acs.jpclett.1c02234.
(35) Kearns, N. M.; Mehlenbacher, R. D.; Jones, A. C.; Zanni, M. T. Broadband 2D Electronic Spectrometer Using White Light and Pulse Shaping: Noise and Signal Evaluation at 1 and 100 KHz. *Opt. Express, OE* **2017**, *25* (7), 7869–7883. https://doi.org/10.1364/OE.25.007869.
(36) Le, A. K.; Bender, J. A.; Arias, D. H.; Cotton, D. E.; Johnson, J. C.; Roberts, S. T. Singlet Fission Involves an Interplay between Energetic Driving Force and Electronic Coupling in Perylenediimide Films. *J. Am. Chem. Soc.* **2018**, *140* (2), 814–826. https://doi.org/10.1021/jacs.7b11888.
(37) Aruda, K. O.; Bohlmann Kunz, M.; Tagliazucchi, M.; Weiss, E. A. Temperature-Dependent Permeability of the Ligand Shell of PbS Quantum Dots Probed by Electron Transfer to Benzoquinone. *J. Phys. Chem. Lett.* **2015**, *6* (14), 2841–2846. https://doi.org/10.1021/acs.jpclett.5b01256.
(38) Higgins, K.; Calhoun, T. R. Compressed Supercontinuum Probe for Transient Absorption Microscopy. *Opt. Lett., OL* **2018**, *43* (8), 1750–1753. https://doi.org/10.1364/OL.43.001750.
(39) McDonough, T. J.; Zhang, L.; Roy, S. S.; Kearns, N. M.; Arnold, M. S.; Zanni, M. T.; Andrew, T. L. Triplet Exciton Dissociation and Electron Extraction in Graphene-Templated Pentacene Observed with Ultrafast Spectroscopy. *Phys. Chem. Chem. Phys.* **2017**, *19* (6), 4809–4820. https://doi.org/10.1039/C6CP06454J.
(40) Hamm, P.; Lim, M.; Hochstrasser, R. M. Structure of the Amide I Band of Peptides Measured by Femtosecond Nonlinear-Infrared Spectroscopy. *J. Phys. Chem. B* **1998**, *102* (31), 6123–6138. https://doi.org/10.1021/jp9813286.
(41) Hybl, J. D.; Albrecht Ferro, A.; Jonas, D. M. Two-Dimensional Fourier Transform Electronic Spectroscopy. *J. Chem. Phys.* **2001**, *115* (14), 6606–6622. https://doi.org/10.1063/1.1398579.
(42) Fuller, F. D.; Ogilvie, J. P. Experimental Implementations of Two-Dimensional Fourier Transform Electronic Spectroscopy. *Annual Review of Physical Chemistry* **2015**, *66* (1), 667–690. https://doi.org/10.1146/annurev-physchem-040513-103623.
(43) Karki, K. J.; Widom, J. R.; Seibt, J.; Moody, I.; Lonergan, M. C.; Pullerits, T.; Marcus, A. H. Coherent Two-Dimensional Photocurrent Spectroscopy in a PbS Quantum Dot Photocell. *Nat Commun* **2014**, *5* (1), 1–7. https://doi.org/10.1038/ncomms6869.
(44) Shim, S.-H.; Zanni, M. T. How to Turn Your Pump–Probe Instrument into a Multidimensional Spectrometer: 2D IR and Vis Spectroscopiesvia Pulse Shaping. *Phys. Chem. Chem. Phys.* **2009**, *11* (5), 748–761. https://doi.org/10.1039/B813817F.

(45) Brida, D.; Manzoni, C.; Cerullo, G. Phase-Locked Pulses for Two-Dimensional Spectroscopy by a Birefringent Delay Line. *Opt. Lett., OL* **2012**, *37* (15), 3027–3029. https://doi.org/10.1364/OL.37.003027.
(46) Mueller, S.; Lüttig, J.; Malý, P.; Ji, L.; Han, J.; Moos, M.; Marder, T. B.; Bunz, U. H. F.; Dreuw, A.; Lambert, C.; Brixner, T. Rapid Multiple-Quantum Three-Dimensional Fluorescence Spectroscopy Disentangles Quantum Pathways. *Nat Commun* **2019**, *10* (1), 4735. https://doi.org/10.1038/s41467-019-12602-x.
(47) Tan, H.-S. Theory and Phase-Cycling Scheme Selection Principles of Collinear Phase Coherent Multi-Dimensional Optical Spectroscopy. *J. Chem. Phys.* **2008**, *129* (12), 124501. https://doi.org/10.1063/1.2978381.
(48) Strasfeld, D. B.; Ling, Y. L.; Shim, S.-H.; Zanni, M. T. Tracking Fiber Formation in Human Islet Amyloid Polypeptide with Automated 2D-IR Spectroscopy. *J. Am. Chem. Soc.* **2008**, *130* (21), 6698–6699. https://doi.org/10.1021/ja801483n.
(49) Mehlenbacher, R. D.; Wu, M.-Y.; Grechko, M.; Laaser, J. E.; Arnold, M. S.; Zanni, M. T. Photoexcitation Dynamics of Coupled Semiconducting Carbon Nanotube Thin Films. *Nano Letters* **2013**, *13* (4), 1495–1501. https://doi.org/10.1021/nl304591w.
(50) Mehlenbacher, R. D.; Wang, J.; Kearns, N. M.; Shea, M. J.; Flach, J. T.; McDonough, T. J.; Wu, M.-Y.; Arnold, M. S.; Zanni, M. T. Ultrafast Exciton Hopping Observed in Bare Semiconducting Carbon Nanotube Thin Films with Two-Dimensional White-Light Spectroscopy. *The Journal of Physical Chemistry Letters* **2016**, *7* (11), 2024–2031. https://doi.org/10.1021/acs.jpclett.6b00650.
(51) Young, R. M.; Wasielewski, M. R. Mixed Electronic States in Molecular Dimers: Connecting Singlet Fission, Excimer Formation, and Symmetry-Breaking Charge Transfer. *Acc. Chem. Res.* **2020**, *53* (9), 1957–1968. https://doi.org/10.1021/acs.accounts.0c00397.
(52) Riedle, E.; Beutter, M.; Lochbrunner, S.; Piel, J.; Schenkl, S.; Spörlein, S.; Zinth, W. Generation of 10 to 50 Fs Pulses Tunable through All of the Visible and the NIR. *Appl Phys B* **2000**, *71* (3), 457–465. https://doi.org/10.1007/s003400000351.
(53) Bradler, M.; Baum, P.; Riedle, E. Femtosecond Continuum Generation in Bulk Laser Host Materials with Sub-MJ Pump Pulses. *Appl. Phys. B* **2009**, *97* (3), 561. https://doi.org/10.1007/s00340-009-3699-1.
(54) Weiner, A. M. Ultrafast Optical Pulse Shaping: A Tutorial Review. *Optics Communications* **2011**, *284* (15), 3669–3692. https://doi.org/10.1016/j.optcom.2011.03.084.
(55) Davis, C. C. *Lasers and Electro-Optics: Fundamentals and Engineering*; Cambridge University Press, 1996.
(56) Verluise, F.; Laude, V.; Cheng, Z.; Spielmann, C.; Tournois, P. Amplitude and Phase Control of Ultrashort Pulses by Use of an Acousto-Optic Programmable Dispersive Filter: Pulse Compression and Shaping. *Opt. Lett., OL* **2000**, *25* (8), 575–577. https://doi.org/10.1364/OL.25.000575.
(57) Dugan, M. A.; Tull, J. X.; Warren, W. S. High-Resolution Acousto-Optic Shaping of Unamplified and Amplified Femtosecond Laser Pulses. *J. Opt. Soc. Am. B, JOSAB* **1997**, *14* (9), 2348–2358. https://doi.org/10.1364/JOSAB.14.002348.
(58) Eaton, P.; West, P. *Atomic Force Microscopy*; Oxford University Press, 2010.
(59) Sarid, D. *Scanning Force Microscopy: With Applications to Electric, Magnetic, and Atomic Forces*; Oxford University Press, 1991.

(60) Dazzi, A.; Glotin, F.; Carminati, R. Theory of Infrared Nanospectroscopy by Photothermal Induced Resonance. *Journal of Applied Physics* **2010**, *107* (12), 124519. https://doi.org/10.1063/1.3429214.
(61) Park, B.; Lee, S.; Kwon, J.; Kim, W.; Jung, S.; Kim, C. Dual-Pulse Photoactivated Atomic Force Microscopy. *Sci Rep* **2021**, *11* (1), 17097. https://doi.org/10.1038/s41598-021-96646-4.

2. Methods

2.1 Creating a white-light pulse pair

2.1.1 White-light generation

Our light source is a 4 W Yb amplifier (Spirit, Spectra Physics), operating at a repetition rate of 100 kHz, a center wavelength of 1040 nm, and a pulse width of ~400 fs. 1 W (10 μJ) of the fundamental is split off with a beam-splitter for the 2D WL experiments. 500 mW (5 μJ) of the 1 W is split off to create the white-light probe, described in the next section, and 500 mW is used to create the white-light pump. The pump beam is used for both the 2D WL experiments and the FTPT experiments. To generate the white-light, the approximately 5 μJ of fundamental is focused into an 8 mm YAG crystal with a 7.5 cm focal length lens. A half waveplate and polarizer are used as a variable attenuator before focusing into the YAG to control the power so as not to have multiple filamentation, followed by an iris to control for the beam mode. I have found that the best beam mode is obtained when the iris is around 80% closed. Approximately 2.4 mW of white-light below 800 nm is generated. The white-light is recollimated after the YAG with a 90º off-axis parabolic mirror. The pulse is negatively chirped with 32 bounces (-40 fs^2/per bounce pair) on a pair of chirped mirrors (Layertec Gmbh). After the chirped mirrors, the polarization of the light is rotated 90º with a periscope. The light is then directed into the AOM pulse shaper.

2.1.2 AOM pulse shaper

The 4-f geometry pulse shaper has five main optical components: two diffraction gratings, two 1D-parabolic mirrors, and a quartz AOM. The diffraction gratings are blazed for 750 nm and have 600 groves/mm. In addition to the optical components, an arbitrary waveform generator creates the mask function, which is then amplified with an RF amplifier, which then sends the RF

pulse to the AOM. The first optic in the pulse shaper is a diffraction grating, which disperses the light in the frequency domain. One focal length away (15 cm) is the first parabolic mirror which collimates the light. This corresponds to the first "f" in the 4-f geometry. The AOM is placed one focal length from the first parabolic mirror, which corresponds to the second "f". The second parabolic mirror follows the AOM another focal length away as the third "f". The second parabolic serves to refocus and combine the light on the second diffraction grating, which is a focal length away from the second parabolic, completing the 4-f geometry. A perfect 4-f geometry should yield well collimated light, assuming all frequencies are deflected at the Bragg angle which is discussed more below. However, the 4-f geometry can be distorted to compensate for temporal chirp. Distorting the geometry changes the relative path length of the different frequencies of light, shifting the relative position in time of the different frequencies. The 4-f geometry of the pulse shaper used for these experiments was distorted by extending the last focal distance, the distance between the second parabolic mirror and the second grating, by XXmm. I have found this the best distance to distort as it has no effect on the alignment of the rest of the shaper. Only small distortions of the geometry should be used, as any distortion disrupts the collimation and leads to a spatially chirped pulse.

The AOM used in this pulse shaper is a quartz AOM. The quartz crystal is 20 mm thick, and the acoustic aperture is 10 μs. The AOM is placed and the parabolic mirrors are aligned so that the light enters the aperture at an angle slightly deviated from 90º. The angle that the light should be impinging on the crystal to achieve maximum deflection efficiency is called the Bragg angle. However, the Bragg angle is a function of the wavelength.[1] The AOM is placed to maximize the deflection efficiency for the center frequency (wavelength) of the pulse, and the acoustic wave is used to correct for the Bragg angle across the bandwidth of the pulse (Chapter 3). Another

consideration is where on the acoustic aperture the light is hitting. The efficiency of the AOM deflection decreases the farther away the light gets from the transducer.[2] For this reason, the AOM is oriented so that the lower frequency light (of which there is less) is closest to the transducer. In addition, only half the acoustic aperture is used. Although the AOM is capable at running at a 100% duty cycle, the 50% duty cycle is used to reduce the average RF power being applied to the crystal out of an abundance of caution. Excessive strain on the crystal can cause it to crack, rendering the AOM unusable. It requires a great deal of time to repair, and it is not always possible to repair cracks in the crystal. Before my work with the pulse shaper, excessive RF power resulted in a broken AOM, however since operating at a 50% duty cycle, there have been no issues with the AOM crystal in five years. The small deviation away from 90º that the light hits the AOM, and the orientation of the light so that the red is closest to the transducer is illustrated in Figure 2.1.

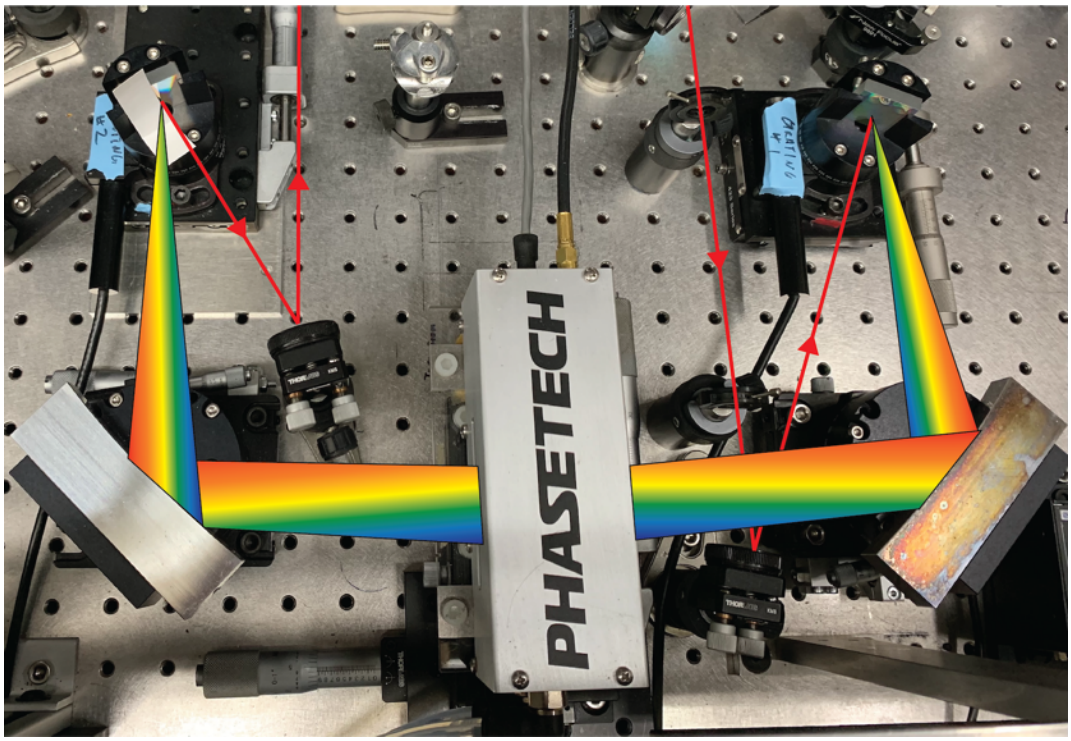

Figure 2.1. A photo of the quartz AOM pulse shaper illustrates the orientation of the light going into the AOM at a very small angle away from 90º, and with the reddest light closest to the transducer. The picture also show that the gratings are mounted on stages to make slight adjustments to the distances between the parabolic mirrors and the gratings to optimize the 4-f geometry.

A last experimental condition to consider for the pulse shaper is the polarization of the light entering the shaper. The diffraction gratings and AOM crystal have different efficiencies depending on the polarization of the incoming light. The gratings are most efficient when the incoming light is perpendicular to the grooves of the grating (Figure 2.2). The quartz crystal is birefringent, with the most efficient deflection occurring along the extraordinary axis. The way the crystal is oriented in the AOM is such that the polarization of light needed for the most efficient deflection in the AOM is perpendicular to the polarization of light needed for the most efficient diffraction on the gratings. A potential solution that I attempted to have the polarization be ideal for both the AOM and the two gratings was to insert two achromatic half waveplates into the pulse shaper. One waveplate would come immediately after the first grating to rotate the polarization 90º after reflecting off the grating; the second waveplate would come immediately before the second grating to rotate the polarization back 90º before focusing onto the grating. These conditions led to the highest efficiency shaper (~15%), but I noticed that the lowest frequency (longest wavelength) light was being cutoff. Although the waveplates are achromatic, their efficiency drops dramatically at the edges of their operating window, which is also where the intensity of the white-light pulse is lowest (750-800 nm). To conserve the red light in the pulse, the polarization going into the shaper is set to maximize deflection efficiency in the AOM, and no waveplates are used. Under these conditions 10-12% efficiency can be achieved, with a maximum of 60 μW of output white-light. Further setup specific alignment tips are included in the Appendix.

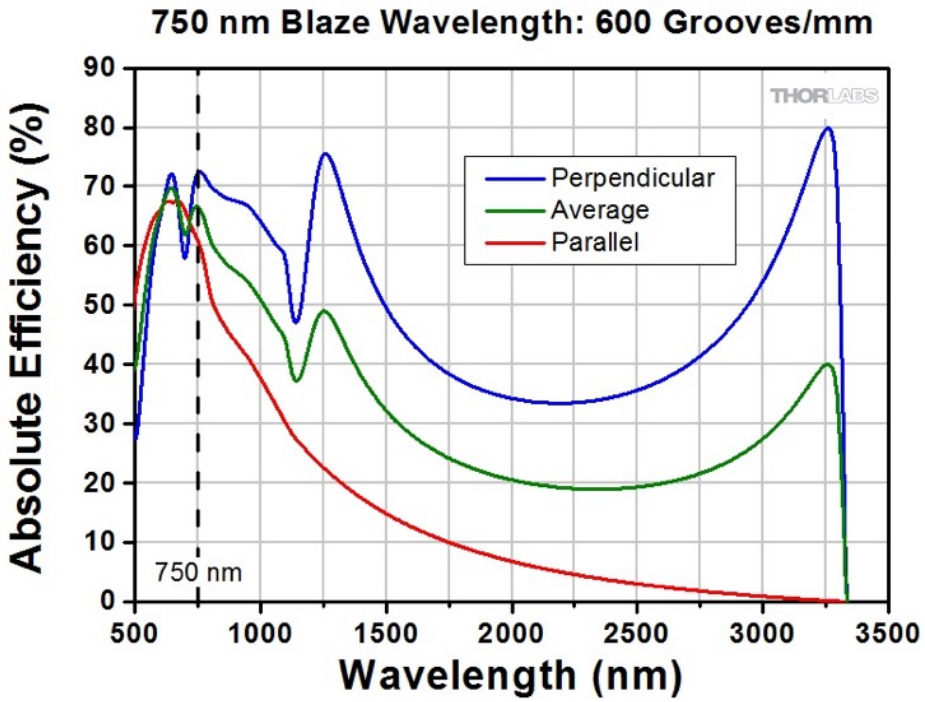

Figure 2.2. The efficiency curve from Thorlabs for the gratings used in the 4-f pulse shaper. Perpendicular and parallel refers to the polarization of the light relative to the grooves on the grating. The parallel polarization is less efficient in the window of the white-light used here (500-800 nm).

2.2 Ultrafast transient absorption and 2D WL spectrometer

One use of the shaped pulse created in the setup described above is for transient absorption and 2D WL spectroscopy. The 2D WL setup is shown in Figure 2.3. The shaped pulse is used as the pump for these experiments. The white-light probe pulse is created with the remaining 500 mW of fundamental 1040 nm light not used for the creation of the pump pulse. The fundamental beam is passed through a TeO_2 AOM chopper (Isomet) operating at a 50% duty cycle. A square pulse from a digital delay generator is sent to the AOM so that every other laser pulse is deflected. The probe is cycled on-off for 8-frame phase cycling, which is described below. The light that does not get deflected passes through a similar variable attenuator as the pump pulse, comprised of a half waveplate and a polarizer to control for the power in the white-light generation. After the variable attenuator another half waveplate is used to rotate the polarization of the probe pulse

relative to the pump light. The polarization is set before the white-light generation due to the lack of half waveplates that can accommodate such a large spectral bandwidth (520-1000 nm). The white-light maintains the same polarization as the fundamental set by the waveplate. The light is focused into a YAG crystal and collimated in the same way as the pump light, except only 4 mm of YAG is used.

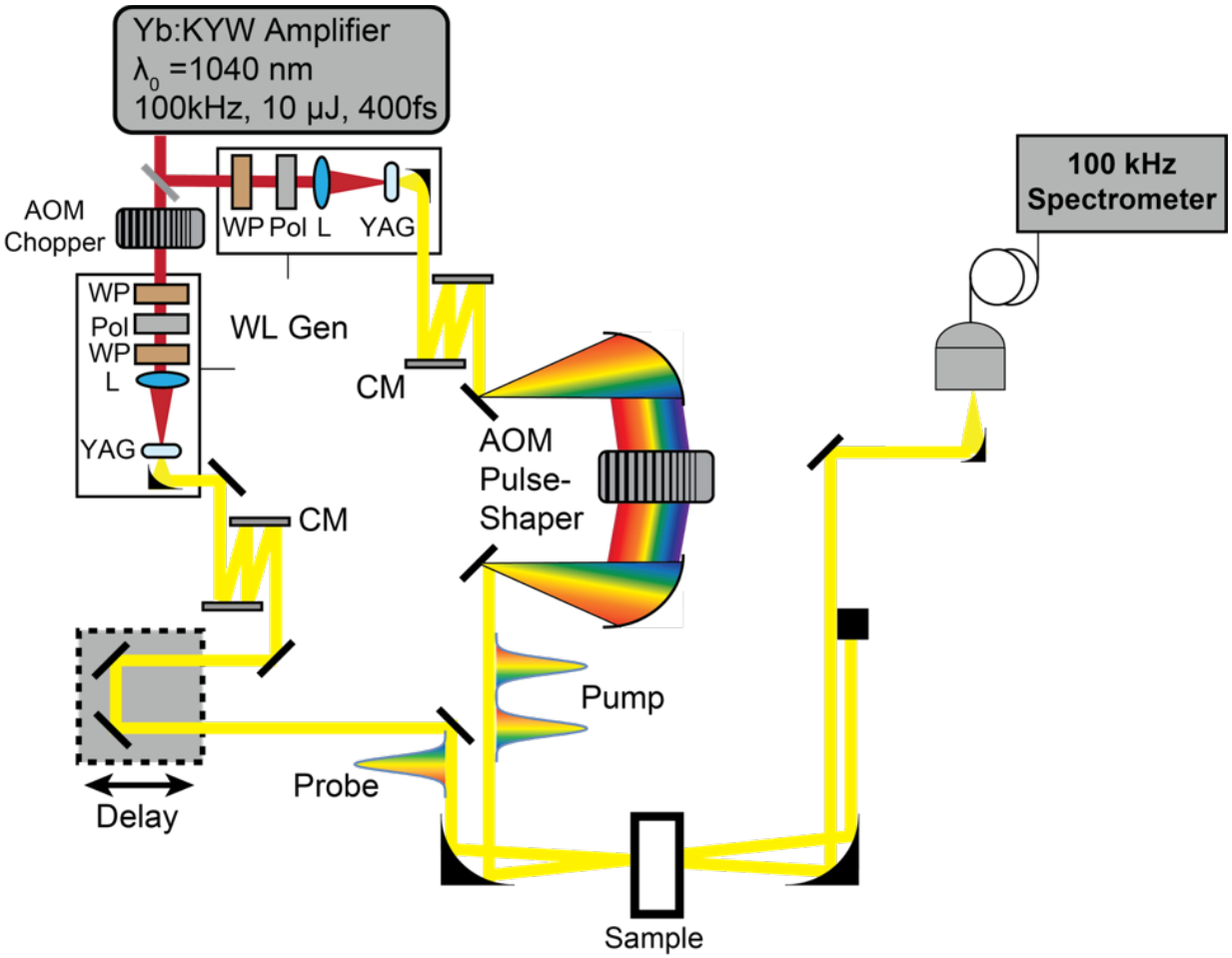

Figure 2.3. The 2D WL setup. WP: waveplate, Pol: polarizer, L: lens, CM: chirped mirror pair

The white-light passes through a 1000 nm short pass filter to filter out the remaining fundamental. A filter is not necessary for the pump pulse as the gratings in the pulse shaper effectively filter out the fundamental. After the filter, the probe white-light is compressed with 22 bounces on a chirped mirror pair (Layertec Gmbh) that are designed to compensate for 1.5 mm of fused silica per bounce pair. The probe white-light is passed through an optical delay line on a

linear motorized stage (National Aperture) that can scan a range of 800 ps relative to the pump pulse. The pump and probe pulses are then focused onto the sample and then recollimated after the sample with 90º off-axis parabolic mirrors with a focal length of 5 cm.

Since the experiments are done in the pump-probe geometry, the desired third-order signal is emitted in the direction of the outgoing probe pulse, as discussed in Chapter 1. The probe beam is aligned onto another 90º off-axis parabolic mirror and is focused into an optical fiber (105 μm diameter, 0.22 NA). The optical fiber routes the light into a spectrograph (Princeton Instruments), that uses a diffraction grating to disperse the pulse onto a 1024-pixel linear CCD array (e2V AviivA EM4), which can read the signal out at 100 kHz allowing shot-to-shot data collection.[3] In addition, a flip mirror can be used to instead route the pump light into the optical fiber for frequency resolved optical gating (FROG), AOM calibration, or flat spectrum fitting. FROG is described in the next section, and the procedure for AOM calibration and flat spectrum fitting are described in the Appendix.

All the 2D WL spectra in this dissertation were collected with 8-frame phase cycling. The phases of the pulses for the 8 frames are listed in Table 1. For 8-frame phase-cycling the transient signal is:

$$\Delta OD = -log\frac{(I_1-I_2)(I_5-I_6)}{(I_3-I_4)(I_7-I_8)} \tag{2.1}$$

Where I_n is the number of counts on the camera for frame n. The 8-frame phase-cycling removes the scattering from the two pump pulses and transient signals from each of the pump pulses. The thin film samples that are studied in the Zanni Group scatter enough light that the 8-frame sequence does not fully remove all the scatter. To completely remove the scatter, for most experiments, spectra are measured at negative time-delays between the pump and probe pulses, and these negative time spectra are subtracted from all the positive delay time spectra. There should be no

signal at negative times, so any measured ΔOD is due to scattered light. An example of the scatter subtraction is shown in Figure 2.4.

Typical coherence times (time between the pump pulses) are 0-98 fs in 2 fs steps, with a 11,000 cm^{-1} rotating frame. In the data processing, a typical zero padding length was 512, and the free-induction decay was multiplied by a gaussian window function that had a width of 40 fs.

Table 2.1. 8-frame phase-cycling scheme

Frame	ϕ_1	ϕ_2	Probe
1	0	0	on
2	0	0	off
3	π	0	on
4	π	0	off
5	π	π	on
6	π	π	off
7	0	π	on
8	0	π	off

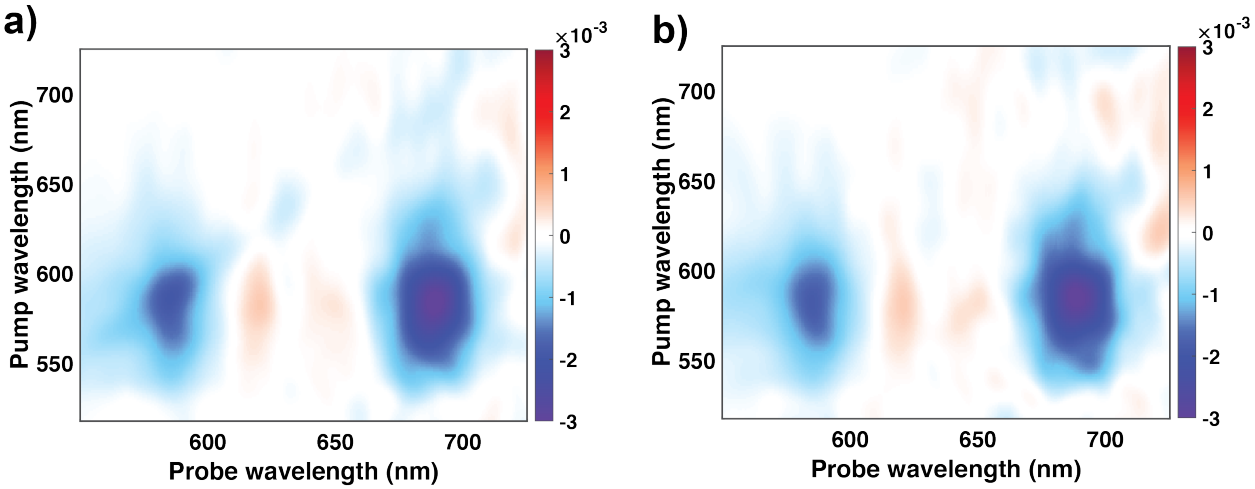

Figure 2.4. Examples of a 2D WL spectrum of a pentacene thin-film with no negative delay-time subtraction (a), and with negative delay-time subtraction (b). The scatter along the diagonal in (a) is removed with the subtraction and is not present in (b).

2.3 Frequency resolved optical gating

The method I used for measuring the spectral phase of the pump and probe white-light pulses was frequency resolved optical gating, FROG.[4] There are various types of FROG experiments, the most common of which is second-harmonic generation (SHG) FROG. SHG-FROG is not possible with the pulses used here, as the pulse energy needed for SHG is greater than the energy of these white-light pulses. Instead, polarization-gated (PG) FROG is used. For PG-FROG I used a higher power gate pulse from a noncollinear optical parametric amplifier (NOPA). The NOPA was pumped with the remaining 3 W of the fundamental and was tuned to an output of 550 nm and had a power near 40 mW. Using a half waveplate and a polarizer, the polarization of the gate pulse is set 45º relative to the pulse being measured. If the pump white-light is being measured, the NOPA pulse is aligned onto the optical delay stage. The gate pulse and the pulse that is being measured are overlapped in a piece of BK7 glass that is 1 mm thick. Any material with a short lived non-linearity ($\chi^{(3)}$) will suffice. The high-power gate pulse creates a birefringence due to the electronic Kerr effect in the material, rotating the polarization of the white-light pulse.[5] The polarization is only rotated if the white-light is in the sample at the same exact time as the gate pulse. The white-light pulse then passes through a polarizer set perpendicular to the polarization of white-light before the sample and is collected into the spectrograph. The polarizer after the sample is set so that all the unrotated white-light is filtered out, and only the light that is rotated from overlapping with the gate pulse is detected. However, in practice the polarization before the detector is only rotated 75-80º relative to the white-light so that a measurable difference can be seen. The PG-FROG setup is shown in Figure 2.5.

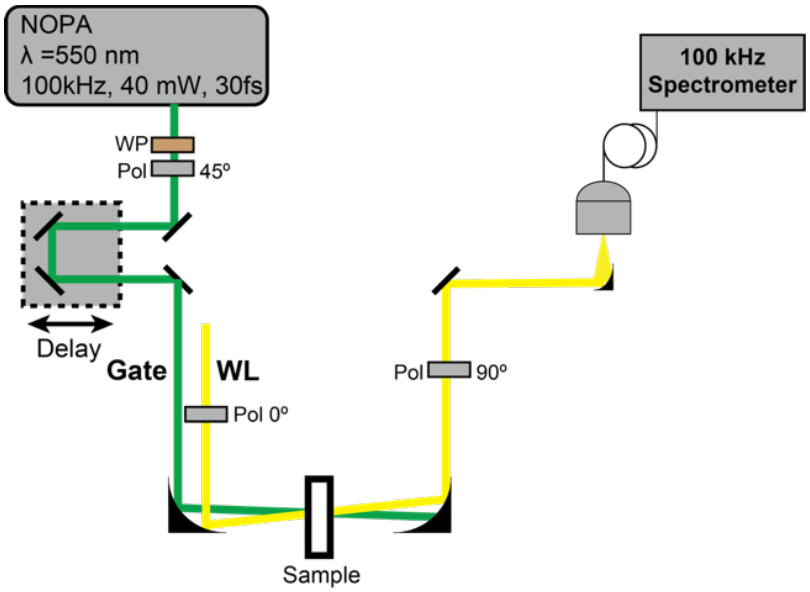

Figure 2.5. PG-FROG setup, the white-light (WL) is either of the pulses shown in Figure 2.3.

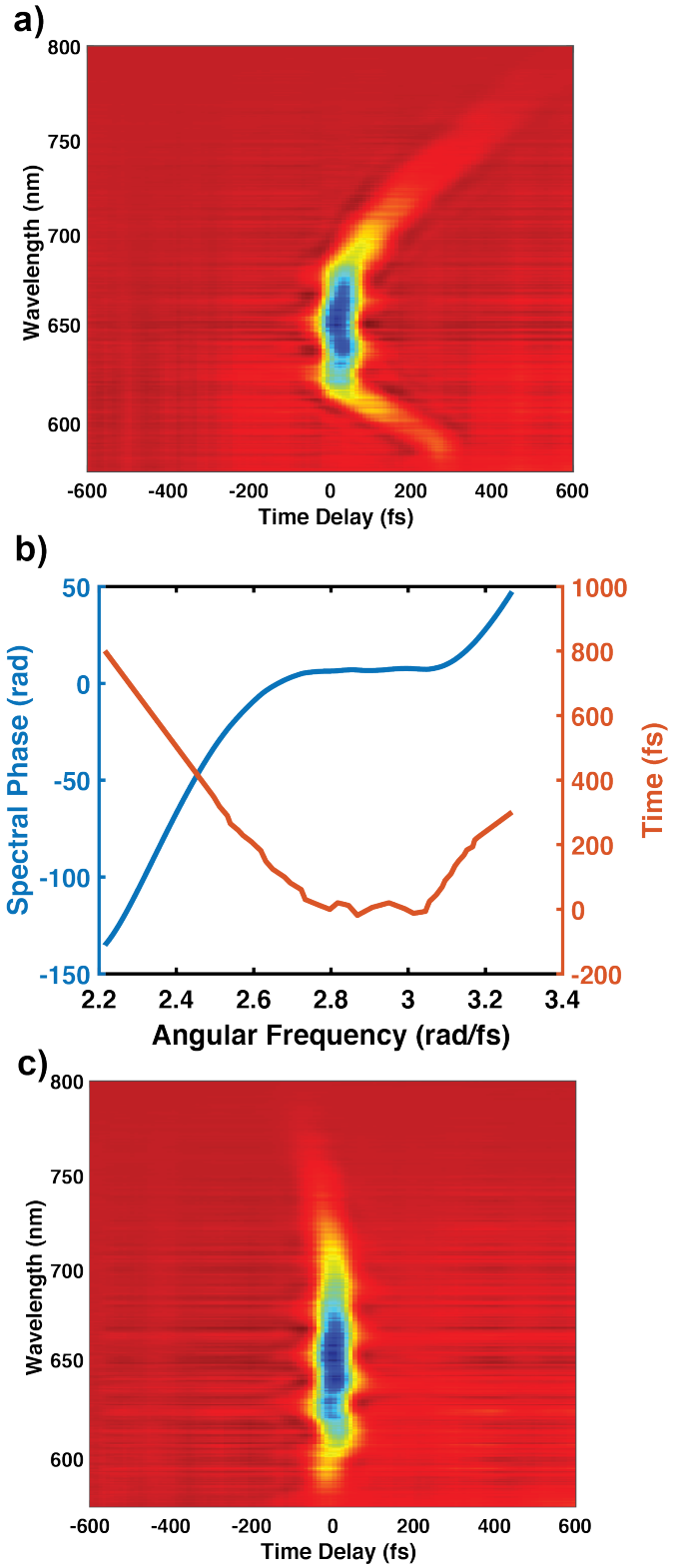

Figure 2.6. (a) FROG of the pump white-light pulse with no phase applied with the AOM. (b) The group delay (orange) and spectral phase (blue) of the pulse uncompressed pulse. (c) FROG of the pump white-light with the AOM applying the measured spectral phase to compress the pulse.

The time between the gate and white-light pulse is scanned and the spectrum of the rotated light detected at each delay, creating a spectrogram (Figure 2.6a). The spectrogram shows that certain wavelengths of light are overlapped with the gate pulse at different delays. The spectral phase of the white-light can be determined from the spectrogram. The spectrogram is essentially a plot of the group delay, which is the first derivative the spectral phase. If a plot is made of the angular frequency of the light versus the time of the maximum PG-FROG signal, the curve can be integrated to retrieve the spectral phase (Figure 2.6b). For the pump white-light, once the spectral phase is known, the pulse shaper can be used to correct for any dispersion, as described in the next chapter. Any dispersion in the probe white-light is corrected for by adding or subtracting bounces to the chirped mirror pair.

2.4 Fourier transform photothermal spectroscopy

2.4.1 Optical microscope

The shaped white-light from the pulse shaper is picked off and directed into the microscope. The microscope illuminates a sample from below using a reflective objective (50X magnification, NA = 0.65) that focus the beam to a one micron spot.[6] To view the sample from above, there is a transmissive objective above the sample (20X magnification, NA = 0.6) that both collimates the white-light pulse and focuses an LED onto the sample. The image looking from above the sample is collected in a Thorlabs CCD camera (Figure 2.7a). The sample can also be viewed from below. A beam-splitter on a magnetic mount is placed in the path of the white-light before the reflective objective so that most of the white-light is reflected off the face of the beam-splitter and a small portion is transmitted and focused onto the sample. If the white-light is focused at the sample, some portion of the light will reflect back off the sample and will go back through

the reflective objective and most of the light that reflected off the sample will be reflected off the beam-splitter, after which it is imaged with another CCD camera (Figure 2.7b). In addition to the white-light, the light that is transmitted through the sample from the LED that illuminates the sample from above will also pass through the reflective objective, reflect off the beam-splitter and show the image of the sample on the lower camera. The removable beam-splitter is only used for alignment and is removed for any spectroscopic measurement. The sample is positioned in the X and Y directions with stepper motors (Thorlabs) to identify objects to be imaged. The microscope is pictured in Figure 2.8.

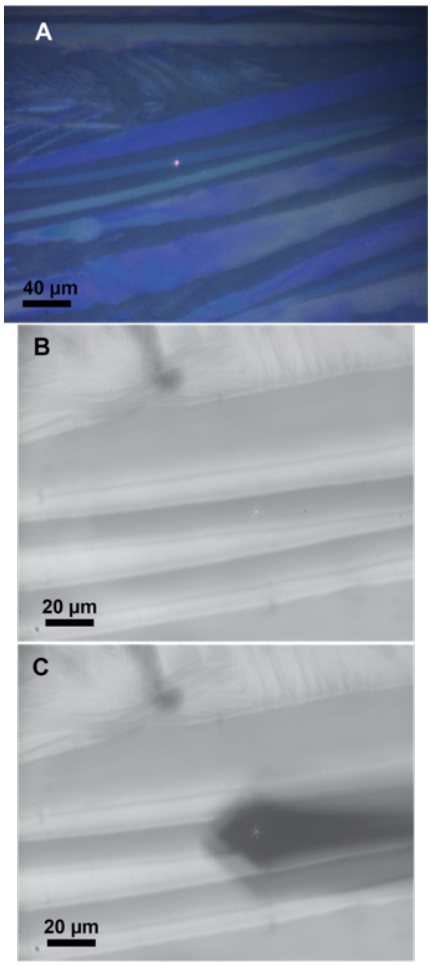

Figure 2.7. The image of TIPS-Pn microcrystals taken with the CCD camera above the sample (a), and below the sample (b). (c) shows the rough alignment of the AFM tip with the laser focus.

2.4.2 Atomic Force Microscope

The AFM used in the FTPT experiments was a refurbished VistaScope from Molecular Vista. The instrument was designed to easily couple optical experiments into the AFM. The AFM has three main components: the AFM head, the sample stage, and the control and feedback electronics. The sample stage, which sits on top of the coarse control described in the previous section, is a piezo-electric stage that has X, Y, and Z control. The range of X and Y is 30 μm with 24-bit resolution, and the range of the sample Z control is 8 μm with 24-bit resolution.

The AFM head contains many smaller components, one of which is the AFM cantilever. The cantilever used for all the FTPT experiments is HQ:NSC14/Pt from MikroMasch. The cantilevers are all slightly different, even within a single box. The length of the cantilevers is approximately 125 μm, the force constant is 5 N/m, the free resonance is 160 kHz, and the radius of the tip is <30 nm. The voltage on the AFM four quadrant photodetector (4QPD) due to the 910 nm continuous wave AFM laser reflecting off the back of the cantilever is between 800-900 mV when the cantilever is properly mounted, and the AFM laser is properly aligned. The entire AFM and microscope sit on an active vibration control platform and are enclosed to minimize noise from the environment.

2.4.3 FTPT procedure

The first step in FTPT aside from aligning an AFM tip and aligning the white-light through the pulse shaper and to the microscope, is to ensure that the white-light is aligned directly beneath the AFM tip. The AFM tip has a radius much smaller than the diameter of the focused white-light beam (30 nm versus 1 μm), which means there is some leniency in the alignment, but it is still not possible to consistently align the tip to the white-light spot by eye. When the AFM cantilever is near the surface of the sample, the shadow of the cantilever is visible in the bottom camera of the

microscope, as is the back-reflection of the white-light laser spot. Using this bottom camera, the position of the AFM head is adjusted so that the AFM cantilever is above the white-light spot, as shown in Figure 2.7c. Once the AFM tip and white-light have been roughly aligned, the AFM tip is put in contact with the sample. With the sample and AFM stationary, the X-Y position of the reflective objective is scanned 10x10 µm, with a 128-pixel resolution. A very slow scan rate is used (0.025-0.05 line/sec) so that each pixel has enough time to average. The 4QPD voltage at the detection frequency, which is set to the repetition rate of the laser, is plotted (Figure 2.9). The objective is set to the position of the maximum voltage of the 4QPD at the detection frequency. Slight corrections can be made to the Z-position (focus) of the objective to maximize the voltage.

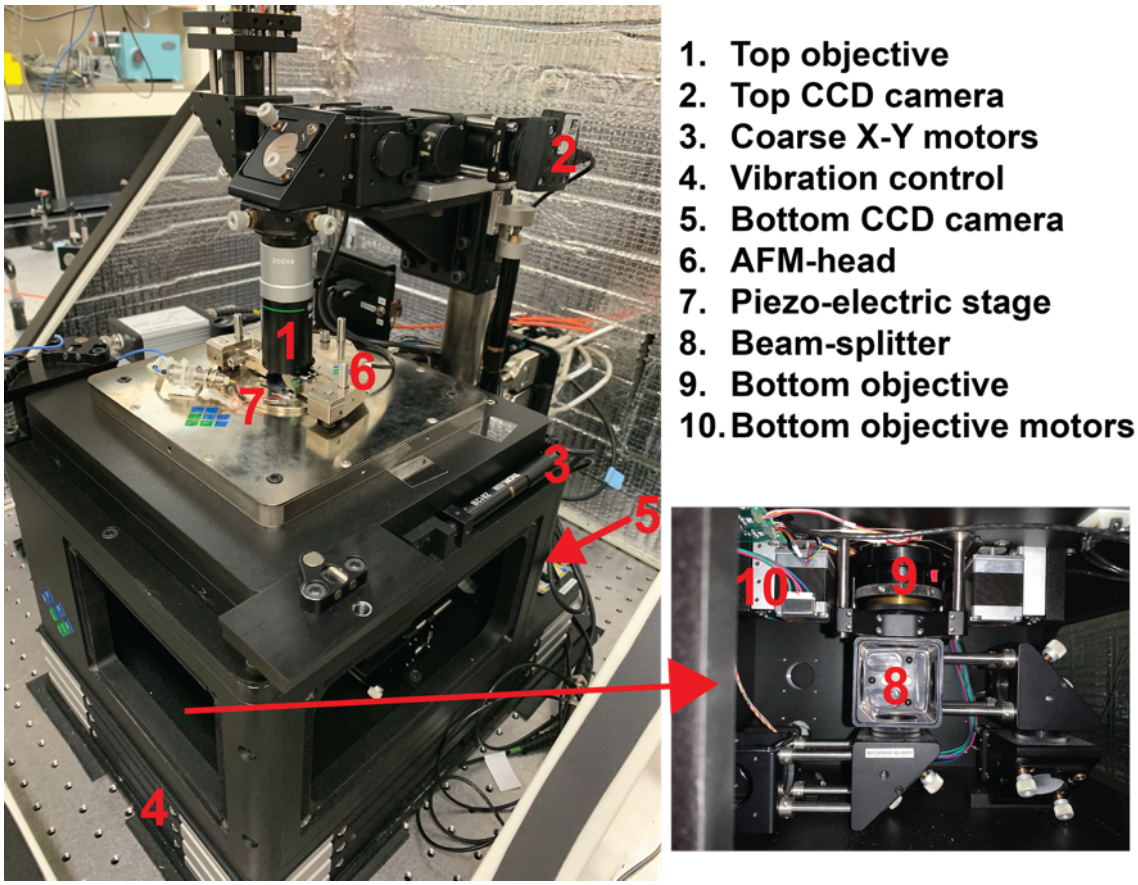

Figure 2.8. Diagram of optical microscope

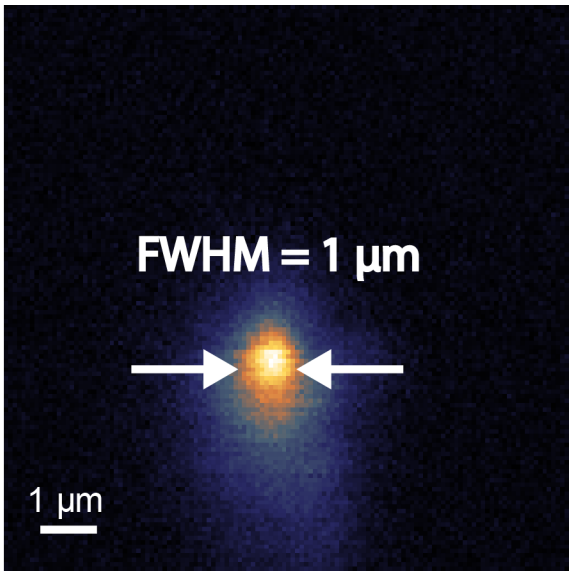

Figure 2.9. Image of the white-light focus from measuring the photothermal expansion as a function of the objective position.

Once the AFM tip and objective positions have been set, the output from the 4QPD is routed to a Zurich Instruments UHFLI 600 MHz lock-in amplifier (Figure 2.10). The amplifier also contains a boxcar integrator, which is used for the FTPT spectrum. The 4QPD voltage is routed to Signal Input 1, a pulse from the light source electronics at the repetition rate of the laser is directed to Trigger 1, and a pulse marking the beginning of the AWG mask sequence is directed to Trigger 2. The UHFLI is set so that it plots the 10 µs window of the 4QPD input between consecutive 100 kHz triggers. This output is shown in Figure 2.11a. There is significant electronic signal even when there is no light interacting with the sample, and therefore no cantilever oscillations. These background electronic signals have not been fully characterized but are most likely due to reflections of the trigger pulses in the BNC cables. In addition, if the AOM from the pulse shaper is not electrically isolated from the table, electronic signals from the amplified RF pulses can be seen. This is avoided by placing the AOM on a 5 mm thick plastic insulator. The 10 µs 4QPD window is collected with and without the light interacting with the sample, and the electronic background is subtracted off to get the AFM cantilever oscillations. The boxcar

integration window is set to integrate the most intense half-period of the AFM oscillations (Figure 2.11b).

Figure 2.10. Zurich Instruments UHFLI used for the FTPT experiments. The left most input is the 4QPD signal. The first trigger, shown in trigger input one with a T-joint, is the 100 kHz trigger from the laser electronics. The second trigger, the furthest on the right, is the trigger marking the beginning of each mask sequence from the AWG.

After the integration window is set, a FTPT spectrum can be measured. The AWG mask sequence is updated to scan the time between the two white-light pulses from 0-63 fs, in 1 fs steps. A rotating frame of 11,000 cm^{-1} is set, each time delay is repeated 10 times in a row, and the amplitude at each AWG pixel is set so that the outgoing pulse-pair has a flat spectrum. Each time delay is repeated 10 times to mitigate that the AFM cantilever oscillates for approximately 60 µs, but a new laser pulse arrives every 10 µs. The necessity of the 10 repeated delays is further discussed in Chapter 5. The marker trigger from the AWG triggers the start of each FID average, and the FID is typically averaged 250,000 to 1,000,000 times, for a collection time of approximately 2.5-10 minutes. Different time-delays and rotating frames can be used, but the values listed above were used for all FTPT spectra presented in this dissertation.

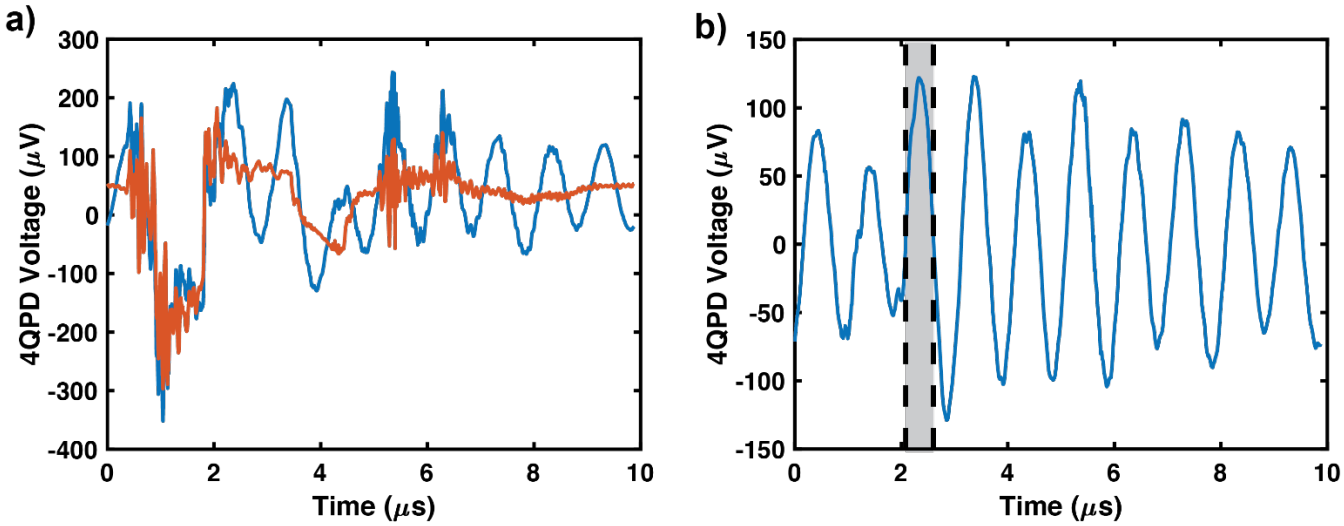

Figure 2.11. The raw 4QPD output from the Zurich UHFLI (a) with the light hitting the sample (blue) and not hitting the sample (orange). If the electronic noise is subtracted from the 4QPD signal, the AFM cantilever oscillations can be seen (b), and the integration window set (gray rectangle).

2.4.4 Photothermal imaging

Photothermal imaging in its current form does not require the use of the UHFLI. After the location of the AFM tip and objective are set, while the AFM tip is in contact and in Contact Mode, the sample is scanned beneath the AFM tip, as would be done for a topography image. The photothermal expansion is collected simultaneously with the topography by saving the amplitude of the 4QPD at the detection frequency (which is set to the repetition rate of the laser). The scan rate of the sample is set slow enough so that each pixel averages for 20-100 ms, which results in the image time being 45 minutes to 3 hours for a 256x256 pixel image where the forward and backward traces are collected.

2.5 References

(1) Nite, J. M.; Cyran, J. D.; Krummel, A. T. Active Bragg Angle Compensation for Shaping Ultrafast Mid-Infrared Pulses. *Opt. Express, OE* **2012**, *20* (21), 23912–23920. https://doi.org/10.1364/OE.20.023912.
(2) Kearns, N. M. Development of Ultrabroadband Nonlinear Spectroscopy and Microscopy with Applications to Materials Systems. Ph.D., The University of Wisconsin - Madison, United States -- Wisconsin.
(3) Kearns, N. M.; Mehlenbacher, R. D.; Jones, A. C.; Zanni, M. T. Broadband 2D Electronic Spectrometer Using White Light and Pulse Shaping: Noise and Signal Evaluation at 1 and 100 KHz. *Opt. Express, OE* **2017**, *25* (7), 7869–7883. https://doi.org/10.1364/OE.25.007869.
(4) Trebino, R. *Frequency-Resolved Optical Gating: The Measurement of Ultrashort Laser Pulses*, 1st ed.; Springer: Boston, MA.
(5) Trebino, R.; DeLong, K. W.; Fittinghoff, D. N.; Sweetser, J. N.; Krumbügel, M. A.; Richman, B. A.; Kane, D. J. Measuring Ultrashort Laser Pulses in the Time-Frequency Domain Using Frequency-Resolved Optical Gating. *Review of Scientific Instruments* **1997**, *68* (9), 3277–3295. https://doi.org/10.1063/1.1148286.
(6) Jones, A. C.; Kearns, N. M.; Bohlmann Kunz, M.; Flach, J. T.; Zanni, M. T. Multidimensional Spectroscopy on the Microscale: Development of a Multimodal Imaging System Incorporating 2D White-Light Spectroscopy, Broadband Transient Absorption, and Atomic Force Microscopy. *J. Phys. Chem. A* **2019**, *123* (50), 10824–10836. https://doi.org/10.1021/acs.jpca.9b09099.

3. Dual spectral phase and diffraction angle compensation of a broadband AOM 4-f pulse-shaper for ultrafast spectroscopy.

AOM-based pulse shaping as a method has been shown to provide many advantages in the field of ultrafast spectroscopy, in particular for the creation of phase matched pulse pairs for two-dimensional IR and electronic spectroscopy. In this paper we demonstrate the capabilities of a quartz-based AOM pulse-shaper to provide fine control over the phase and spatial dispersion of ultrafast supercontinuum pulses. We show that by using the Bragg condition, we can define a mask function for our AOM such that the angle of diffraction is constant for all frequencies. By summing all the contributions to spectral phase due to normal and anomalous dispersion of our optical components, and taking into account the intrinsic frequency dependent phase as a result of the acoustic sine wave propagating through the AOM, we can determine an optimal mask function that meets the Bragg condition for all frequencies, and generates compressed (~50 fs) supercontinuum pulses.

Acknowledgments

The research in this chapter was done in collaboration with Andrew C. Jones. ACJ contributed the calculations, and to the analysis and manuscript writing. I completed the experiments, and to the analysis and manuscript writing. Reprinted from *Optics Express*. Copyright 2019 Optical Society of America. https://doi.org/10.1364/OE.27.037236

3.1 Introduction

The emergence of multidimensional spectroscopy techniques has represented a valuable advance towards the characterization of the ultrafast temporal response of materials [1–4]. Through the characterization of the coupling between electronic states (Two-Dimensional Electronic Spectroscopy (2DES)), vibrational states (Two-Dimensional Infrared Spectroscopy (2DIR)), and electronic-vibrational coupling (Two Dimensional Electronic-Vibrational Spectroscopy (2DEV/2DVE)), multidimensional spectroscopy techniques are a powerful tool in characterizing the electronic and structural properties which govern the dynamic response of a material to optical excitation. A wide-variety of experimental geometries of varied complexity are possible in carrying out multidimensional spectroscopic characterization, as the measurement requires the detection of the four wave mixing signal (FWM), which is the result of the interaction of two pump pulses, a probe pulse, and interference with a local oscillator [5]. There are many ways that are used to create the pump pulse pair, including Michelson interferometers [6] or birefringent wedge pairs [7]. One approach which significantly simplifies the experimental geometry is the implementation of a pulse-shaping system which allows for multidimensional spectra to be recorded with a simple pump-probe beam geometry [8–10].

While a number of different pulse-shapers including SLM and AOPDF based systems are available [11,12], AOM-based 4-f pulse-shaping systems are commonly used as they can be applied in both the visible [13] and mid-IR [8,14] spectral ranges and are capable of shaping on a shot-to-shot basis at repetition rates up to 100 kHz [13,15]. For these AOM-based shapers, diffraction of light from a precisely timed, phase and amplitude controlled acoustic wave launched across a large acoustic aperture enables the measurement of 2DES via control over the corresponding phase and amplitude of the diffracted light [13]. Such control allows for

characterization of materials over a broad spectral range in the visible [16]. The operating mechanism of these shapers necessitates transmission through relatively thick (~10-20 mm) acousto-optic crystals (TeO_2, SiO_2, Ge) of materials which can be highly dispersive. While the amount of material in an AOM is smaller than an AOPDF, the dispersion created by the material needs to be removed for optimally compressed pulses. The AOM has a finite acoustic bandwidth, and can compensate for spectral phase across a broad bandwidth pulse within that limit, but at some point the spectral bandwidth will exceed the AOM's ability to compensate for dispersion created by its own acousto-optic crystal. One way to extend that limit is by using prisms or chirped mirrors. A second consideration is that the angle of diffraction from the acoustic waveform within the AOM is directly linked to the spectral phase compensation mask defined by the user. While providing spectral phase compensation may result in temporal compression of an ultrafast pulse, it may also result in unwanted spatial dispersion of the beam.

In the sections below we detail the development and implementation of a broadband quartz-based 4-f pulse shaper system operating in the visible spectral range across a broad bandwidth and globally optimized for both temporal compression of the optical pulse and diffraction at the Bragg angle. Here, we develop a model for the dispersive contributions associated with normal and anomalous dispersive contributions within the beampath in addition to the dispersion of the 4-f AOM pulse-shaper itself, which reveals a complex relationship between the spectral phase mask applied by the user and the relative angle of diffraction of the outgoing shaped beam. While quartz was chosen as a demonstration material for the visible spectral range due to its comparatively low amount of dispersion, the modeling of the spectral phase contributions and diffraction can be extended to any 4-f AOM pulse shaping system.

3.2 Experimental apparatus for broadband pulse shaping of White-Light Supercontinua

In contrast to ultrafast laser and parametric amplification light sources whose spectral bandwidth is limited by the lasing gain and phase matching conditions respectively, the broadband spectral distribution available from supercontinuum generation is a significant advantage in the characterization of the ultrafast response of materials over a large energy range [17]. To generate an ultrabroadband supercontinuum spectrum which spans the visible spectral range, we utilize white-light (WL) generation via filamentation of μJ-scale pulses from an Yb-based laser amplifier ($\boldsymbol{\lambda = 1050}$ nm) in a solid-state YAG crystal ($\boldsymbol{L_{YAG}}$ =8 mm) to create a continuous spectral distribution in the visible with wavelengths ranging down to ~500 nm [18,19]. While the process of WL generation is relatively inefficient, the relative pulse-to-pulse noise of the WL is only fractionally larger than that of the fundamental laser source [20], while the ~nJ pulse-energies of the visible component of the spectrum is still sufficient for many ultrafast spectroscopy applications.

Prior to the pulse-shaping system, in order to provide additional dispersion control, the WL is sent through a chirped mirror compressor system (Layertec GmbH 103367) with the number of bounce-pairs determined by the desired level of dispersion pre-compensation. The pulse-shaper system implemented here follows a traditional 4-f acousto-optic modulator (AOM) based shaper geometry [8,11] with the AOM crystal itself being composed of quartz with a thickness of $\boldsymbol{L_{AOM} = 20}$ mm. This AOM is paired with 600 lines/mm reflection gratings and single-axis parabolic mirrors of focal length of $\boldsymbol{f = 150}$ mm to form the complete shaper system as depicted in Figure 3.1(a).

3.3 Broadband Dispersion Compensation of a Quartz-based AOM Pulse-shaping System

The temporal duration and dispersion of an optical pulse can be manipulated via the spectral phase with the electric field, $\boldsymbol{E}$, expressed as:

$$\boldsymbol{E(\omega) = \sqrt{S(\omega)} \cdot e^{-i\psi(\omega)}} \tag{3.1}$$

Here, $\boldsymbol{S(\omega)}$ and $\boldsymbol{\psi(\omega)}$ represent the spectral intensity and phase, respectively. $\boldsymbol{\psi(\omega)}$ is often expressed in terms of a Taylor expansion using terms associated with the group-delay ($\boldsymbol{\psi_1}$, GD), 2nd order group-delay dispersion ($\boldsymbol{\psi_2}$, GDD), 3rd order ($\boldsymbol{\psi_3}$, TOD), 4th order ($\boldsymbol{\psi_4}$, FOD), …to nth order ($\boldsymbol{\psi_n = \frac{\partial^n \psi}{\partial \omega^n}}$) dispersion.

$$\begin{aligned} \boldsymbol{\psi(\omega)} \quad = \quad & \boldsymbol{\psi_0 + \psi_1 \cdot (\omega - \omega_0) + \frac{\psi_2}{2} \cdot (\omega - \omega_0)^2} \\ & \boldsymbol{+ \frac{\psi_3}{6} \cdot (\omega - \omega_0)^3 + \frac{\psi_4}{24} \cdot (\omega - \omega_0)^4 + \ldots} \end{aligned} \tag{3.2}$$

The net spectral phase at the measurement location, $\boldsymbol{\psi_{Net}}$, represents the superposition of the various dispersive elements within the experimental apparatus. These elements represent either normal dispersion for which the derivative of the propagation time, $\boldsymbol{\tau = \frac{\partial \psi}{\partial \omega}}$, is positive $\boldsymbol{\frac{\partial \tau}{\partial \omega} > 0}$, or anomalous dispersion for which the derivative of the propagation time is negative, $\boldsymbol{\frac{\partial \tau}{\partial \omega} < 0}$.

For a given spectrum, a flat spectral phase distribution is required to achieve a temporally compressed, Fourier-limited pulse duration. For broadband applications in the visible spectral range, where transmissive materials in the optical beampath can add large amounts of dispersion, precise compensation of 2nd and higher order dispersive terms over the entire spectral bandwidth of the optical pulse can be particularly challenging. To this end, the ability of a pulse-shaping system to apply a user-defined compensatory mask as a means of providing targeted compensation

of residual spectral phase contributions represents a powerful tool in optimizing the temporal compression of an optical pulse. Imposition of a user-defined spectral amplitude and phase mask, $\boldsymbol{M(\omega)}$, to generate a custom outgoing shaped electric field, $\boldsymbol{E'(\omega)}$, is often expressed in frequency space in terms of the spectral amplitude, $\boldsymbol{|M(\omega)|}$, and phase, $\boldsymbol{\psi_M(\omega)}$,of the applied mask [11]:

$$\boldsymbol{E'^{(\omega)} = M(\omega) \cdot E(\omega) = |M(\omega)| E(\omega) \cdot e^{-i\psi_M(\omega)}} \tag{3.3}$$

For an AOM-based pulse-shaping system, $\boldsymbol{\psi_M(\omega)}$ is applied through the diffraction of an optical pulse from periodic refractive index modulations associated with a traveling RF acoustic wave within the AOM crystal [21,22]. As shown by the schematic in Figure 3.1(a), an acoustic wave with a characteristic center frequency, $\mathbf{f_0}$, is launched by a transducer over a fixed time window representing the duration of the acoustic wave, $\mathbf{T_A}$. The general form of the acoustic wave, $\boldsymbol{\mathcal{A}}$, can be expressed in terms of temporally varying acoustic amplitude, $\mathbf{a(t_A)}$, and instantaneous phase, $\boldsymbol{\Phi_A(t_A)}$, terms [14].

$$\boldsymbol{\mathcal{A}(t_A) = a(t_A) \cdot \sin(\Phi_A(t_A)) = a(t_A) \cdot \sin(2\pi f_0 t_A + \Psi_A(t_A))} \tag{3.4}$$

Here, $\mathbf{t_A}$ represents the relative timing of the acoustic transducer output and $\boldsymbol{\Psi_A(t_A)}$ the phase associated with application of the user-defined phase mask. The AOM transducer frequency required to implement a given phase shift is defined by a corresponding instantaneous frequency, $\boldsymbol{\nu_{A,in}}$ [14]:

$$\boldsymbol{\nu_{A,in}(t_A) = \frac{d\Phi_A}{dt_A} = 2\pi f_0 + \frac{d\Psi_A(t_A)}{dt_A}} \tag{3.5}$$

For the 4-f AOM-based pulse-shaper depicted in Figure 3.1(a), the light incident upon the AOM travels with a vertical projection along the direction of the acoustic wave resulting in -1 order diffraction and a negative frequency/phase being applied to the diffracted pulse [23].

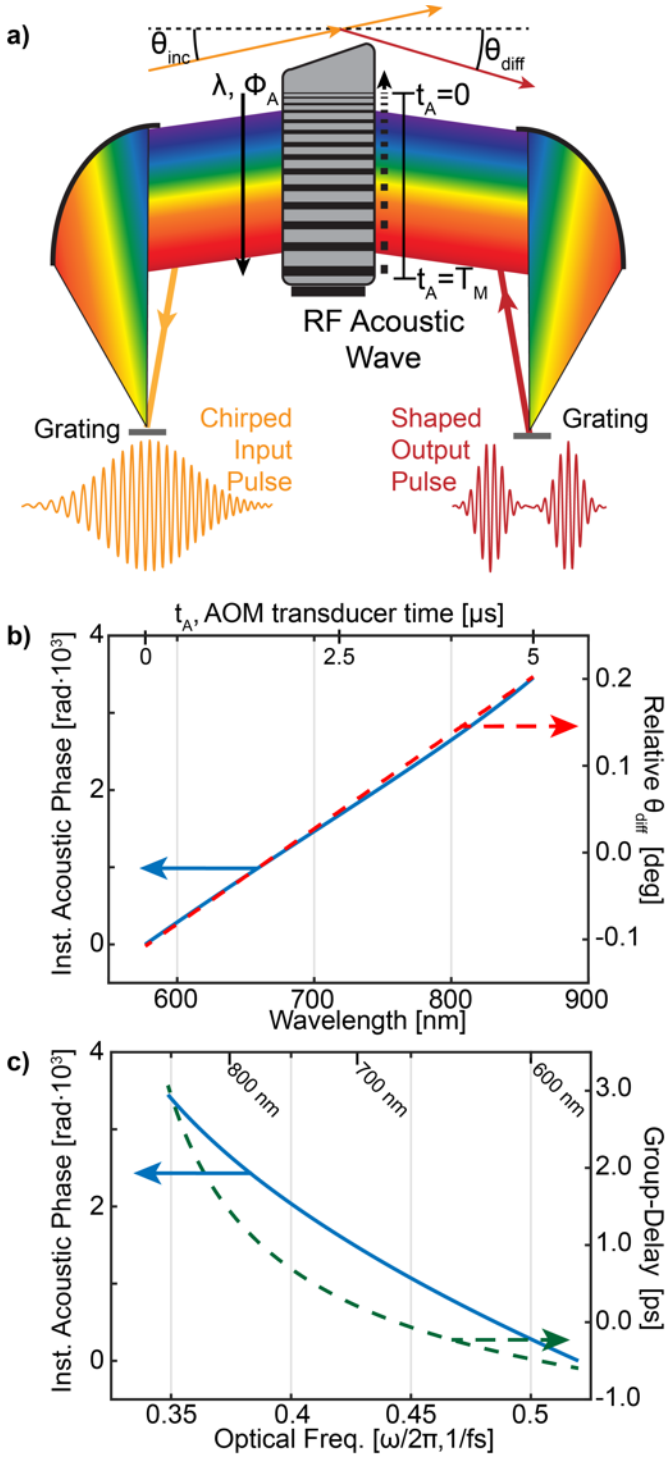

Figure 3.1. The 4f-AOM geometry relating the λ and ω parameters of the incident light with t_A of the acoustic wave are represented within a) with incoming light represented by the orange lines/arrows and the outgoing diffracted light represented by the red lines/arrows. The linear scaling of instantaneous acoustic phase, $\Phi_A(t_A)$, with λ is depicted in b) (blue solid line) with the associated variation of the relative angle of diffraction (red dashed line). Panel c) exhibits the non-linear relationship between Φ_A and ω (blue solid line), with the associated non-linear group-delay resulting from a -1 order diffraction process (green dashed line).

Following previous works [20], $|\boldsymbol{M}(\boldsymbol{\omega})|$ and $\boldsymbol{\psi_M}(\boldsymbol{\omega})$ in Eq. (3.4) can directly be linked to the amplitude, $\mathbf{a}(\mathbf{t_A})$, and phase $\mathbf{\Psi_A}(\mathbf{t_A})$ of the traveling acoustic wave within the AOM. This relationship is established by linking the relative timing of the transducer output $\mathbf{t_A}$ with the optical frequency $\boldsymbol{\omega}$ traveling through the AOM using a polynomial expansion:

$$\boldsymbol{\omega}(\mathbf{t_A}) = \mathbf{c_0} + \mathbf{c_1 t_A} + \mathbf{c_2 t_A}^2 \tag{3.6}$$

Here, $\mathbf{c_n}$ represents the calibration constants whose values capture the linear scaling of optical wavelengths, $\boldsymbol{\lambda}$, across the acoustic aperture of the AOM [20]. As a consequence of this scaling, both $\boldsymbol{M}$ and $\boldsymbol{\psi_M}$, may be expressed in terms of the timing of the transducer output:

$$\begin{array}{rcl} |\boldsymbol{M}(\boldsymbol{\omega}(\mathbf{t_A}))| & = & \mathbf{a}(\mathbf{t_A}) \\ \boldsymbol{\psi_M}(\boldsymbol{\omega}(\mathbf{t_A})) & = & \pm\mathbf{\Psi_A}(\mathbf{t_A}) \end{array} \tag{3.7}$$

with the sign determined by the order of diffraction.

Using Eq. (3.**Error! Reference source not found.**) to express phase as a function of **ω** r ather than $\mathbf{t_A}$, we can relate the net spectral phase applied by the pulse-shaper, $\boldsymbol{\phi_M}(\boldsymbol{\omega})$, directly to the instantaneous phase of the transducer output, $\mathbf{\Phi_A}(\mathbf{t_A})$:

$$\boldsymbol{\phi_M}(\boldsymbol{\omega}) = \boldsymbol{\psi_{M,\mathbf{sin}}}(\boldsymbol{\omega}) + \boldsymbol{\psi_M}(\boldsymbol{\omega}) = \pm\mathbf{\Phi_A}(\mathbf{t_A}(\boldsymbol{\omega})) \tag{3.8}$$

$\boldsymbol{\phi_M}$ thus exists as the superposition of two terms: $\boldsymbol{\psi_M}$, which represents the user-defined spectral phase, and $\boldsymbol{\psi_{M,\mathbf{sin}}}$, an additional spectral-phase contribution associated with a flat-phase sinusoidal wave within the AOM. Using Eq. (3.4) and (3.8), both of these phase contributions can be expressed in terms of the acoustic wave as:

$$\begin{array}{rcl} \boldsymbol{\psi_{M,\mathbf{sin}}}(\boldsymbol{\omega}) & = & \pm\mathbf{2\pi f_0 t_A}(\boldsymbol{\omega}) \\ \boldsymbol{\psi_M}(\boldsymbol{\omega}) & = & \pm\mathbf{\Psi_A}\big(\mathbf{t_A}(\boldsymbol{\omega})\big) \end{array} \tag{3.9}$$

The origin of dispersion associated with a single-frequency sinusoidal wave traveling through the AOM, $\boldsymbol{\psi_{M,\mathbf{sin}}}$, originates from the linear scaling of wavelength across the acoustic aperture of the AOM. As seen in Figure 3.1(b,c) the linear scaling of the acoustic phase as a

function of wavelength results in a non-linear group-delay as a function of $\boldsymbol{\omega}$ due to significant higher-order dispersive contributions from $\boldsymbol{\psi_{M,\sin}}$ [20]. Following Eq. (3.6) for the 4-f AOM shaper geometry detailed above, the following calibration constants mapping the timing of the acoustic waveform to the optical frequency were measured: $\mathbf{c_0 \cong 3.26\ rad \cdot PHz}$, $\mathbf{c_1 \cong -3.13 \cdot 10^5\ rad \cdot PHz/s}$, and $\mathbf{c_2 \cong 1.96 \cdot 10^{10}\ rad \cdot PHz/s^2}$. By performing a Taylor expansion about a central optical angular frequency, $\boldsymbol{\omega_0}$, the higher order dispersive terms associated with the instantaneous phase of a sinusoidal wave with acoustic frequency, $\mathbf{f_0}$, may easily be determined.

$$\mathbf{2\pi f_0 t_A}(\boldsymbol{\omega}) = \boldsymbol{\psi_{M\sin,0}} + \boldsymbol{\psi_{M\sin,1}}(\boldsymbol{\omega} - \boldsymbol{\omega_0}) + \frac{\boldsymbol{\psi_{M\sin,2}}}{\mathbf{2}}(\boldsymbol{\omega} - \boldsymbol{\omega_0})^2 + \frac{\boldsymbol{\psi_{M\sin,3}}}{\mathbf{6}}(\boldsymbol{\omega} - \boldsymbol{\omega_0})^3 + \frac{\boldsymbol{\psi_{M\sin,4}}}{\mathbf{24}}(\boldsymbol{\omega} - \boldsymbol{\omega_0})^4 \ldots \quad (3.10)$$

Provided the calibration constants above, performing the expansion in Eq. (3.10) reveals spectral phase contributions associated with a flat sinusoidal wave to be $\boldsymbol{\psi_{M\sin,2}}$ = -1580 fs^2, $\boldsymbol{\psi_{M\sin,3}}$ = 4,390 fs^3, and $\boldsymbol{\psi_{M\sin,4}}$ = -27100 fs^4. These dispersive terms are significant with respect to the normal dispersion of the quartz AOM itself, which with a thickness of 20 mm for a center wavelength of $\boldsymbol{\lambda = 675}$ nm provides a normal dispersion of approximately: $\boldsymbol{\psi_{ND,2} = 1100}$ fs^2, $\boldsymbol{\psi_{ND,3} = 570}$ fs^3, and $\boldsymbol{\psi_{ND,4} = -65}$ fs^4. It is notable that, $\boldsymbol{\psi_{M\sin,2}}$, slightly overcompensates for the positive 2nd order normal dispersion, $\boldsymbol{\psi_{ND,2}}$, due to transmission through the AOM material. Conversely, the third-order spectral phase terms $\boldsymbol{\psi_{M\sin,3}}$ and $\boldsymbol{\psi_{ND,3}}$ are both positive and sum constructively. Thus, in order to temporally compress an optical pulse, the user must define and apply an additional phase mask $\boldsymbol{\psi_M}$ primarily consisting a large negative 3rd and positive 4th order spectral phase terms, $\boldsymbol{\psi_{M,3}}$ and $\boldsymbol{\psi_{M,4}}$ respectively, as a means of cancelling out the residual spectral phase associated with the sinusoidal acoustic wave.

3.4 Global Balancing of Dispersion Compensation and Diffraction Angle for AOM-based Pulse-shaping Systems

While an AOM pulse shaping system can be used to compensate for large amounts of dispersion over a wide optical bandwidth, the $\boldsymbol{\nu_{A,in}}$ necessary to apply a given $\boldsymbol{\psi_M}$ intrinsically affects the angle of diffraction $\boldsymbol{\theta_{diff}}$. As such, the balancing of temporal compression with the associated variation of the diffraction angle by the AOM represents an additional consideration in the global optimization of the pulse shaping system.

In order for light diffracted by the acoustic wave-front within the AOM to constructively interfere, the relationship between the incident, $\boldsymbol{\theta_{inc}}$, and diffracted, $\boldsymbol{\theta_{diff}}$, angles must meet the following condition:

$$\boldsymbol{\sin\theta_{inc} + \sin\theta_{diff} = \frac{m\lambda f}{V_A}} \tag{3.11}$$

with m an integer representing the order of diffraction, $\mathbf{f}$ the acoustic frequency, and V_A the acoustic velocity of the AOM medium. When operating in the Bragg regime with a long interaction length between the optical wave-front and the acoustic-wave, conservation of momentum requires that the incoming and outgoing optical wave-fronts be approximately equal $\boldsymbol{\theta_{inc} = \theta_{diff}}$ in order for efficient diffraction to occur. This is known as the Bragg condition with the corresponding Bragg angle defined as:

$$\begin{aligned} \boldsymbol{\theta_B} &= \boldsymbol{\operatorname{asin}\left(\frac{m\lambda f}{2 V_A n(\lambda)}\right)} \\ &= \boldsymbol{\operatorname{asin}\left(\frac{\pi c}{\omega}\cdot\frac{mf}{V_A n(\omega)}\right)} \end{aligned} \tag{3.12}$$

with $\boldsymbol{n(\omega)}$ the frequency/wavelength dependent index of refraction of the AOM medium.

Examining Eq. (3.11), while $\mathbf{f}$ is variable, its value is typically chosen to match the instantaneous frequency $\boldsymbol{\nu_{A,inst}}$ required to precisely compensate for residual dispersion. $\boldsymbol{\theta_{inc}}$ is

typically fixed for the 4-f shaper implying that while AOM masks are capable of providing large amounts of dispersion compensation, the variation of $\mathbf{v_{A,inst}}$ necessary to achieve these phase masks may result in angular dispersion of the outgoing diffracted beam. Even for the case of diffraction from a flat-sinusoidal acoustic wave, the large optical bandwidth covered by the AOM pulse-shaper can result in significant variation of $\boldsymbol{\theta}_{\mathbf{diff}}$ as illustrated in Figure 3.1(b).

As imposition of $\boldsymbol{\psi_M}$ affects relative frequency of the AOM waveform, the application of an additional user-defined phase can either increase or reduce the spectral variance of $\boldsymbol{\theta}_{\mathbf{diff}}$. While the variation of angular diffraction can be compensated to minimize spatial dispersion at the sample, it is generally preferable and experimentally easier to operate with a phase mask that diffracts all wavelengths of light at an identical angle. The acoustic waveform which corresponds to this condition is known as a Bragg mask [14].

To achieve a constant $\boldsymbol{\theta}_{\mathbf{diff}}$ across the acoustic aperture of the AOM, it is necessary that the acoustic waveform satisfies the Bragg condition for each optical frequency. As discussed by Nite et al., this Bragg mask may be achieved by re-expressing Eq. (3.12) to define a constant *C* associated with diffraction a Bragg angle corresponding to the central optical frequency, $\boldsymbol{\omega_0}$, and center acoustic frequency $\mathbf{f_0}$ [14]:

$$\boldsymbol{C = 2v_A \sin(\theta_B) = \frac{2\pi c}{\omega_0}\frac{m f_0}{n(\omega_0)}} \tag{3.13}$$

Utilizing the notation for the acoustic wave used in the previous section, this constant may be used to determine the AOM's Bragg phase mask which diffracts all optical frequencies at the same angle as $\boldsymbol{\omega_0}$:

$$\begin{aligned} \frac{2\pi c}{\omega}\frac{f_B(\omega)}{n(\omega)} &= \boldsymbol{C} \\ \rightarrow \boldsymbol{f_B(\omega)} &= \frac{\omega}{\omega_0}\frac{m f_0 n(\omega)}{n(\omega_0)} \end{aligned} \tag{3.14}$$

Having established an instantaneous frequency, $\boldsymbol{\nu_{A,Bragg}(t_A) = f_B(\omega(t_A)}$, for the AOM acoustic waveform which satisfies the Bragg condition, and with the understanding from Eq. (3.5) that each waveform can be also expressed in terms of an additional user-defined spectral phase mask, the relationship between $\boldsymbol{\theta_{diff}}$ and the $\boldsymbol{\psi_M}$ can now be explored. To establish this connection, we both simulate and experimentally measure diffraction from a quartz AOM following the geometry depicted in Figure 3.2(a).

First, using the Bragg angle of incidence for a center wavelength of $\boldsymbol{\lambda = 675}$ nm ($\boldsymbol{\theta = 0.37}$°), the optical constants of quartz, and the $\boldsymbol{c_n}$ calibration parameters for the AOM noted above, Figure 3.2(b) displays the expected relative variation of the angle of diffraction. Again, we note that even a flat sinusoidal acoustic wave results in a significant variation in $\boldsymbol{\theta_{diff}}$. Using $\boldsymbol{\psi_M}$ to apply additional negative GDD acts to further increase the variation of $\boldsymbol{\theta_{diff}}$. Conversely, using $\boldsymbol{\psi_M}$ to apply positive GDD can negate and even reverse the sign of the relative variation with respect to the center wavelength.

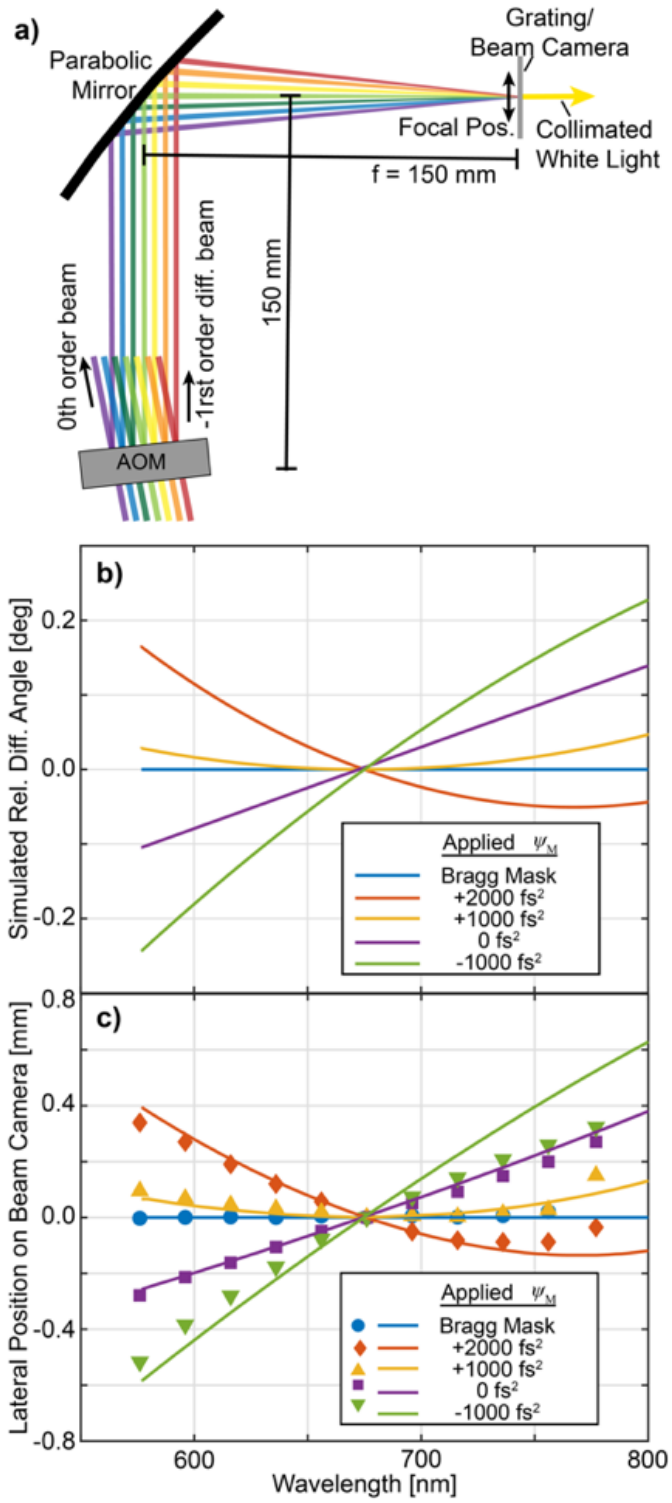

Figure 3.2. a) Schematic of the relative geometry of the 4-f quartz AOM pulse-shaper system used to both b) simulate and c) experimentally measure the variation of the relative diffraction angle with respect to a center wavelength of $\lambda = 675$ nm for various applied ψ_M.

We experimentally characterize the variation of $\boldsymbol{\theta}_{\mathbf{diff}}$ by measuring the spatial position of the outgoing beam from the 4-f pulse-shaper system as a function of wavelength. Here, the

amplitude acoustic waveform $\mathbf{a}(\mathbf{t_A})$ is set to allow diffraction of a narrow (~20 nm) bandwidth of light while a beam-camera placed at the position of the re-collimation grating measures the spatial dispersion of the outgoing light. As illustrated by the data points in Figure 3.2(c), for the Bragg mask all wavelengths of light precisely overlap on the beam camera as they are diffracted at the same angle. Deviation from a Bragg mask leads to spatial variation of the outgoing beam, as shown by the data corresponding to a flat-sinusoidal acoustic waveform, as well as waveforms corresponding to $\boldsymbol{\psi_M}$ in which a GDD of -1000, +1000, and +2000 fs^2 is respectively applied. In addition, from ray-tracing simulations of the focal position combining the relative geometry of the 4-fshaper and the expected angle of diffraction of the AOM from Figure 3.2(b). represented by the solid lines in Figure 3.2(c), we find that the predicted direction and magnitude of the spatial dispersion associated with various $\boldsymbol{\psi_M}$ masks is reproduced by the experimental measurements. Notably, we observe that applying a 2nd order spectral phase mask of $\boldsymbol{\psi_{M,2} = +1000}$ fs^2, nearly removes $\boldsymbol{\theta_{diff}}$ to first order.

Using the same methods used to determine the spectral phase associated with a flat-sinusoidal acoustic wave, we can explicitly calculate the phase contributions associated with the Bragg mask. Making a comparison with Eq. (3.10), a similar expression relating the difference between the instantaneous phase of the Bragg mask and a sinusoid with frequency $\boldsymbol{f_0}$ can be derived and used to express the relative spectral phase associated with the Bragg mask ($\boldsymbol{\psi_B = 2\pi t_A(\omega) \cdot (f_B(\omega) - f_0)}$).

$$\begin{aligned}\mathbf{2\pi t_A}(\boldsymbol{\omega}) \cdot (\boldsymbol{f}_{\mathbf{B}}(\boldsymbol{\omega}) - \boldsymbol{f_0}) \;=\; & \boldsymbol{\psi_{B,0}} + \boldsymbol{\psi_{B,1}}(\boldsymbol{\omega} - \boldsymbol{\omega_0}) + \frac{\boldsymbol{\psi_{B,2}}}{\mathbf{2}}(\boldsymbol{\omega} - \boldsymbol{\omega_0})^{\mathbf{2}} \\ & + \frac{\boldsymbol{\psi_{B,3}}}{\mathbf{6}}(\boldsymbol{\omega} - \boldsymbol{\omega_0})^{\mathbf{3}} + \frac{\boldsymbol{\psi_{B,4}}}{\mathbf{24}}(\boldsymbol{\omega} - \boldsymbol{\omega_0})^{\mathbf{4}}\end{aligned} \tag{3.15}$$

Here, $\frac{d^n \psi_B}{d\omega^n} = \boldsymbol{\psi_{B,n}}$ with $\boldsymbol{\psi_{B,2}}$, $\boldsymbol{\psi_{B,3}}$, and $\boldsymbol{\psi_{B,4}}$ represent the respective GDD, TOD, and FOD dispersion parameters associated with the application of a Bragg mask. As such, if the user-

defined spectral phase mask is chosen such that $\boldsymbol{\psi_{M,n} = \psi_{B,n}}$, all incident wavelengths will be diffracted at precisely the same angle. For the broadband spectrum incident on the quartz AOM presented above, the Bragg mask corresponds to the application of $\boldsymbol{\psi_M}$ with a dispersion corresponding to $\boldsymbol{\psi_{B,2}}$= 940 fs^2, $\boldsymbol{\psi_{B,3}}$ = -1580 fs^3, $\boldsymbol{\psi_{B,4}}$= 8610 fs^4. This matches the previous empirical observation from Figure 3.2(c), in which a phase mask of $\boldsymbol{\psi_M = +1000}$ fs^2 was found to approximately match the diffraction of the Bragg mask to first order.

Unfortunately, the positive sign associated with the effective GDD of the Bragg mask represents a challenge for AOM-based pulse-shaping systems. While the quartz AOM is capable of compensating for the normal dispersion of the AOM itself, in order to produce a constant diffraction angle over a broad spectral range, it is necessary to implement a phase mask which imposes significant additional positive 2nd order, and negative 3rd order spectral phase contributions.

To implement a 4-f AOM-based pulse shaping system in a globally optimized configuration, two conditions must be met. First, the $\boldsymbol{\psi_M}$ applied by the AOM must result in a temporally compressed pulse at the location of the measurement. Second, diffraction of the shaped-light must occur near the Bragg angle of the center wavelength across the entire spectral range of the shaper. In order to simultaneously accomplish these conditions, additional dispersion compensation is necessary. Here, negative GDD and TOD can be added through the addition of optical elements with anomalous dispersion $\boldsymbol{\psi_{AD}}$. With this additional phase compensation, the AOM can operate in a regime in which $\boldsymbol{\psi_M \cong \psi_B}$, allowing for diffraction of the shaped light at a constant angle while the net group delay of the experimental beampath remains near zero, $\boldsymbol{\psi_{Net,1}(\omega) = 0}$, enabling the simultaneous temporal compression of the optical pulse.

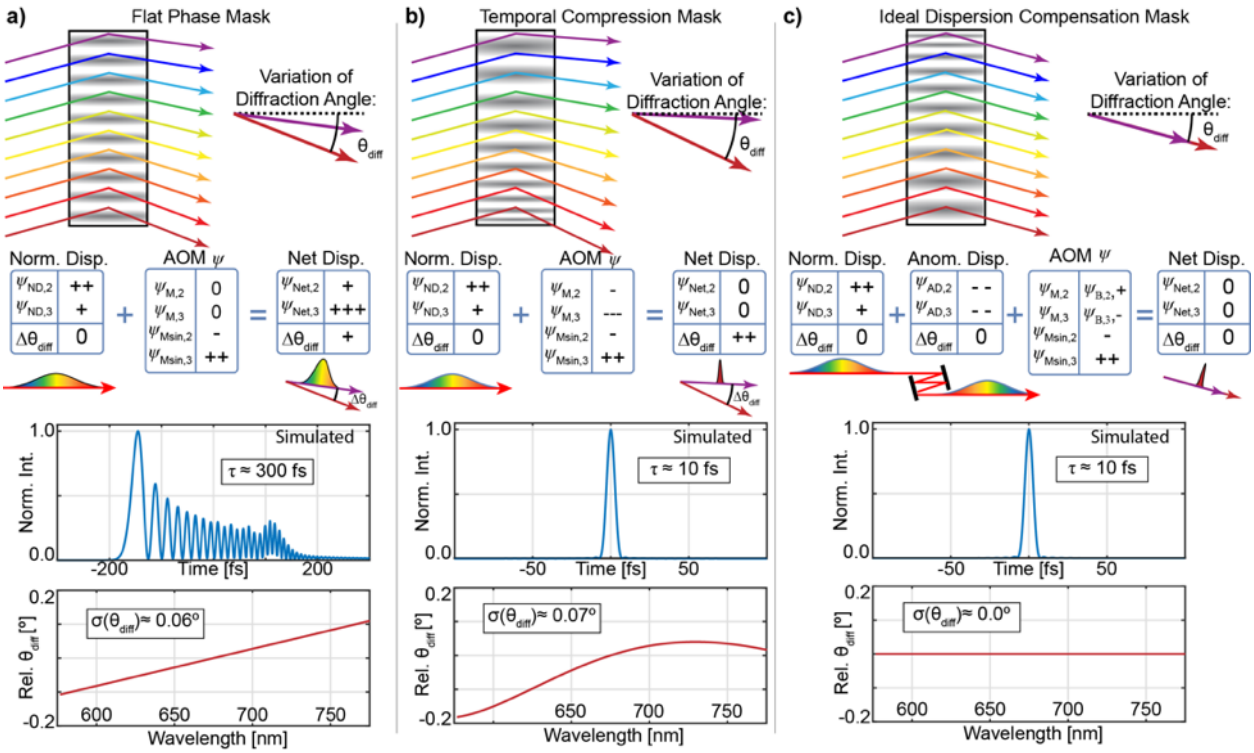

Figure 3.3. Schematics of the incoming and outgoing diffracted light from a quartz-based AOM 4-f pulse-shaping system are represented for configurations representing a) a flat-sinusoidal acoustic mask, b) a temporally compressive acoustic mask, and c) a globally optimized temporally compressive Bragg Mask. The upper schematics pictorially represent the general sign and magnitude of dispersion contributions from normal and anomalous optical elements in the beampath in addition to the ψ_M and ψ_{Msin} spectral phase contributions associated with the AOM. Pictorial representations of the resulting temporal compression and variation of the diffraction angle are further diagrammed. For a temporally compressed input pulse ($\lambda_0 = 675$ nm, $\lambda_{FWHM} = 100$ nm), the bottom panels display the simulated temporal duration and relative variation of the diffraction angle of the outgoing pulse for a beampath including an AOM thickness, $L_{AOM} = 20$ mm, and a YAG crystal, $L_{YAG} = 8$ mm used for white light generation.

These scenarios are explored in Figure 3.3.3, which schematically explores the relationship between the spectral phase applied by the AOM and the relative variation of the diffraction angle for the output beam. Here, for a temporally compressed input pulse centered at $\boldsymbol{\lambda_0 = 675}$ nm with a bandwidth of $\boldsymbol{\lambda_{FWHM} = 100}$ nm, we simulate the resulting temporal dispersion and angular diffraction resulting from a quartz AOM ($\boldsymbol{L_{AOM} = 20}$ mm) for a beampath which includes a YAG crystal used for white-light generation ($\boldsymbol{L_{YAG} = 8}$ mm). Shown in Figure 3.3(a), a flat-sinusoidal acoustic mask results in both a temporal stretching of the optical pulse with a large contribution from third-order spectral phase in addition to a linear variation of the diffraction angle. Figure

3.3(b), displays the effects of an AOM mask which provides precise spectral phase compensation to temporally compress the pulse to its Fourier limit. Unfortunately, using $\boldsymbol{\psi_M}$ to fully compensate for residual spectral phase results in a larger relative variation of the diffraction angle. Lastly, Figure 3.3(c) represents the case in which anomalous dispersion has been added in a manner such that the AOM can apply an acoustic waveform near the Bragg mask, enabling both temporal compression and diffraction at a constant angle.

The temporal effect of the application of $\boldsymbol{\psi_M}$ equivalent to the Bragg waveform can be experimentally characterized by measuring the duration of the optical pulse following the pulse-shaping system. Using a broadband white-light (WL) supercontinuum spectrum generated via filamentation in a 8mm YAG crystal [18], we send a WL pulse through the AOM-based pulse-shaper and investigate the effect of varied $\boldsymbol{\psi_M}$ on the net spectral phase of the outgoing pulse using polarization-gated frequency resolved optical gating (PG-FROG) [24]. The 30-fs output of a NOPA operating at $\boldsymbol{\lambda = 550}$ nm was used as the optical gate.

As discussed above, application of a sinusoidal mask has the net effect of applying a negative GVD which approximately cancels out the normal dispersion of the AOM but also adds a strong positively signed TOD. This results in a strong curvature of the PG-FROG trace as seen in Figure 3.4(a). Applying an acoustic waveform corresponding to the Bragg mask, Figure 3.4(b) displays the resulting PG-FROG trace which, with respect to Figure 3.4(a), now exhibits a strong, positive, linear chirp corresponding to the additional positive GVD associated with $\boldsymbol{\psi_B}$.

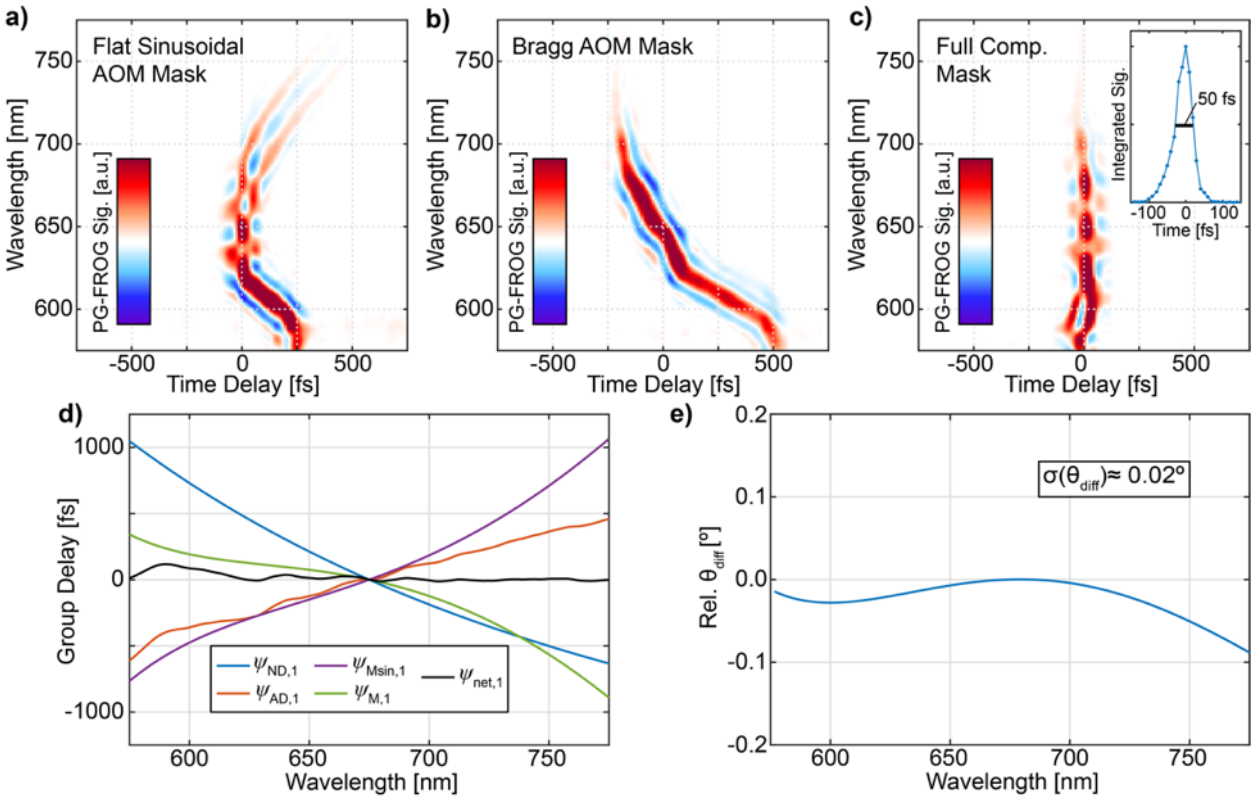

Figure 3.4. PG-FROG measurements of the temporal duration of the optical pulse at the sample location corresponding to differing ψ_M applied by the AOM in the 4-f pulse-shaping system. a) displays the PG-FROG recorded using a flat sinusoidal mask and exhibits curvature indicative of a strong residual cubic phase. The application of a Bragg phase mask ($\psi_M = \psi_B$) in panel b) results in the linear chirping of the optical pulse. By compensating for higher order spectral phase contributions in panel c), the AOM pulse-shaper is capable of compressing the pulse to pulse durations of 50 fs. The group delay corresponding to each of the dispersive contributions from Table 3.1 used to achieve this temporal compression is shown in d) resulting in a flat-spectral phase (black line). e) displays the calculated angle of diffraction relative to the center wavelength corresponding to the ψ_M in Table 3.1. representing the acoustic-mask used to temporally compresses the optical pulse while matching the Bragg Mask to first order.

In order to fully compress the optical pulse while minimizing the variation of the angle of diffraction to first order, we implement anomalous dispersion compensation in the form of a chirped-mirror compressor system prior to the pulse-shaper. By implementing 24 bounces (-40 fs^2/bounce) we add an additional -1280 fs^2 of GVD to the beampath, which allows the shaper system to operate with a GVD contribution identical to the Bragg Mask resulting in a compression of the pulse below 50 fs (Figure 3.4(c)) limited primarily by the temporal duration of the NOPA generated gate pulse used for characterizing the spectral phase. Future implementation of a

shorter-gate pulse for the PG-FROG measurement should allow for more precise measurement and compensation of the spectral phase to enable compression of the pulse to duration closer to the ~10 fs time-bandwidth limit.

Table 3.1. Spectral phase parameters (λ_0 =675 nm) associated with quartz-based AOM-based 2DWL system. ψ_{ND} is determined by the optical thickness of the AOM $L_{AOM} = 20$ mm and other transmissive optical elements in the pump beampath ($L_{YAG} = 8$ mm). ψ_{AD} is generated via ~24 bounces on a negative chirped mirror compressor system. ψ_M and $\psi_{M\sin}$ represent the user defined and static sinusoidal spectral phase contributions associated with the application of the AOM phase mask. ψ_{Net} is the net dispersion of the complete 2DWL microscopy system while the difference of $\psi_M - (\psi_B)$ shows the difference in between spectral phase necessary to temporally compress the pulse and the spectral phase profile associated with the Bragg waveform.

Phase Term	GDD (fs^2)	TOD (fs^3)	FOD (fs^4)
$\boldsymbol{\psi_{ND}}$	**950+(980)**	**490+(450)**	**-40+(15)**
$\boldsymbol{\psi_{AD}}$	**-1280**	**0**	**0**
$\boldsymbol{\psi_M}$	**930**	**-5330**	**+27125**
$\boldsymbol{\psi_{M\sin}}$	**-1580**	**4390**	**-27100**
$\boldsymbol{\psi_{Net}}$	**0**	**0**	**0**
$\boldsymbol{\psi_M - \psi_B}$	**950-(940) = 10**	**-5330-(-1580) =-3750**	**27125-(8610) = 18515**

Table 3.1 displays each of the spectral phase terms corresponding to the dispersive elements within the experimental beampath for the configuration described above. In order to fully compress the pulse, $\boldsymbol{\psi_M}$ is chosen such that the net group-delay of the system is zero. While $\boldsymbol{\psi_M} \cong \boldsymbol{\psi_B}$ for the GDD contribution, significant differences still exist between the spectral phase mask necessary for temporal compression and Bragg mask for the higher order TOD and FOD terms (Table 3.1: $\boldsymbol{\psi_M - \psi_B}$). Future improvements to $\boldsymbol{\psi_{AD}}$, which may be implemented by moving towards a dispersion pre-compensation system capable of providing additional control over TOD and FOD parameters, will enable this system to more closely match the globally optimized configuration in which $\boldsymbol{\psi_M} \cong \boldsymbol{\psi_B}$ at higher orders. Still, as demonstrated by Figure 3.4(c) which displays the PG-FROG corresponding to the fully compressed pulse, simply providing proper GDD pre-compensation was able to reduce relative variation of the diffraction angle by a factor of three (as compared to Figure 3.3(b)). Further simulation of the variation of the diffraction angle corresponding to the generation of the pulse-pairs necessary for 2DES measurements for time-

separations out to 100 fs showed the generation of pulse-pairs with short time separation had a negligible effect on the diffraction angle with respect to the $\boldsymbol{\psi_M}$ necessary for temporal compression of the pulse.

3.5 Conclusions

AOM-based pulse shaping is a method that can shape ultrafast broad bandwidth pulses so that they have both minimal spatial and temporal dispersion. This capability is possible when the spectral phase of the user applied mask, ψ_M, is both equal to the spectral phase of a Bragg mask, ψ_B, where each frequency is diffracted at the same angle, and when ψ_M is equal to the sum of all the other contributions to the spectral phase in the beampath. This includes a contribution to the spectral phase from a static sinusoidal wave across the AOM. We demonstrate that it is possible to calculate these contributions to spectral phase when the optical constants of the AOM crystal and additional optical components are known, as well as the calibration parameters that map the pulse wavelength/frequency to the relative timing of the transducer output, $\mathrm{t_A}$. Lastly, we show that the simulated spatial and temporal dispersion due to the application of AOM masks with various values of GDD maps closely to the experimentally measured spatial and temporal dispersion due to the same AOM masks, and that there exists a user applied spectral phase that will yield a pulse with minimal spatial and temporal dispersion.

3.6 References

1. F. D. Fuller and J. P. Ogilvie, "Experimental Implementations of Two-Dimensional Fourier Transform Electronic Spectroscopy," Annu. Rev. Phys. Chem. **66**(1), 667–690 (2015).
2. C. L. Smallwood and S. T. Cundiff, "Multidimensional Coherent Spectroscopy of Semiconductors," Laser Photonics Rev. **12**(12), 1800171 (2018).
3. K. J. Karki, J. R. Widom, J. Seibt, I. Moody, M. C. Lonergan, T. Pullerits, and A. H. Marcus, "Coherent two-dimensional photocurrent spectroscopy in a PbS quantum dot photocell," Nat Commun. **5**(1), 1–7 (2014).
4. F. Thouin, D. A. Valverde-Chávez, C. Quarti, D. Cortecchia, I. Bargigia, D. Beljonne, A. Petrozza, C. Silva, and A. R. S. Kandada, "Phonon coherences reveal the polaronic character of excitons in two-dimensional lead halide perovskites," Nat. Mater. **18**(4), 349–356 (2019).
5. D. M. Jonas, "Two-Dimensional Femtosecond Spectroscopy," Annu. Rev. Phys. Chem. **54**(1), 425–463 (2003).
6. M. Khalil, N. Demirdöven, and A. Tokmakoff, "Coherent 2D IR Spectroscopy: Molecular Structure and Dynamics in Solution," J. Phys. Chem. A **107**(27), 5258–5279 (2003).
7. D. Brida, C. Manzoni, and G. Cerullo, "Phase-locked pulses for two-dimensional spectroscopy by a birefringent delay line," Opt. Lett. **37**(15), 3027–3029 (2012).
8. S.-H. Shim and M. T. Zanni, "How to turn your pump–probe instrument into a multidimensional spectrometer: 2D IR and Vis spectroscopiesvia pulse shaping," Phys. Chem. Chem. Phys. **11**(5), 748–761 (2009).
9. S. C. Edington, A. Gonzalez, T. R. Middendorf, D. B. Halling, R. W. Aldrich, and C. R. Baiz, "Coordination to lanthanide ions distorts binding site conformation in calmodulin," PNAS **115**(14), E3126–E3134 (2018).
10. B. Xiang, R. F. Ribeiro, A. D. Dunkelberger, J. Wang, Y. Li, B. S. Simpkins, J. C. Owrutsky, J. Yuen-Zhou, and W. Xiong, "Two-dimensional infrared spectroscopy of vibrational polaritons," PNAS **115**(19), 4845–4850 (2018).
11. A. M. Weiner, "Ultrafast optical pulse shaping: A tutorial review," Opt. Commun. **284**(15), 3669–3692 (2011).
12. J. A. Myers, K. L. M. Lewis, P. F. Tekavec, and J. P. Ogilvie, "Two-color two-dimensional Fourier transform electronic spectroscopy with a pulse-shaper," Opt. Express **16**(22), 17420–17428 (2008).
13. N. M. Kearns, R. D. Mehlenbacher, A. C. Jones, and M. T. Zanni, "Broadband 2D electronic spectrometer using white light and pulse shaping: noise and signal evaluation at 1 and 100 kHz," Opt. Express **25**(7), 7869–7883 (2017).
14. J. M. Nite, J. D. Cyran, and A. T. Krummel, "Active Bragg angle compensation for shaping ultrafast mid-infrared pulses," Opt. Express **20**(21), 23912–23920 (2012).
15. P. M. Donaldson, G. M. Greetham, D. J. Shaw, A. W. Parker, and M. Towrie, "A 100 kHz Pulse Shaping 2D-IR Spectrometer Based on Dual Yb:KGW Amplifiers," J. Phys. Chem. A **122**(3), 780–787 (2018).
16. A. C. Jones, N. M. Kearns, J.-J. Ho, J. T. Flach, and M. T. Zanni, "Imaging the structure and energetics of singlet fission microcrystals with 2D White Light (2DWL) microscopy.," Nat. Chem. **In press**, (2019).
17. N. Krebs, I. Pugliesi, J. Hauer, and E. Riedle, "Two-dimensional Fourier transform spectroscopy in the ultraviolet with sub-20 fs pump pulses and 250–720 nm supercontinuum probe," New J. Phys. **15**(8), 085016 (2013).

18. M. Bradler, P. Baum, and E. Riedle, "Femtosecond continuum generation in bulk laser host materials with sub-μJ pump pulses," Appl. Phys. B **97**(3), 561 (2009).
19. R. D. Mehlenbacher, M.-Y. Wu, M. Grechko, J. E. Laaser, M. S. Arnold, and M. T. Zanni, "Photoexcitation Dynamics of Coupled Semiconducting Carbon Nanotube Thin Films," Nano Lett. **13**(4), 1495–1501 (2013).
20. A. C. Jones, N. M. Kearns, M. Bohlmann Kunz, J. T. Flach, and M. T. Zanni, "Multidimensional spectroscopy on the microscale: Development of a multimodal imaging system incorporating 2D White-Light spectroscopy, broadband transient absorption, and atomic force microscopy.," (Submitted), (2019).
21. M. A. Dugan, J. X. Tull, and W. S. Warren, "High-resolution acousto-optic shaping of unamplified and amplified femtosecond laser pulses," J. Opt. Soc. Am. B **14**(9), 2348–2358 (1997).
22. C. W. Hillegas, J. X. Tull, D. Goswami, D. Strickland, and W. S. Warren, "Femtosecond laser pulse shaping by use of microsecond radio-frequency pulses," Opt. Lett. **19**(10), 737 (1994).
23. E. Li, J. Yao, D. Yu, J. Xi, and J. Chicharo, "Optical phase shifting with acousto-optic devices," Opt. Lett. **30**(2), 189–191 (2005).
24. R. Trebino, K. W. DeLong, D. N. Fittinghoff, J. N. Sweetser, M. A. Krumbügel, B. A. Richman, and D. J. Kane, "Measuring ultrashort laser pulses in the time-frequency domain using frequency-resolved optical gating," Rev. Sci. Instrum. **68**(9), 3277–3295 (1997).

4. 2D White-Light Spectroscopy: Application to Lead-Halide Perovskites with Mixed Cations

Lead-halide perovskite photovoltaic devices continue to increase in efficiency. One route to improved performance is the inclusion of cations and halides of mixed composition. Here, we report ultrafast 2D White-Light (2D WL) spectra of mixed lead-halide perovskite films using combinations of the organic-cations methylammonium, formamidinium, and Br^-/Cs^+. Linear absorption spectra of all the samples are smooth and vary only in the position of their bandgaps, but they have different 2D WL spectra. The microcrystalline films containing purely iodide and organic cations exhibit a feature approximately 150 meV above the bandgap of the material that we assign to a previously unreported electronic transition. The Br^-/Cs^+ film lacks this feature. All of the samples exhibited similar kinetics, which we attribute to hot-carrier cooling rates on the 100s of fs time-scale. The differences in 2D WL spectra reported here suggest that the Br^-/Cs^+ is altering the electronic structure of the films to impact efficiency, helping to explain why the bandgap alone is insufficient to explain perovskite solar cell efficiencies.

Acknowledgments

The samples for this project were made by Jessica T. Flach at École polytechnique fédérale de Lausanne under the guidance of Hui-Seon Kim in the lab of Anders Hageldt. Reprinted with permission from *Emerging Trends in Chemical Applications of Lasers*, Chapter 7, pp 135-151.

4.1 Introduction

Two-dimensional electronic (2D ES) spectroscopy is an ultrafast spectroscopic method that utilizes multiple laser pulses to correlate electronic states. 2D White-Light (2D WL) spectroscopy

is a version in which ultrabroadband pulses are utilized, typically through continuum generation.[1] To create the necessary pump pulse delays and phases, pulse shapers have been built and optimized for the large pulse bandwidth and can operate at 100 kHz or larger repetition rates, making them compatible with new ytterbium laser technology.[2] Broad bandwidth is typically necessary to span the entirety of an electronic transition in a molecule and is particularly helpful for materials systems where electronic transitions are very broad or nearly continuous, as is the case with perovskites. As shown below, the 2D WL spectra map energy transfer between electronic states via the observation of cross peaks and 2D lineshapes. A particular strength of 2D spectroscopy is the ability to measure states which have no oscillator strength, called optically dark states, which prevents them from being measured through linear spectroscopy. 2D WL has femtosecond time resolution and so can measure energy and charge transfer with high fidelity. For more details on the description of the theory and implementations of two-dimensional spectroscopies, the authors suggest several review articles 3-5[3–5] and prior applications of 2D ES to light harvesting proteins in photosynthetic systems,[6–8] the electronic structure and energy transfer in semiconductors.[1,9,10] This chapter contains a report on the application of 2D WL spectroscopy to mixed-cation perovskites.

Organic-inorganic lead halide perovskites have received great attention in the past decade as a promising new photovoltaic (PV) material.[11] Perovskites are lauded for their strong absorption coefficients in the visible range,[12,13] low exciton binding energies,[13–15] and high balanced charge carrier diffusion lengths[16–18] with ambipolar charge transfer. In the years since the first perovskite PV device was made in 2009 with an initial efficiency of just over 3%,[19] the efficiencies have rapidly increased now reaching 25.5%.[20] Perovskites have the general ABX_3 structure, where the A site can be organic cations methylammonium (MA), formamidinium (FA), or inorganic cations

such as cesium. The B site is typically lead or tin and the halide site, X, can be occupied by iodide, bromide, or chloride. While $MAPbI_3$ has been the most studied perovskite composition to date, currently the highest performing perovskite photovoltaic devices are those with both mixed cation and mixed halide compositions.[21] The halides have a large effect on the valence band level, which allows the bandgap to be tuned relative to the solar spectrum and for optimizing tandem solar cells.[11] Although bromide unfavorably blue-shifts the bandgap, it helps stabilize the black phase of FA-containing perovskite compositions, leading to longer-lived devices.[21] Incorporating FA into the lattice improves the thermal and humidity stability of $MAPbI_3$ while also favorably red-shifting the absorption onset.[22,23] Although organic cations have a much smaller effect on the bandgap, the FA cation is larger in size than the MA cation, which not only indirectly determines the bandgap by increasing the lattice symmetry[24] but also affects the crystal structure and lattice parameters of lead halide perovskites.[25] Black-phase $FAPbI_3$ generally crystallizes in a cubic structure while $MAPbI_3$ forms a tetragonal structure at room temperature.[26] Besides stability, the crystal structure impacts the rate of hot-carrier cooling, 270 fs versus 210 fs for $FAPbBr_3$ and $MAPbBr_3$ respectively, and the mobility of charges.[27] In this paper, we investigate the effects of organic cation stoichiometry MA^+:FA^+ and the presence of Cs^+ as well as the effects of the mixed halide, Br^- and I^-, on the sub-picosecond kinetics and electronic structure of mixed lead halide perovskites.

An interesting property of lead halide perovskites that is intimately linked to their efficiency are the ultrafast kinetics of exciton dissociation and the accompanying cooling of the electrons and holes in the lattice. As a result, ultrafast spectroscopy is often used to study the initial excitation and sub-picosecond dynamics of perovskites.[1,28–30] In the case of $MAPbI_3$,[27,29,31–33] it has been shown that free charges are generated upon photoexcitation because the small binding

energy allows excitons to dissociate into free electrons and holes within 50 fs.[13,34–36] For our work, the most relevant studies are on bandgap normalization and hot-carrier cooling. The presence of free-charges leads to a renormalization of the bandgap,[33] whereby the free-charges coulombically shield the ions in the lattice, shifting the valence and conduction band edges. This renormalization occurs simultaneously with the creation of free carriers.[37] The small exciton binding energy, and relatively high charge mobility give insight into why perovskite photovoltaic devices are efficient, but it is not clear if these same properties are also able to differentiate why certain perovskite devices are more efficient than others.

In this chapter I use an ultrafast technique that we call two-dimensional white light (2D WL) spectroscopy to study the photophysics of mixed-organic-cation lead iodide perovskite mixtures. Unlike traditional transient absorption spectroscopy, where the photophysics are monitored after initiating at a specific frequency, 2D WL spectroscopy uses femtosecond pump pulses created by continuum generation that have femtosecond time resolution and a broad spectrum.[2] The 2D spectra resolve the pump wavelengths, so that the entire absorption band is simultaneously excited by the pump and is resolved in a single spectrum, analogous to measuring many transient absorption spectra with different center pump frequencies. Additionally, the spectra reveal cross peaks that give information about energy transfer pathways and electronic or vibrational couplings within a system. Another difference that is relevant to the interpretation of the data presented below, is that two-dimensional spectroscopies typically have narrower and better-defined spectra because the signals scale to the 4^{th} power of transition dipole, μ^4, rather than the square, μ^2, for linear spectroscopies.[38] The continuous coverage over a broad wavelength range made possible by white-light excitation is particularly advantageous for studying the electronic structure of next-generation materials that absorb across a large fraction of the solar spectrum.

Here, we utilize 2D WL spectroscopy to continuously span 200 nm of these perovskite films, centered to cover about 100 nm on either side of the bandgap, thereby resolving the eigenstates into which relaxation is expected to occur.

4.2 Results

Four different ABX_3 lead-halide perovskite semi-crystalline thin films were prepared as described in Methods, with different ratios of the organic cation, A, and iodide as the halide, X, were measured with two-dimensional white light (2D WL) spectroscopy. The samples were $MAPbI_3$, $MA_{0.75}FA_{0.25}PbI_3$, $MA_{0.5}FA_{0.5}PbI_3$, and $MA_{0.16}FA_{0.79}Cs_{0.05}PbI_{2.43}Br_{0.57}$, which we label as samples 1-4, respectively. Sample 4, which contains a small amount of cesium and bromide is a composition often used for highly efficient perovskite photovoltaic devices.[39] Samples 1-3 were chosen to study the effect of organic cation ratio on the different spectroscopic observables. Sample 4 was chosen as an example of a high performing perovskite for comparison. The linear absorption spectra of the four samples are shown in Figure 1. The bandgaps for the four samples were calculated from the absorption spectra using the Tauc method, which gives 783 nm (1.58 eV), 788 nm (1.57 eV), 800 nm (1.54 eV), and 735 nm (1.69 eV) for samples 1-4 respectively. These values match well with previously reported bandgaps for samples of the same composition.[40] The halide composition has the largest effect on the bandgap of perovskites,[41] especially by governing the antibonding overlapping of Pb s and X p orbitals, and the cation concentration and presence of cesium also shift the bandgap.[25]

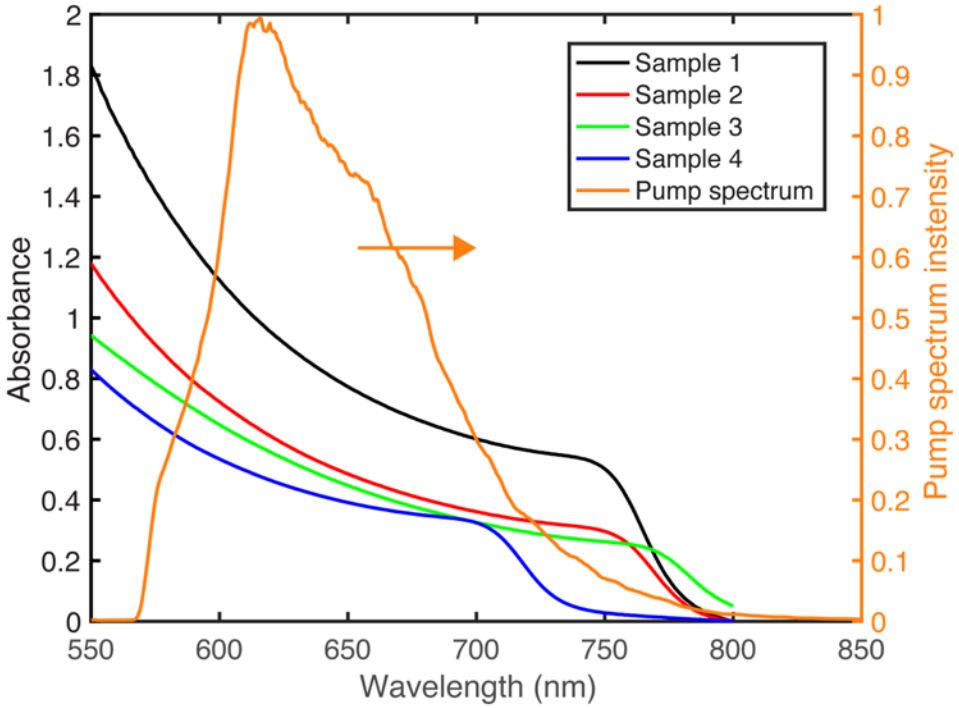

Figure 4.1. Linear absorption spectra of the four perovskite samples, $MAPbI_3$, $MA_{0.75}FA_{0.25}PbI_3$, $MA_{0.5}FA_{0.5}PbI_3$, and $MA_{0.16}FA_{0.79}Cs_{0.05}PbI_{2.43}Br_{0.57}$, in black, red, green, and blue respectively. The spectrum of the pump pulse used in the 2D experiments is also plotted in orange and spans the band gap of all four samples.

4.2.1 2D WL Spectroscopy Spanning the Band-Edge

For our 2D WL measurements, the pulses are <40 fs in duration and span ~200 nm, as shown by the spectrum of the pump-pulse in Figure 4.1 (orange). The bandwidth of the probe pulse (not shown) is even larger. Shown in Figure 4.2a is a 2D WL spectrum of $MAPbI_3$ (sample 1) at a "waiting time" (analogous to a pump-probe delay in a kinetic scan) of $t_2 = 0$ fs. We note that the observed features decay gradually with time delay and that the same features at $t_2 = 0$ fs are also seen at $t_2 = 25$ fs (not shown). From these observations we conclude that non-resonant artifacts and the residual chirp of the pulses have negligible effects on the spectra.The main feature that dominates the 2D spectrum is a ground state bleach (GSB), (Figure 4.2, peak A). This feature for $MAPbI_3$ matches previously published 2D electronic spectra.[10] Peak A is a cross peak due to pumping above the bandgap and probing at the bandgap. It extends vertically towards a diagonal

peak at 750 nm (Figure 4.2 peak B). There is a second ground state bleach feature that appears ~60-80 meV above the band edge (peak C) and similarly extends to the diagonal (peak D). To better illustrate the diagonal features, we plot in Figure 4.3e cuts through the 2D spectra along the diagonal for all four samples, where peak D appears at 720 nm (~1.65 eV) and peak B is at 750 nm for sample 1. I discuss peak E below.

2D WL spectra are also shown in Figure 4.2b-d for the other 3 samples. They have similar features, but differ in their relative intensities and frequencies. The major difference is that sample 4, the Cs^+ compound, lacks peak D.

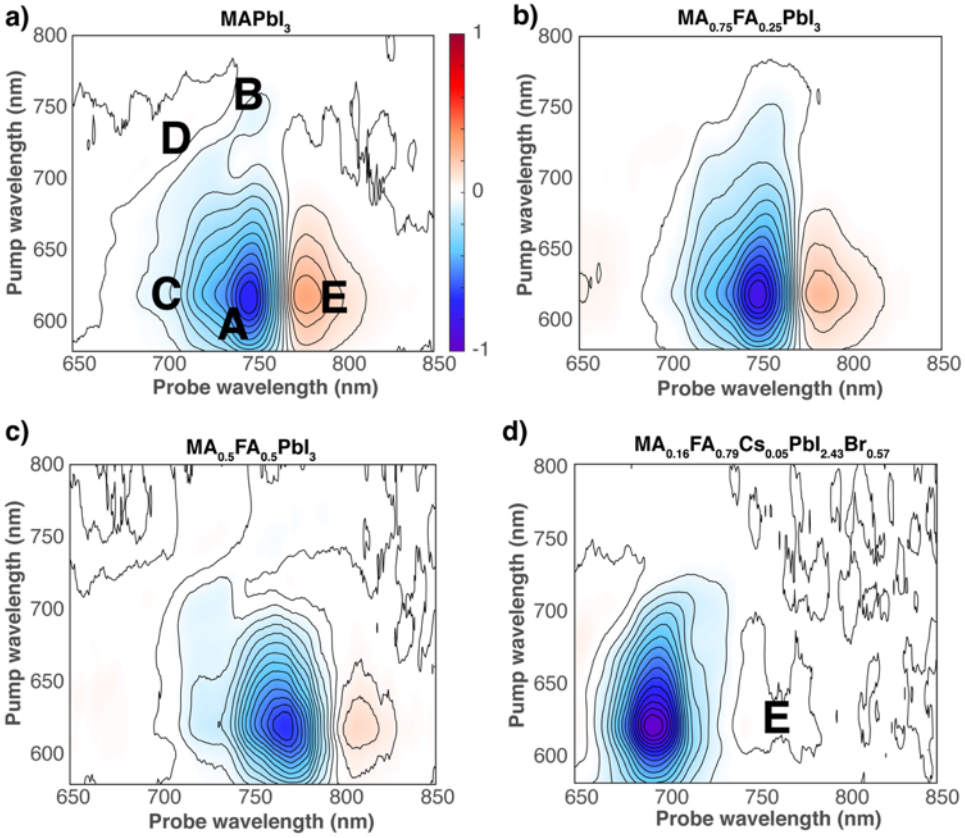

Figure 4.2. 2D WL spectra at t_2 = 0 fs for a) $MAPbI_3$, b) $MA_{0.75}FA_{0.25}PbI_3$, c) $MA_{0.5}FA_{0.5}PbI_3$, and d) $MA_{0.16}FA_{0.79}Cs_{0.05}PbI_{2.43}Br_{0.57}$, samples 1-4, respectively.

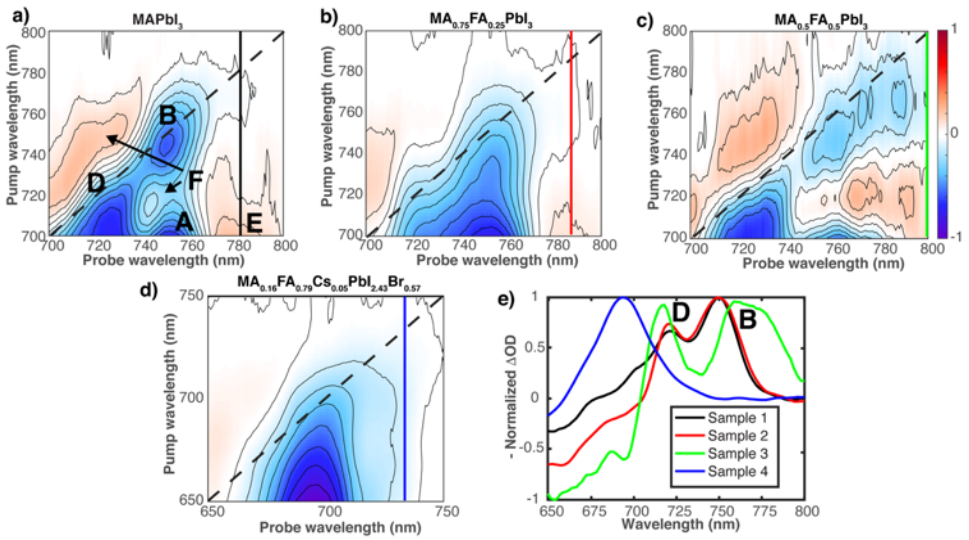

Figure 4.3. a-d) 2D WL spectra of samples 1-4, respectively, at 0 fs waiting time. The spectra zoom in on the diagonal peaks near the bandgap. Solid vertical lines of black, red, green, and blue correspond to the bandgap of each sample. e) Overlay of the diagonal slices, where the black, red, green, and blue traces correspond to samples 1-4 respectively.

Figure 4.3a-d plots the same 2D WL spectra from Figure 4.2, but zooms in on the diagonal peaks D and B. Each figure includes a solid vertical line that marks the bandgap for that particular sample. Figure 3e plots diagonal slices through the 2D WL spectra to better illustrate peaks B and D. Peak B is prominent in samples 1-3 and starts at its respective bandgap. Peak D occurs at about the same frequency in samples 1-3, at 720 nm. There are also cross peaks between peaks B and D, which we label F in Figure 4.3a. The cross peaks indicate that peaks B and D share a common ground state. Sample 4, the perovskite containing cesium, has a very different spectrum. It has a single peak, which we label B since it lies at the same wavelength as cross-peak A. Thus 2D WL spectra show the absorption of light anywhere above the energy of the bandgap will create a bleach at the bandgap of the sample revealing that there are two distinct electronic transitions near the bandgap.

4.2.2 Kinetics and Multiphoton Experiments

Shown in Figure 4.4 are 2D WL spectra of sample 1 collected at larger waiting time delays. The GSB peak A remains the dominant feature at all waiting times.

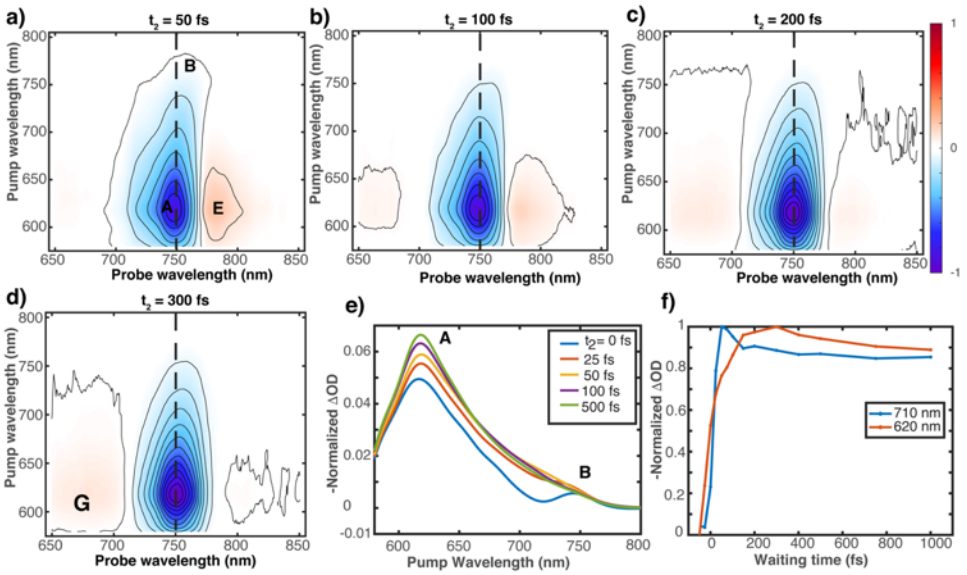

Figure 4.4. a-d) $MAPbI_3$ 2D WL spectra at four waiting times, illustrating the decay of the bandgap renormalization peak at λ_{probe} = 800 nm, and the growth of peak G. e) plots slices through the 2D WL spectra at λ_{probe} = 750 nm (dashed vertical lines), illustrating the fast growth of the GSB close to the bandgap, and the slightly slower growth of the GSB at 620 nm, where f) shows the kinetics at two representative pump wavelengths, 710 nm (blue) and 620 nm (orange).

To better illustrate the dynamics associated with peaks A and B, shown in Figure 4.4e are vertical slices through the 2D WL spectra of $MAPbI_3$ at a probe wavelength of 750 nm (dashed line). They show how energy relaxes following photoexcitation. Peak A grows in on a ~300 fs timescale. The intensity of peak B is largely unchanged and is no longer resolved by t_2 = 50 fs because of overlap with peak A. The kinetics of sample 1 are qualitatively representative of all four samples, with insignificant differences in exact rates as discussed below.

In addition, the two photo-induced absorption features, peaks E and G, are present in Figure 4a-d. Peak E, decays over the first 300 fs. Peak G appears at about 100 fs. Peak E has previously been attributed to bandgap renormalization, which also agrees with our data as explained in the Discussion below. Peak G has been attributed to photoinduced reflectivity changes[33] and will not be discussed in this paper.

Looking closer at peak E for all four samples (Figure 4.5a) shows that the decay of the bandgap renormalization occurs within the first picosecond. By fitting the peak E kinetics for all

four samples to a mono-exponential, we determine no significant difference in the time constants, as reported in Table 1. Also in Figure 4.5 are shown the kinetics of peaks B and D for the four samples. Within the pump-probe overlap, the two peaks reach their maximum value, and in the following 100 fs reach a steady value which does not noticeably change over the rest of the waiting times measured. Peak D switches sign only for sample 3 because probing at 720 nm at later waiting times corresponds to excited state absorption of peak G for sample 3. This difference between samples 1,2 and sample 3 is due to 720 nm being higher above the bandgap for sample 3 than for samples 1 and 2. After the initial spike and decay of peaks B and D, it is no longer possible to distinguish between two different peaks, but rather peak B appears broadened.

Thus, in summary of the kinetics, we observe significant changes in peak intensity over the first 500 fs of our experiments. Features closest to the bandgap undergo sub-150 fs dynamics, while features farther away in energy from the bandgap undergo slower dynamics, although still sub-picosecond.

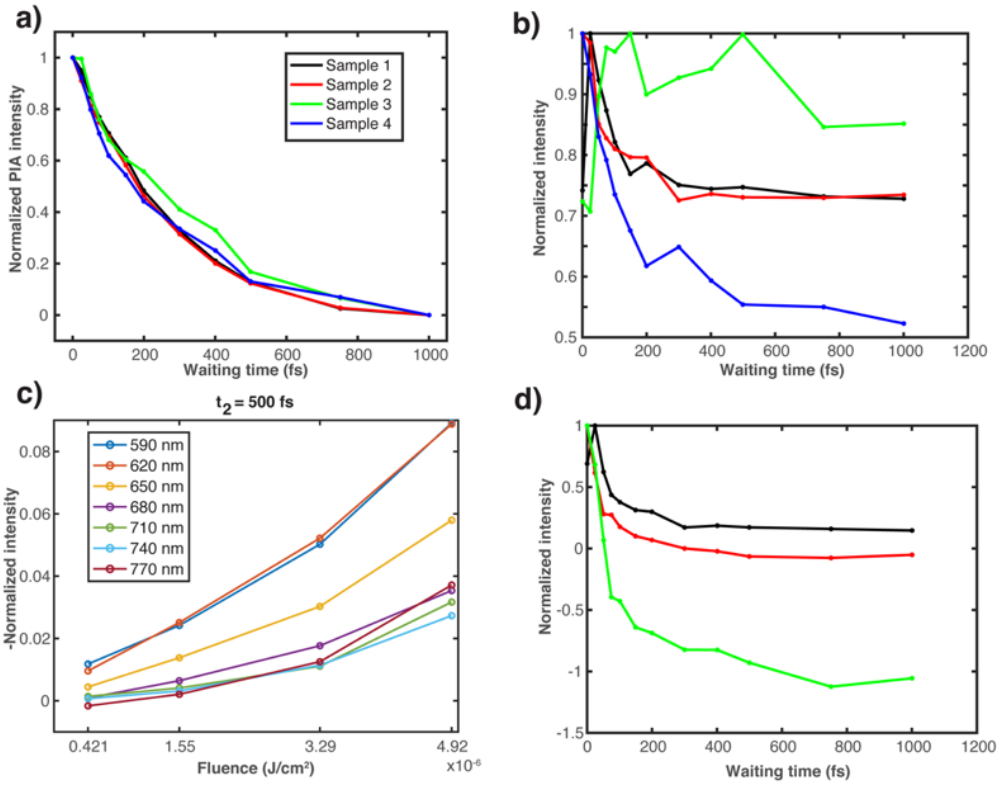

Figure 4.5. a) shows the decay of peak E of samples 1-4 as the black, red, green, and blue traces respectively. c) Fluence-dependent measurements of $MAPbI_3$ at t_2 =500 fs show that the fluence dependence of the GSB at all pump wavelengths is quadratic and becomes more non-linear at wavelengths closest to the bandgap. The non-linearity is due to multi-photon effects, in particular carrier-carrier scattering. b, d) show the kinetics of peaks B and D respectively in samples 1-4. Both features are at their maximum intensity within the width of the pulse overlap (first 50 fs). Sample 4 is not plotted in d), as there is no corresponding peak D in sample 4.

Fluence dependent measurements were performed on the $MAPbI_3$ film (sample 1) to determine if multi-photon effects contributed to the data. Fluence dependent information was only collected for sample 1, to serve as a model for the other samples, given they all show the features of interest, particularly peak A. In Figure 4.5c, the fluence dependence of the 2D intensity at peak A as a function of wavelength is plotted for t_2 = 500 fs. The intensities are not linearly dependent on the fluence, meaning that a portion of these features are created by multi-photon processes. In addition, it is evident from Figure 4.5 that features closer to the bandgap are more quadratic. While multiexciton process contribute close to the bandgap, we also note that the maximum fluence used in these measurements is still below the threshold needed to observe the hot-phonon bottleneck,[31]

which would slow the rate of hot-carrier cooling relative to carrier-concentration at high enough densities.

4. 3 Discussion

4.3.1 Explanation of Bandgap Features B and D

The 2D WL spectra have resolved two electronic transitions that are not apparent in the broad continuum of the absorption spectrum. 2D spectroscopies often have narrower and better-defined spectra than the corresponding linear absorption spectra when there is a continuum of states that overlaps a few discrete states. The signal strength of linear absorption and 2D spectra both scale linearly with concentration, but the 2D spectrum scales as the square of the absorption coefficient.[38] Thus, a single strong transition will appear much more prominently than a high density of weakly absorbing continuum states. An example are quantum dots, in which the S-transition at the bandgap is much better resolved from the continuum of higher energy states in a 2D than a linear absorption spectrum.[42] Thus, we conclude that peaks B and D are discrete and strong electronic transitions that fall near the bandgap. They have linewidths of about 30 nm, consistent with well-defined electronic transitions. Pumping above these states creates cross peaks C and A, which correlate to B and D, respectively. The intensity of peaks C (not shown) and A, increase on a 500 fs timescale, indicating that the deposited energy relaxes into the bandgap states B and D.

There are several possible origins for peaks B and D. Two bands could be explained by two discrete electronic states each created by a distinct structure within the film. As stated in the introduction, $MAPbI_3$ occupies a tetrahedral structure at room temperature, but undergoes a phase change to cubic at only 327 K.[26,43] The two electronic states could be due to the tetrahedral and cubic structures. Temperature dependent XRD measurements of $MAPbI_3$ pin-pointed the

temperature of this phase-change.[43] However, a rough lattice-heating calculation suggests that the sample temperature should only increase by 10-20 K, making the final temperature 308-318 K, making this mechanism unlikely. Another possibility is that peak D is due to an excited vibrational state. 720 nm (1.72 eV) is approximately 1100 cm^{-1} above the bandgap of $MAPbI_3$ calculated from the absorption spectrum. This energy difference corresponds to the C-N stretch and the CH_3-NH_3^+ rocking modes of methylammonium.[44] If a vibrational excited state were the cause of peak D, it might be possible to see coherent oscillations of the cross-peak between D and B (peak F). The waiting times in this experiment were not sufficient to measure the coherent oscillation if it is present. A third possibility is that the two peaks could be due to Rashba splitting. Rashba splitting is a result of spin-orbit coupling, and creates two different conduction bands at the same energy, but with different spins and therefore different momentum.[45] As a result, the lowest energy transition, which would be the bandgap calculated above, would be indirect and a triplet.[46,47] The direct singlet transition, which is at the crossing of the two conduction bands, would be ~50 meV greater in energy than the indirect bandgap. Although the direct transition is optically dark in single crystals,[47] the increased disorder in the perovskite films could result in brightening of the direct transition. The difference between peaks B and D is 60 meV. This could also explain the fast decay of peak D. If peak D is due to the direct bandgap at the crossing of the two conduction bands, it has two possible pathways to relax to the lower energy indirect bandgap.

Between the four samples, the two diagonal peaks were only present for samples 1-3. This suggests that the electronic energy landscape for these two groups, samples 1-3 and sample 4, is significantly different. The electronic structure is intimately connected to device efficiency and so one could expect that having two versus one absorption feature would have a large impact on the efficiency of PV devices. From our experiments, it is not clear whether it is the addition of a third,

inorganic cation or the addition of bromide that leads to this significant change in electronic structure. If Rashba splitting is the origin of the two features, the addition of Cs^+ or Br^- could affect the spin-orbit coupling enough so that it is no longer possible to distinguish between the direct and indirect bandgaps.

4.3.2 Explanation of Kinetics

Previous studies have shown that carrier-carrier scattering, which is a multi-photon effect, is a key mechanism in hot-carrier thermalization and cooling.[10,48] The GSB probed at the bandgap is due to the cooling of hot-carriers to the bandgap, which happens through carrier-carrier scattering.[29]

Peak A, the broad bleach feature, has two possible origins. The first possibility is that electrons excited from the valence band (VB1) to the conduction band (CB) with excess energy cool to the band edge quickly and bleach the absorption at the band edge within the time resolution of our experiment, as illustrated in the simplified band diagram shown in Figure 6. For this origin to be correct, the electrons would require a very high carrier mobility, and although these materials are known to have high carrier mobilities, it is unlikely that such a large portion of the excited electrons are able to thermalize essentially instantly. The other possibility is that when the samples are pumped significantly above the bandgap, electrons are excited from a second valence band (VB2) to the CB. This is likely the largest contributor to the bleach feature pumped well above the bandgap at $t_2 = 0$ fs, as the presence of excited electrons at the CB band edge would lead to stimulated emission from CB1 to VB1 and decreased absorption from VB1 to CB1.[29,49] Peak A continues to increase in intensity over the first 400 fs as the holes also relax to the bandgap.

The time-scale of the decay of peak E (Figure 5a), is also consistent with that of hot-carrier cooling.[48,50] Peak E has previously been attributed to the renormalization of the bandgap due to

the presence of free-carriers. Our interest in the bandgap renormalization is that its decay gives an easily identifiable marker for carrier-dynamics. The decay of peak E is also correlated with the rise of peak A. The bandgap renormalization also appears to result in a red-shift of the GSB at shorter pump wavelengths. For instance, at $t_2 = 0$ fs, the peak of the GSB when pumping at 600 nm in $MAPbI_3$ is centered at 747 nm, but at 300 fs has shifted to 751 nm, and at our longest delay of 100 ps has shifted to 754 nm. For $MA_{0.75}FA_{0.25}PbI_3$, $MA_{0.5}FA_{0.5}PbI_3$, and $MA_{0.16}FA_{0.79}Cs_{0.05}PbI_{2.43}Br_{0.57}$, the center of the GSB pumped at 600 nm shifted from 748 nm to 759 nm, 771 nm to 777 nm, and 695 nm to 712 nm respectively. The position of the GSB pumped above the bandgap at longer waiting times is the same as the position of the GSB along the diagonal, within one or two nanometers. This equality suggests that the bandgap renormalization feature interferes with the GSB at short delays, obstructing the actual peak width and position of the GSB. However, because there is a bandgap renormalization, we would expect the GSB to red-shift even past where we see the GSB in the diagonal. This discrepancy has been attributed to Burstein-Moss band filling, where the density of states available at and near the bandgap is finite, thus as the states near the bandgap fill there should be a blue spectral shift.[33] Previous ultrafast experiments have indeed not only failed to see a red-shift due to bandgap renormalization, but a blue-shift of the GSB.[29] In our experiments we do not measure a blue-shift but see that the GSB remains constant with respect to the location of the diagonal peak. This difference between our experiments and previous measurements is due to the use of lower pump fluences, and therefore smaller carrier-concentrations in our experiments. In our experiments the maximum carrier densities are on the order of 10^{17} cm^{-3}, whereas the experiments where this blue-shift is observed have densities an order of magnitude larger. This would result in the bands filling to a lesser extent in our experiments and therefore a smaller blue-shift.

Further results indicative of hot-carrier cooling are the differences in kinetics of peak A pumped at 620 nm versus 710 nm (Figure 4f). When peak A is pumped at 620 nm it takes 300 fs for the peak to reach its maximum value, whereas if peak A is pumped at 710 nm, it only takes 100 fs for the peak to reach its equilibrium value for the remainder of the experiment. This change in rate as well as the non-linear fluence dependence at delays > 100 fs are also consistent with the growth of these features being due to hot-carrier cooling. Picturing the bands in k-space, hot-carriers closer to the band edge require a smaller change in momentum to reach the band edge, and therefore cool before carriers pumped higher above the bandgap (Figure 4.6). This figure is a very simplified band diagram to illustrate the phenomena of bandgap renormalization and carrier cooling. The hot-carriers are able to transfer momentum through carrier-carrier scattering, with the excess energy going into the lattice in the form of phonons.[50] As phonons are also present due to this relaxation, it is possible that carrier-phonon scattering also contributes to the carrier cooling.[10] We restrict our discussion to carrier-carrier scattering since we know from the data in Figure 5c that multi-photon effects contribute.

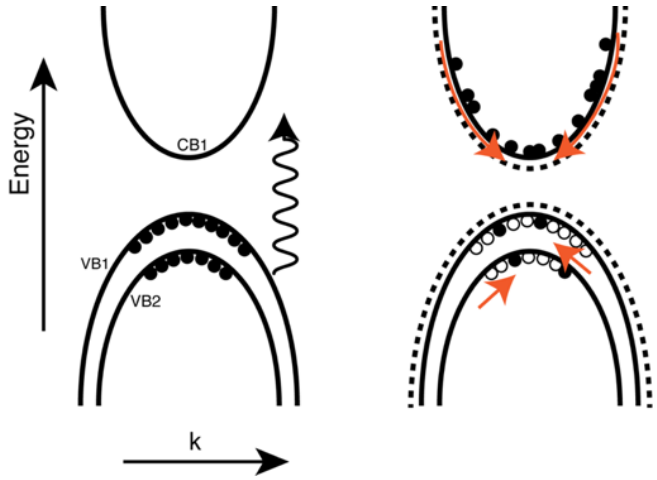

Figure 4.6. shows an extremely simplified band diagram cartoon of the lead-halide perovskites. The left side represents the valence bands filled with electrons (filled circles), and empty conduction band, and the right side depicts the occupation of the valence band with holes (empty circles) and conduction band with electrons. During the waiting time in our experiments, the excited electrons or holes will cool to the renormalized bandgap (dashed black lines). The cooling is represented with the orange arrows.

We were able to quantify the hot-carrier cooling by measuring the decay of the bandgap renormalization feature (feature E, most notable in Figure 4.2). Using a single exponential fit, we determined that this cooling has a time constant between 230-280 fs between the different samples (Table 2.). There are some small differences on the order of 1-10s of fs between the different samples, but the cooling happens at a remarkably similar rate for all four samples. The similar rates of carrier cooling suggests that this rate, although a potential reason for the good performance of perovskite devices compared to other materials, does not account for the differences in efficiency between different perovskite devices.

Table 4.1. Hot-carrier cooling time constants with one standard deviation

Composition	**τ_{cool} (fs)**
$MAPbI_3$	278.3 ± 16.4
$MA_{0.75}FA_{0.25}PbI_3$	274.6 ± 16.7
$MA_{0.5}FA_{0.5}PbI_3$	250.6 ± 12.2
$MA_{0.16}FA_{0.79}Cs_{0.05}PbI_{2.43}Br_{0.57}$	230.5 ± 20.2

4.4 Conclusions and Outlook

We report the first 2D WL spectra of mixed cation lead-halide perovskites. Due to the μ^4 scaling the diagonal features and cross-peaks which represent energy transfer, we were able to resolve an additional absorption feature at 720 nm, which undergoes fast energy transfer with the band edge. Our analysis of the sub-picosecond dynamics and carrier-density dependent measurements provide further evidence for carrier-carrier scattering as the mechanism for hot-carrier cooling. Through fitting of the 2D WL kinetics we show no difference in the hot-carrier cooling between the samples. Therefore it is unlikely that the carrier-carrier scattering leads to increased efficiency in mixed cation devices.

The application here of 2D WL spectroscopy to perovskite films is insightful because of the broad bandwidth of the spectra. Our spectrometer was built using a pulse-shaper that is compatible with the 100-200 kHz repetition rate ytterbium lasers, allowing phase control, pulse delays, and background correction to be altered shot-to-shot.[2,51] That capability makes possible new experiments on materials and photovoltaic materials. The high repetition rate also enables microscopies,[52–54] analogous to transient absorption microscopy used to measure exciton difficusion, for example, but with broad bandwidth imaging and multidimensional detection,[55] 2D WL microscopy has already been applied to organic thin crystals that undergo singlet fission.[56,57] We expect that the application reported here to perovskites will be followed by 2D hyperspectral imaging of similar materials, revealing the spatial extent of the energy landscape.

4. 5 Methods

4.5.1 Materials

Organic cation salts (methylammonium iodide (MAI), formamidinium iodide (FAI), methylammonium bromide (MABr), formamidinium bromide (FABr)) were purchased from Dyesol. Lead(II) iodide (PbI2) and lead(II) bromide (PbBr2) were purchased from TCI, and cesium iodide (CsI) was purchased from Sigma-Aldrich. N-N-dimethylformamide (DMF), dimethyl sulfoxide (DMSO), and chlorobenzene (CB) were purchased from Acros Organics.

4.5.2 Perovskite Precursor Preparation

Perovskite Precursor Synthesis

All solutions were prepared in an argon glovebox using a DMF:DMSO 4:1 (v:v) solvent system. MAPbI3 solution was prepared from precursor solutions of PbI2 (1.3 M). The PbI_2 solution was used to dissolve MAI powder, resulting in a 1.2 M solution of $MAPbI_3$. A 1.2 M $FAPbI_3$ solution was prepared by adding 1.3 M stock solution of PbI_2 to the appropriate amount

of FAI. Final solutions of $MA_xFA_{(1-x)}PbI_3$ were prepared by mixing the desired ratios of $MAPbI_3$:$FAPbI_3$ solutions by volume to synthesize samples 1, 2, and 3.

Sample 4 was made by first dissolving making 1.5 M solutions of both PbI_2 and $PbBr_2$ in the DMF:DMSO 4:1 (v:v) solvent system. The PbI_2 solution was then used to dissolve FAI, resulting in a 1.2 M solution of FAPbI. The $PbBr_2$ solution was used to dissolve MABr, resulting in a 1.2 M solution of $MAPbBr_3$. A 1.2 M solution of CsI was made by dissolving solid CsI in DMSO. To make the final mixed-cation-mixed-halide lead perovskite the solutions were combined with a ration of $FAPbI_3$:$MAPbBr_3$:CsI=950:190:60 (v/v/v).

Perovskite Film Deposition

Glass microscope slides (Thermo Fisher) were cleaned first with 10% Hellmanex solution, followed by ethanol, and then blow-dried. The substrates were further cleaned with a 15 min UV-ozone treatment immediately before deposition. The perovskite thin films were deposited via a two-step spin coating method using the antisolvent method in a dry air-filled glovebox. A 50 µL portion of perovskite precursor was deposited onto the substrate and first spun at 1000 rpm for 10 s followed by 4000 rpm for 20 s. During the second step, 200 µL of chlorobenzene antisolvent was dynamically deposited with 10 s left in the program. The samples were then annealed at 100 C for 1 hour in a dry air-filled glovebox. Substrates were allowed to cool and then encapsulated in the dry air environment using a glass cover slip and epoxy (Araldite) before being removed from the glovebox for measurements. UV-Vis absorption spectra were taken on a Varian Cary 5 spectrometer scanning from 200-800 nm.

4.5.3 2D WL Spectroscopy

The 2D WL spectrometer used for our measurements was described in detail previously[2]. Briefly, 10 µJ of the output of a 100-kHz Yb oscillator (Spirit, Spectra Physics) was split equally

into pump and probe arms and pumped an 8 mm and 4 mm YAG crystal respectively to generate supercontinuum pulses. A quartz acousto-optic modulator (PhaseTech Spectroscopy) incremented the 2D pulse sequence shot-to-shot using an eight-frame pulse sequence and increased t_1 in steps of 2 fs from 0 to 98 fs. The pump pulse-duration and phase were measured using polarization-gating frequency resolved optical gating.[41] The home-built pulse shaper was used to compensate for the dispersion induced by the quartz AOM, to give a pump pulse-duration of 35 fs. The pump fluence at the sample was 4.92×10^{-6} J/cm^2. Transient absorption measurements are performed similarly, except the t_1 is held constant at 0 fs.

4.6 References

(1) Mehlenbacher, R. D.; McDonough, T. J.; Grechko, M.; Wu, M.-Y.; Arnold, M. S.; Zanni, M. T. Energy Transfer Pathways in Semiconducting Carbon Nanotubes Revealed Using Two-Dimensional White-Light Spectroscopy. *Nature Communications* **2015**, *6* (1).
(2) Kearns, N. M.; Mehlenbacher, R. D.; Jones, A. C.; Zanni, M. T. Broadband 2D Electronic Spectrometer Using White Light and Pulse Shaping: Noise and Signal Evaluation at 1 and 100 KHz. *Opt. Express, OE* **2017**, *25* (7), 7869–7883.
(3) Jonas, D. M. Two-Dimensional Femtosecond Spectroscopy. *Annual Review of Physical Chemistry* **2003**, *54* (1), 425–463.
(4) Hamm, P.; Zanni, M. T. *Concepts and Methods of 2d Infrared Spectroscopy*; Cambridge University Pres: Cambridge ; New York, 2011.
(5) Fuller, F. D.; Ogilvie, J. P. Experimental Implementations of Two-Dimensional Fourier Transform Electronic Spectroscopy. *Annual Review of Physical Chemistry* **2015**, *66* (1), 667–690.
(6) Schlau-Cohen, G. S.; Calhoun, T. R.; Ginsberg, N. S.; Read, E. L.; Ballottari, M.; Bassi, R.; van Grondelle, R.; Fleming, G. R. Pathways of Energy Flow in LHCII from Two-Dimensional Electronic Spectroscopy. *J. Phys. Chem. B* **2009**, *113* (46), 15352–15363.
(7) Fassioli, F.; Dinshaw, R.; Arpin, P. C.; Scholes, G. D. Photosynthetic Light Harvesting: Excitons and Coherence. *J. R. Soc. Interface.* **2014**, *11* (92), 20130901.
(8) Son, M.; Pinnola, A.; Gordon, S. C.; Bassi, R.; Schlau-Cohen, G. S. Observation of Dissipative Chlorophyll-to-Carotenoid Energy Transfer in Light-Harvesting Complex II in Membrane Nanodiscs. *Nat Commun* **2020**, *11* (1), 1295.
(9) Zhu, W.; Spencer, A. P.; Mukherjee, S.; Alzola, J. M.; Sangwan, V. K.; Amsterdam, S. H.; Swick, S. M.; Jones, L. O.; Heiber, M. C.; Herzing, A. A.; Li, G.; Stern, C. L.; DeLongchamp, D. M.; Kohlstedt, K. L.; Hersam, M. C.; Schatz, G. C.; Wasielewski, M. R.; Chen, L. X.; Facchetti, A.; Marks, T. J. Crystallography, Morphology, Electronic Structure, and Transport in Non-Fullerene/Non-Indacenodithienothiophene Polymer:Y6 Solar Cells. *J. Am. Chem. Soc.* **2020**, *142* (34), 14532–14547.
(10) Richter, J. M.; Branchi, F.; Camargo, F. V. de A.; Zhao, B.; Friend, R. H.; Cerullo, G.; Deschler, F. Ultrafast Carrier Thermalization in Lead Iodide Perovskite Probed with Two-Dimensional Electronic Spectroscopy. *Nature Communications* **2017**, *8* (1), 376.
(11) Green, M. A.; Ho-Baillie, A.; Snaith, H. J. The Emergence of Perovskite Solar Cells. *Nature Photonics* **2014**, *8* (7), 506–514.
(12) Herz, L. M. Charge-Carrier Dynamics in Organic-Inorganic Metal Halide Perovskites. *Annual Review of Physical Chemistry* **2016**, *67* (1), 65–89.
(13) Even, J.; Pedesseau, L.; Katan, C. Analysis of Multivalley and Multibandgap Absorption and Enhancement of Free Carriers Related to Exciton Screening in Hybrid Perovskites. *J. Phys. Chem. C* **2014**, *118* (22), 11566–11572.
(14) Sun, S.; Salim, T.; Mathews, N.; Duchamp, M.; Boothroyd, C.; Xing, G.; Sum, T. C.; Lam, Y. M. The Origin of High Efficiency in Low-Temperature Solution-Processable Bilayer Organometal Halide Hybrid Solar Cells. *Energy Environ. Sci.* **2014**, *7* (1), 399–407.
(15) Sestu, N.; Cadelano, M.; Sarritzu, V.; Chen, F.; Marongiu, D.; Piras, R.; Mainas, M.; Quochi, F.; Saba, M.; Mura, A.; Bongiovanni, G. Absorption F-Sum Rule for the Exciton Binding Energy in Methylammonium Lead Halide Perovskites. *J. Phys. Chem. Lett.* **2015**, *6* (22), 4566–4572.
(16) Shi, D.; Adinolfi, V.; Comin, R.; Yuan, M.; Alarousu, E.; Buin, A.; Chen, Y.; Hoogland, S.; Rothenberger, A.; Katsiev, K.; Losovyj, Y.; Zhang, X.; Dowben, P. A.; Mohammed, O. F.;

Sargent, E. H.; Bakr, O. M. Low Trap-State Density and Long Carrier Diffusion in Organolead Trihalide Perovskite Single Crystals. *Science* **2015**, *347* (6221), 519–522.
(17) Kedem, N.; Brenner, T. M.; Kulbak, M.; Schaefer, N.; Levcenko, S.; Levine, I.; Abou-Ras, D.; Hodes, G.; Cahen, D. Light-Induced Increase of Electron Diffusion Length in a p–n Junction Type $CH_3NH_3PbBr_3$ Perovskite Solar Cell. *J. Phys. Chem. Lett.* **2015**, *6* (13), 2469–2476.
(18) Zhao, Y.; Nardes, A. M.; Zhu, K. Solid-State Mesostructured Perovskite $CH_3NH_3PbI_3$ Solar Cells: Charge Transport, Recombination, and Diffusion Length. *J. Phys. Chem. Lett.* **2014**, *5* (3), 490–494.
(19) Kojima, A.; Teshima, K.; Shirai, Y.; Miyasaka, T. Organometal Halide Perovskites as Visible-Light Sensitizers for Photovoltaic Cells. *J. Am. Chem. Soc.* **2009**, *131* (17), 6050–6051.
(20) Best Research-Cell Efficiencies. NREL. https://www.nrel.gov/pv/assets/images/efficiency-chart.png. Accessed 8/11/2021.
(21) Yoo, J. J.; Seo, G.; Chua, M. R.; Park, T. G.; Lu, Y.; Rotermund, F.; Kim, Y.-K.; Moon, C. S.; Jeon, N. J.; Correa-Baena, J.-P.; Bulović, V.; Shin, S. S.; Bawendi, M. G.; Seo, J. Efficient Perovskite Solar Cells via Improved Carrier Management. *Nature* **2021**, *590* (7847), 587–593.
(22) Stoumpos, C. C.; Malliakas, C. D.; Kanatzidis, M. G. Semiconducting Tin and Lead Iodide Perovskites with Organic Cations: Phase Transitions, High Mobilities, and Near-Infrared Photoluminescent Properties. *Inorg. Chem.* **2013**, *52* (15), 9019–9038.
(23) Turren-Cruz, S.-H.; Hagfeldt, A.; Saliba, M. Methylammonium-Free, High-Performance, and Stable Perovskite Solar Cells on a Planar Architecture. *Science* **2018**, *362* (6413), 449–453.
(24) Meloni, S.; Palermo, G.; Ashari-Astani, N.; Grätzel, M.; Rothlisberger, U. Valence and Conduction Band Tuning in Halide Perovskites for Solar Cell Applications. *J. Mater. Chem. A* **2016**, *4* (41), 15997–16002.
(25) Eperon, G. E.; Stranks, S. D.; Menelaou, C.; Johnston, M. B.; Herz, L. M.; Snaith, H. J. Formamidinium Lead Trihalide: A Broadly Tunable Perovskite for Efficient Planar Heterojunction Solar Cells. *Energy Environ. Sci.* **2014**, *7* (3), 982–988.
(26) Xu, Z.; Liu, Z.; Li, N.; Tang, G.; Zheng, G.; Zhu, C.; Chen, Y.; Wang, L.; Huang, Y.; Li, L.; Zhou, N.; Hong, J.; Chen, Q.; Zhou, H. A Thermodynamically Favored Crystal Orientation in Mixed Formamidinium/Methylammonium Perovskite for Efficient Solar Cells. *Advanced Materials* **2019**, *31* (24), 1900390.
(27) Chen, J.; Messing, M. E.; Zheng, K.; Pullerits, T. Cation-Dependent Hot Carrier Cooling in Halide Perovskite Nanocrystals. *J. Am. Chem. Soc.* **2019**, *141* (8), 3532–3540.
(28) Smallwood, C. L.; Cundiff, S. T. Multidimensional Coherent Spectroscopy of Semiconductors. *Laser & Photonics Reviews* **2018**, *12* (12), 1800171.
(29) Manser, J. S.; Kamat, P. V. Band Filling with Free Charge Carriers in Organometal Halide Perovskites. *Nature Photonics* **2014**, *8* (9), 737–743.
(30) Camargo, F. V. A.; Nagahara, T.; Feldmann, S.; Richter, J. M.; Friend, R. H.; Cerullo, G.; Deschler, F. Dark Subgap States in Metal-Halide Perovskites Revealed by Coherent Multidimensional Spectroscopy. *J. Am. Chem. Soc.* **2020**, *142* (2), 777–782.
(31) Yang, Y.; Ostrowski, D. P.; France, R. M.; Zhu, K.; van de Lagemaat, J.; Luther, J. M.; Beard, M. C. Observation of a Hot-Phonon Bottleneck in Lead-Iodide Perovskites. *Nature Photonics* **2016**, *10* (1), 53–59.
(32) Rivett, J. P. H.; Tan, L. Z.; Price, M. B.; Bourelle, S. A.; Davis, N. J. L. K.; Xiao, J.; Zou, Y.; Middleton, R.; Sun, B.; Rappe, A. M.; Credgington, D.; Deschler, F. Long-Lived Polarization Memory in the Electronic States of Lead-Halide Perovskites from Local Structural Dynamics. *Nature Communications* **2018**, *9* (1), 3531.

(33) Price, M. B.; Butkus, J.; Jellicoe, T. C.; Sadhanala, A.; Briane, A.; Halpert, J. E.; Broch, K.; Hodgkiss, J. M.; Friend, R. H.; Deschler, F. Hot-Carrier Cooling and Photoinduced Refractive Index Changes in Organic–Inorganic Lead Halide Perovskites. *Nature Communications* **2015**, *6*, 8420.
(34) Yamada, Y.; Nakamura, T.; Endo, M.; Wakamiya, A.; Kanemitsu, Y. Photocarrier Recombination Dynamics in Perovskite CH3NH3PbI3 for Solar Cell Applications. *J. Am. Chem. Soc.* **2014**, *136* (33), 11610–11613.
(35) Miyata, A.; Mitioglu, A.; Plochocka, P.; Portugall, O.; Wang, J. T.-W.; Stranks, S. D.; Snaith, H. J.; Nicholas, R. J. Direct Measurement of the Exciton Binding Energy and Effective Masses for Charge Carriers in Organic–Inorganic Tri-Halide Perovskites. *Nature Physics* **2015**, *11* (7), 582–587.
(36) Jha, A.; Duan, H.-G.; Tiwari, V.; Nayak, P. K.; Snaith, H. J.; Thorwart, M.; Miller, R. J. D. Direct Observation of Ultrafast Exciton Dissociation in Lead Iodide Perovskite by 2D Electronic Spectroscopy. *ACS Photonics* **2018**, *5* (3), 852–860.
(37) Shah, J. *Ultrafast Spectroscopy of Semiconductors and Semiconductor Nanostructures*; Springer series in solid-state sciences; Springer: Berlin ; New York, 1996.
(38) Petti, M. K.; Lomont, J. P.; Maj, M.; Zanni, M. T. Two-Dimensional Spectroscopy Is Being Used to Address Core Scientific Questions in Biology and Materials Science. *J. Phys. Chem. B* **2018**, 10.
(39) Saliba, M.; Matsui, T.; Seo, J.-Y.; Domanski, K.; Correa-Baena, J.-P.; Nazeeruddin, M. K.; Zakeeruddin, S. M.; Tress, W.; Abate, A.; Hagfeldt, A.; Grätzel, M. Cesium-Containing Triple Cation Perovskite Solar Cells: Improved Stability, Reproducibility and High Efficiency. *Energy Environ. Sci.* **2016**, *9* (6), 1989–1997.
(40) Jacobsson, T. J.; Correa-Baena, J.-P.; Pazoki, M.; Saliba, M.; Schenk, K.; Grätzel, M.; Hagfeldt, A. Exploration of the Compositional Space for Mixed Lead Halogen Perovskites for High Efficiency Solar Cells. *Energy & Environmental Science* **2016**, *9* (5), 1706–1724.
(41) Filip, M. R.; Eperon, G. E.; Snaith, H. J.; Giustino, F. Steric Engineering of Metal-Halide Perovskites with Tunable Optical Band Gaps. *Nature Communications* **2014**, *5*, 5757.
(42) Wong, C. Y.; Scholes, G. D. Using Two-Dimensional Photon Echo Spectroscopy to Probe the Fine Structure of the Ground State Biexciton of CdSe Nanocrystals. *Journal of Luminescence* **2011**, *131* (3), 366–374.
(43) Jacobsson, T. J.; Schwan, L. J.; Ottosson, M.; Hagfeldt, A.; Edvinsson, T. Determination of Thermal Expansion Coefficients and Locating the Temperature-Induced Phase Transition in Methylammonium Lead Perovskites Using X-Ray Diffraction. *Inorg. Chem.* **2015**, *54* (22), 10678–10685.
(44) Glaser, T.; Müller, C.; Sendner, M.; Krekeler, C.; Semonin, O. E.; Hull, T. D.; Yaffe, O.; Owen, J. S.; Kowalsky, W.; Pucci, A.; Lovrinčić, R. Infrared Spectroscopic Study of Vibrational Modes in Methylammonium Lead Halide Perovskites. *J. Phys. Chem. Lett.* **2015**, *6* (15), 2913–2918.
(45) Zheng, F.; Tan, L. Z.; Liu, S.; Rappe, A. M. Rashba Spin–Orbit Coupling Enhanced Carrier Lifetime in $CH_3NH_3PbI_3$. *Nano Lett.* **2015**, *15* (12), 7794–7800.
(46) Azarhoosh, P.; McKechnie, S.; Frost, J. M.; Walsh, A.; van Schilfgaarde, M. Research Update: Relativistic Origin of Slow Electron-Hole Recombination in Hybrid Halide Perovskite Solar Cells. *APL Materials* **2016**, *4* (9), 091501.
(47) Becker, M. A.; Vaxenburg, R.; Nedelcu, G.; Sercel, P. C.; Shabaev, A.; Mehl, M. J.; Michopoulos, J. G.; Lambrakos, S. G.; Bernstein, N.; Lyons, J. L.; Stöferle, T.; Mahrt, R. F.;

Kovalenko, M. V.; Norris, D. J.; Rainò, G.; Efros, A. L. Bright Triplet Excitons in Caesium Lead Halide Perovskites. *Nature* **2018**, *553* (7687), 189–193.
(48) Hopper, T. R.; Gorodetsky, A.; Frost, J. M.; Müller, C.; Lovrincic, R.; Bakulin, A. A. Ultrafast Intraband Spectroscopy of Hot-Carrier Cooling in Lead-Halide Perovskites. *ACS Energy Lett.* **2018**, *3* (9), 2199–2205.
(49) Xing, G.; Mathews, N.; Sun, S.; Lim, S. S.; Lam, Y. M.; Grätzel, M.; Mhaisalkar, S.; Sum, T. C. Long-Range Balanced Electron- and Hole-Transport Lengths in Organic-Inorganic CH3NH3PbI3. *Science* **2013**, *342* (6156), 344–347.
(50) Bretschneider, S. A.; Ivanov, I.; Wang, H. I.; Miyata, K.; Zhu, X.; Bonn, M. Quantifying Polaron Formation and Charge Carrier Cooling in Lead-Iodide Perovskites. *Advanced Materials* **2018**, *30* (29), 1707312.
(51) Jones, A. C.; Kunz, M. B.; Tigges-Green, I.; Zanni, M. T. Dual Spectral Phase and Diffraction Angle Compensation of a Broadband AOM 4-f Pulse-Shaper for Ultrafast Spectroscopy. *Opt. Express, OE* **2019**, *27* (26), 37236–37247.
(52) Blach, D. D.; Zheng, W.; Liu, H.; Pan, A.; Huang, L. Carrier Transport Across a CdS_xSe_{1-x} Lateral Heterojunction Visualized by Ultrafast Microscopy. *J. Phys. Chem. C* **2020**, *124* (21), 11325–11332.
(53) Gabriel, M. M.; Kirschbrown, J. R.; Christesen, J. D.; Pinion, C. W.; Zigler, D. F.; Grumstrup, E. M.; Mehl, B. P.; Cating, E. E. M.; Cahoon, J. F.; Papanikolas, J. M. Direct Imaging of Free Carrier and Trap Carrier Motion in Silicon Nanowires by Spatially-Separated Femtosecond Pump–Probe Microscopy. *Nano Lett.* **2013**, *13* (3), 1336–1340.
(54) Colon, B. A.; Hassan, M. R.; Saleheen, A.; Baker, C. A.; Calhoun, T. R. Total Internal Reflection Transient Absorption Microscopy: An Online Detection Method for Microfluidics. *J. Phys. Chem. A* **2020**, *124* (20), 4160–4170.
(55) Jones, A. C.; Kearns, N. M.; Bohlmann Kunz, M.; Flach, J. T.; Zanni, M. T. Multidimensional Spectroscopy on the Microscale: Development of a Multimodal Imaging System Incorporating 2D White-Light Spectroscopy, Broadband Transient Absorption, and Atomic Force Microscopy. *J. Phys. Chem. A* **2019**, *123* (50), 10824–10836.
(56) Jones, A. C.; Kearns, N. M.; Ho, J.-J.; Flach, J. T.; Zanni, M. T. Impact of Non-Equilibrium Molecular Packings on Singlet Fission in Microcrystals Observed Using 2D White-Light Microscopy. *Nature Chemistry* **2019**, 1–8.
(57) Armstrong, Z. T.; Kunz, M. B.; Jones, A. C.; Zanni, M. T. Thermal Annealing of Singlet Fission Microcrystals Reveals the Benefits of Charge Transfer Couplings and Slip-Stacked Packing. *J. Phys. Chem. C* **2020**, *124* (28), 15123–15131.
(58) Trebino, R.; DeLong, K. W.; Fittinghoff, D. N.; Sweetser, J. N.; Krumbügel, M. A.; Richman, B. A.; Kane, D. J. Measuring Ultrashort Laser Pulses in the Time-Frequency Domain Using Frequency-Resolved Optical Gating. *Review of Scientific Instruments* **1997**, *68* (9), 3277–3295.

5. Time-domain photothermal AFM spectroscopy via femtosecond pulse shaping.

A time-domain version of photothermal microscopy using an atomic force microscope (AFM) is reported, which we call Fourier transform photothermal (FTPT) spectroscopy, where the delay between two laser pulses is varied and the Fourier transform computed. An acousto-optic modulator based pulse shaper sets the delay and phases of the pulses shot-to-shot at 100 kHz, enabling background subtraction and data collection in the rotating frame. The pulse shaper is also used to flatten the pulse spectrum, thereby eliminating the need for normalization by the laser spectrum. We demonstrate the method on 6,13-bis(triisopropylsilylethynyl)pentacene (TIPS-Pn) microcrystals and Mn-phthalocyanine islands, confirming sub-diffraction spatial resolution, and providing new spectroscopic insights likely linked to structural defects in the crystals.

Acknowledgements

Reprinted with permission from *Analytical Chemistry*, 10.1021/acs.analchem.2c01920.

5.1 Introduction

Some of the most interesting and least well understood variation of material properties occurs at sub-diffraction length scales, such as the structural variation between grains in a thin film,[1–3] the behavior of an isolated nanoparticle,[4,5] or edge effects in a single crystal.[6–8] These regions are often of interest because the variation at grain boundaries and the edge effects in single crystals can perturb the electronic structure significantly resulting in increased or decreased charge carrier generation or mobility when used in photovoltaic devices,[9,10] whereas nanoparticles have shown to be catalysts for various reactions, which is strongly affected by the electronic

structure.[11,12] Ideally, the spectroscopic information of each region would be measured separately, but in typical far-field microscopies where the spatial resolution is limited by the diffraction of light, the responses from each of these regions are convoluted with one another.

There are various methods of sub-diffraction limit imaging, including electron microscopy, fluorescence techniques such as stochastic optical reconstruction microscopy[13] and reversible saturable optical fluorescence transitions (RESOLFT) techniques,[14–16] as well as scanning probe techniques such as scanning tunneling microscopy (STM)[17] and atomic force microscopy (AFM).[18] Scanning probe microscopies in combination with light-matter interactions have been used to measure spectroscopic information with sub-diffraction limit spatial resolution.[19,20] Two of these most common scanning probe spectroscopic techniques are scanning scattering near-field optical microscopy (s-SNOM)[21] and AFM infrared spectroscopy (AFM-IR). AFM-IR is closely related to the technique presented here. AFM-IR is a photothermal method, in which a tunable-wavelength laser pulse illuminates the sample and if the light is absorbed, the photon energy ultimately becomes thermal energy, leading to an increase in temperature, a thermal expansion, and thereby an upward force on the AFM cantilever that is in contact with the sample, causing it to oscillate.[22] The amplitude of this oscillation is proportional to the amount of light absorbed.[23–25] The AFM-IR principle has also been used to measure visible light absorption.[26] Previous implementations of AFM detected spectroscopy have measured the degradation of $MAPbI_3$ films,[27] mapped domains in metal organic frameworks with mixed linkers,[28] and chemically mapped cancer cells.[29] For more detail on previous AFM detected spectroscopies and nanoscale imaging, we direct the reader to recent reviews on the topic.[30,31]

Here, we present the first implementation of Fourier transform photothermal (FTPT) spectroscopy. To date, photothermal AFM detection has almost exclusively been implemented in

the frequency domain, where the cantilever response is measured as a function of laser frequency. Our method operates in the time-domain, where instead of scanning the frequency of the excitation pulse, we scan the time delay between two laser pulses to measure a free-induction decay (FID). We then Fourier transform this FID to retrieve the absorption spectrum. The approach is analogous to time-domain methods using a Michelson interferometer in scattering-type scanning nearfield optical microscopy (s-SNOM) measurements,[32] and with incoherent light and a Michelson interferometer using synchrotron broadband-IR sources,[33,34] albeit the pulse shaper used here enables new modes of data collection not previously possible, such as data collection utilizing phase cycling, a rotating frame, time-delay reordering, and the creation of a flat laser spectrum. The method presented here uses an ultrafast visible supercontinuum created simply by pumping a bulk material, 8 mm YAG, with less than 4 μJ of 1040 nm fundamental power. The advantage of the presented method versus previous time-domain methods in the IR is that it can be done with a commercially available light source. In addition, the use of coherent femtosecond pulses gives the method potential for being extended to a multidimensional method, with both high temporal and spatial resolution, which would not be possible with nanosecond pulses. We demonstrate the capabilities here, explain the theory behind the approach, and detail the technical factor necessary to implement the technique.

5.2 Experimental

Our Fourier transform photothermal experiment adapts a previously described 2D white light microscope[35] as shown in Figure 5.1. Briefly, 5 μJ of a 100 kHz Yb amplifier centered at 1040 nm pumps an 8 mm YAG crystal to create a supercontinuum. This supercontinuum is then compressed using broadband chirped mirrors (Layertec) and phase compensation in an acousto-optic modulator pulse shaper[36]. The spectrum of the shaped light is measured by directing the light

immediately after the pulse shaper into a spectrometer, where it is dispersed by a grating and focused onto a CCD line scan camera (e2V AviivA EM4). The spectral range of the white light is 520-800 nm, although this is mostly windowed to 540-720 nm, as described in more detail below. The delay time possible with an AOM pulse shaper are only limited by a maximum possible delay, which is on the order of picoseconds and is much greater than the final delay needed for electronic transitions. The size of the delay time steps determines the maximum frequency (minimum wavelength) resolvable, and the final delay time determines the spectral resolution, which is 260 cm^{-1} for all spectra reported here. The deflected light from the pulse shaper is directed into an AFM (Molecular Vista) from below the sample using a reflective objective, which focuses the beam to a spot size of approximately one micrometer.[35] An achromatic half waveplate rotates the polarization of the light relative to the sample in the microscope. The beam is aligned beneath the AFM tip (HQ:NSC14/Pt MikroMasch) by scanning the position of the reflective objective while the AFM tip is in contact with the sample. The AFM probe used has a moderate force constant of 5 N/m, a diameter of less than 30 nm, and a free resonance near 160 kHz. The AFM probe takes 60 μs to return to equilibrium after being excited by sample expansion. The position of the beam relative to the AFM tip is set to maximize the deflection of the continuous wave laser reflecting off the back of the AFM probe.

An optically detected linear absorption spectrum on a single 6,13-bis(triisopropylsilylethynyl)pentacene (TIPS-Pn) crystal was measured on the CCD line scan camera using the FTPT microscope. After the sample, the light was recollimated in a transmissive objective, coupled into an optical fiber, and directed into a spectrometer. The light used in all the microscope and FTPT experiments was linearly polarized. For a photothermal imaging experiment, a single supercontinuum pulse is used. To scan the position, the objective and AFM

positions are fixed, and the sample stage is translated. The topography and photothermal information are collected simultaneously. The signal collected in a photothermal image represents the total absorption at all wavelengths for a given position on the sample, and the amount of time averaged per pixel is approximately 50 ms.

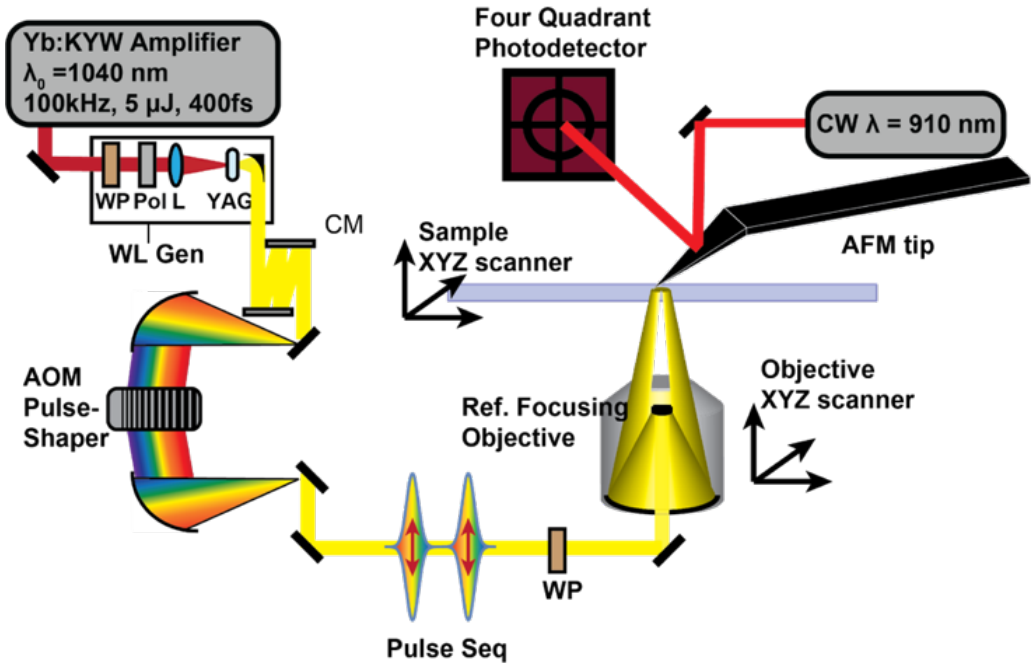

Figure 5.1. The experimental design and layout. WP: waveplate, Pol: polarizer, L: lens, CM: chirped mirrors.

Films of 6,13-bis(triisopropylsilylethynyl)pentacene (TIPS-Pn) microcrystals were grown by drop casting 100 µL of 5 mg/mL TIPS-Pn in toluene onto a microscope slide held at 50 °C to create crystals that were 10-20 µm in width, 100-300 nm in height, and several millimeters in length. The bulk absorption spectrum of the TIPS-Pn microcrystal film was measured using a standard UV-Vis spectrometer (Cary UV-Vis Spectrophotometer). Islands of Mn-pthalocyanine (MnPc) were made by drop casting a filtered saturated solution of MnPc in DMSO (<0.5 mg/mL)

onto a glass slide held at room temperature for 72 hours resulting in a featureless amorphous film. This film was solvent annealed in chloroform vapor for 12 hours, resulting in small islands of crystalline MnPc.

5.3 Theory of FTPT spectroscopy

In this section we cover some of the mathematical principles used to collect FTPT spectra. The pulse shaper is used to generate two femtosecond pulses, as depicted in Figure 5.2a and b, separated by a time delay $t = \tau_1 - \tau_2$. Each pulse has a phase, φ_n. We want to measure the heat caused by the pair of pulses, but each individual pulse also heats the sample, creating a background. Shown in Figure 5.2c are the Feynman diagrams for the background and desired signal. In this formalism, heat is created when the pulses end in an excited state population, $|e\rangle\langle e|$, that subsequently relaxes to the ground state as the sample thermalizes. Thermalization causes a temperature rise, $\Delta T^{(n)}$, and an expansion of the sample. To create a population state, the sample must interact twice with the pulse electric fields, *E*. For the two background pathways (i) and (ii), the two electric field interactions will occur within the width of a single pulse, centered at either τ_1 or τ_2, and give temperature rises $\Delta T^{(1)}$ and $\Delta T^{(2)}$, respectively. The signal pathway (iii) is by pulse one, E_1, and pulse two, E_2, each interacting once with the sample at τ_1 and τ_2 respectively, thereby spaced by $t = \tau_2 - \tau_1$, which we refer to as the delay time. This pathway also ends in an excited population and decays back to the ground state through the same non-radiative mechanism as pathways (i) and (ii), resulting in another increase in temperature, $\Delta T^{(12)}$.

The response functions, R_n, for each Feynman pathway are given in Equation 5.1.

$$R_1 \propto i{\mu_{ge}}^2$$

$$R_2 \propto i{\mu_{ge}}^2 \tag{5.1}$$

$$R_3 \propto i{\mu_{ge}}^2 e^{-i\omega_{ge}(\tau_1-\tau_2)} e^{-(\tau_1-\tau_2)/T_2} = i{\mu_{ge}}^2 e^{-it\omega_{ge}} e^{-t/T_2}$$

Where ω_{ge} is the resonant frequency for the transition from ground to excited state, μ_{ge} is the transition dipole moment, and T_2 is the homogeneous dephasing, which takes into account population relaxation and fluctuations of the environment.[37] The notation follows that of Hamm and Zanni (Cambridge Univ Press).[37] From these three expressions for the response functions, it is clear that R_1 and R_2 are not dependent on the time between the two pulses, but the real value of R_3 oscillates as a function of the delay time. In other words, because pathway (iii) depends on *t*, the temperature in the sample is modulated by the delay time.

The signal is given by the convolution of the response functions with the electric fields of the laser pulses,

$$S(\tau) \propto E(\tau) \otimes R(\tau)$$

$$E(\tau) \propto A(\tau) e^{\pm i\omega_c \tau \mp i\varphi \mp i\vec{k}\cdot\vec{r}} \tag{5.2}$$

, where ω_c is the carrier frequency of the electric field, which in the limit of δ-function envelopes becomes

$$S(\tau) \propto iE_1(\tau_1)E_1^*(\tau_1)R_1 + iE_2(\tau_2)E_2^*(\tau_2)R_2 + iE_1(\tau_1)E_2^*(\tau_2)R_3 \tag{5.3}$$

which gives

$$S(t) \propto I_1 {\mu_{ge}}^2 + I_2 {\mu_{ge}}^2 + I_{12} e^{it(\omega_c - \omega_{ge})} e^{-i\Delta\varphi_{12}} {\mu_{ge}}^2 \tag{5.4}$$

$$\propto \Delta T^{(1)} + \Delta T^{(2)} + \Delta T^{(12)}(t)$$

Where $\Delta\varphi_{12}$ is the relative phase between E_1 and E_2, and I_n is the intensity of the laser pulse-pair. The intensity, I_n, should be the same for pulse one and pulse two and the interaction with both pulses. Equation 5.4 is experimentally measured and plotted as the FID. The phase, $\Delta\varphi_{12}$, can be changed as a function of the delay time to operate in a rotating frame, thereby lowering the Nyquist

frequency.[38] The use of an ultrafast pulse shaper in these experiments allows for a rotating frame of 11,000 cm^{-1} to be used for all measurements presented here. In addition, a Gaussian window function with a width of 40 fs was used to minimize the noise for delay times after the signal had decayed to a level below the noise threshold.

In our experiment, photons are not directly measured. Instead, the heat generated by the absorbed photon causes an expansion of the sample, which the AFM detects. The thermal expansion is also dependent on the thermal expansion coefficients and thermal diffusivity.[23] Experimentally, the contribution from each pathway will result in an increase in temperature, $\Delta T^{(1)}$, $\Delta T^{(2)}$, and $\Delta T^{(12)}$, all causing an expansion as shown in Figure 5.2d. $\Delta T^{(1)}$ and $\Delta T^{(2)}$ are independent of the delay time. Whereas $\Delta T^{(12)}$ will depend on the delay time, creating an oscillation, as shown in Figure 5.2e. Previous theoretical work has shown that the maximum deflection of the AFM cantilever due to the expansion of the sample is linearly proportional to the amount of light absorbed,[23] and which we demonstrate for our setup in Figure 5.3d. Thus, the Fourier transform gives the desired spectrum.

$$S(\omega) = \int_0^\infty S(t) e^{i\omega t} dt \tag{5.5}$$

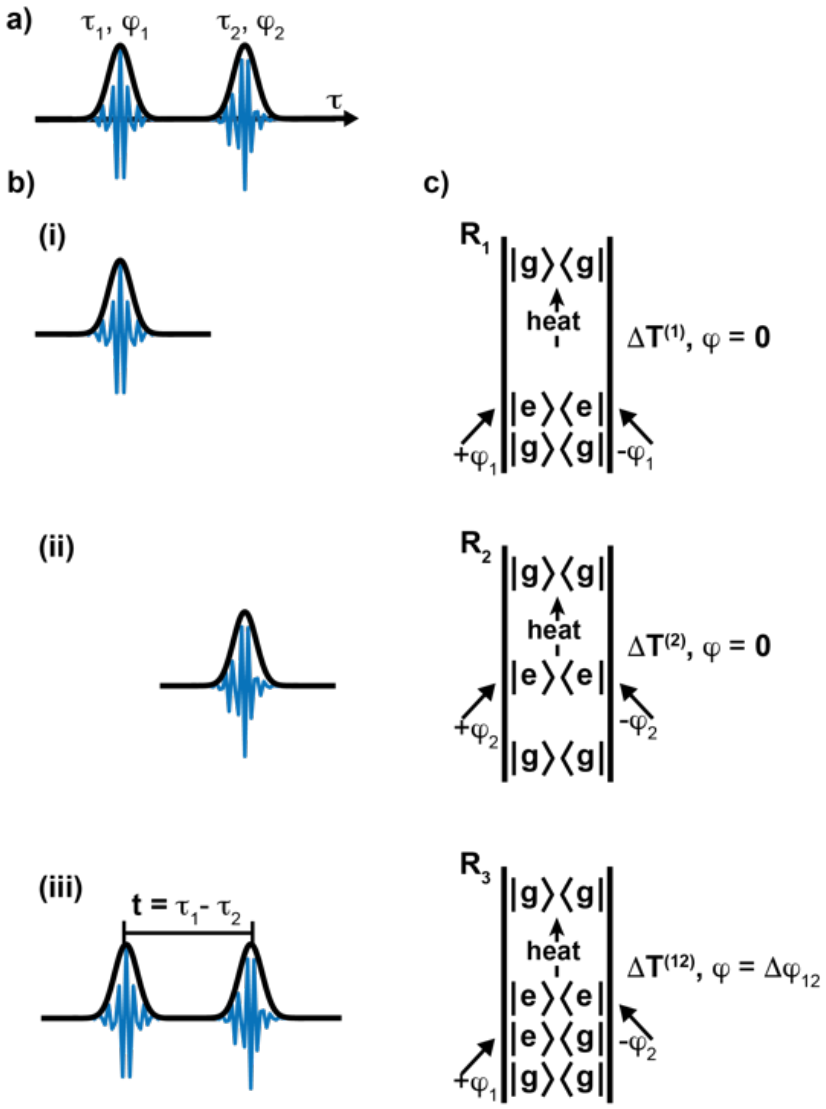

Figure 5.2. Formalism behind FTPT measurements. Each pulse pair (a), with a delay time, *t*, has three possible pathways that lead to absorption in the sample (b, c). Feynman diagrams (i) and (ii) show pathways where pulse one and pulse two respectively each interact with the sample twice. Feynman diagram (iii) illustrates the scenario where each pulse interacts with the sample once, and therefore it is dependent both on the phase and delay time of the pulse pair.

5.4 Results and Discussion

Shown in Figure 5.3 is the application of FTPT to microcrystals of TIPS-Pn. The absorption spectrum of TIPS-Pn is discussed in more detail below, but for this section the nature

of the sample is not important. Figure 5.3a shows the AFM response for three different time delays, *t*. After each pair of pulses, the AFM probe is deflected, followed by oscillations of the probe, which last 60 μs. The intensity and phase of the AFM oscillations depends on the phases and delay time of the pulses, according to Equation 5.4. To measure an FID of the response, the maximum value of the AFM oscillations for each laser shot is plotted as a function of the delay time, *t*, as illustrated in Figure 5.3b. Figure 5.3c shows the Fourier transform of the FID to retrieve the spectrum. Each point in the FID is measured ten times for a single FID, as discussed in more detail below, which results in each FID taking 6.4 ms to measure. However, due to relatively low pulse energies and the repetition rate of the laser not being tunable to the cantilever resonance, tens of thousands of averages are used for a single spectrum, which takes between two to five minutes, depending on the sample.

For Equations 5.4 and 5.5 to hold, the AFM amplitude must be linearly proportional to the amount of light absorbed by the sample. Figure 5.3d plots the maximum AFM photodiode voltage as a function of pulse energies, showing a linear response. Although non-linear signals are possible and measurable in higher-order experiments, such as transient absorption and 2D white light spectroscopy, these non-linear signals are three orders of magnitude less than the linear signals. In addition, we do not observe the non-linear thermal expansion effect,[39] which would result in a slope of the FID, but is not present in the FTPT data.

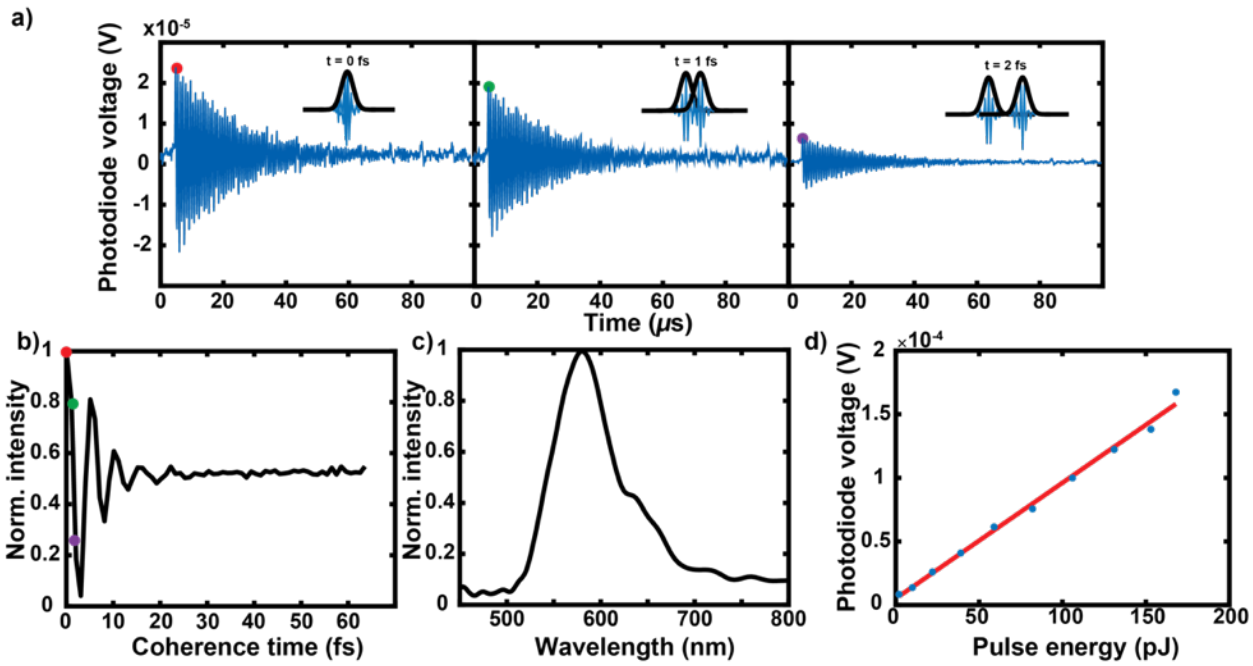

Figure 5.3. Linear response of AFM photothermal detection. (a) shows examples of the magnitude of the AFM oscillations for different delay times, and how the maximum amplitude for each pulse pair: red, green, and purple dots, correspond to the respective points in the FID of TIPS-Pn (b). The FID is then Fourier transformed to obtain the absorption spectrum (c). (d) demonstrates that the AFM photodiode voltage is linear with the intensity of the light.

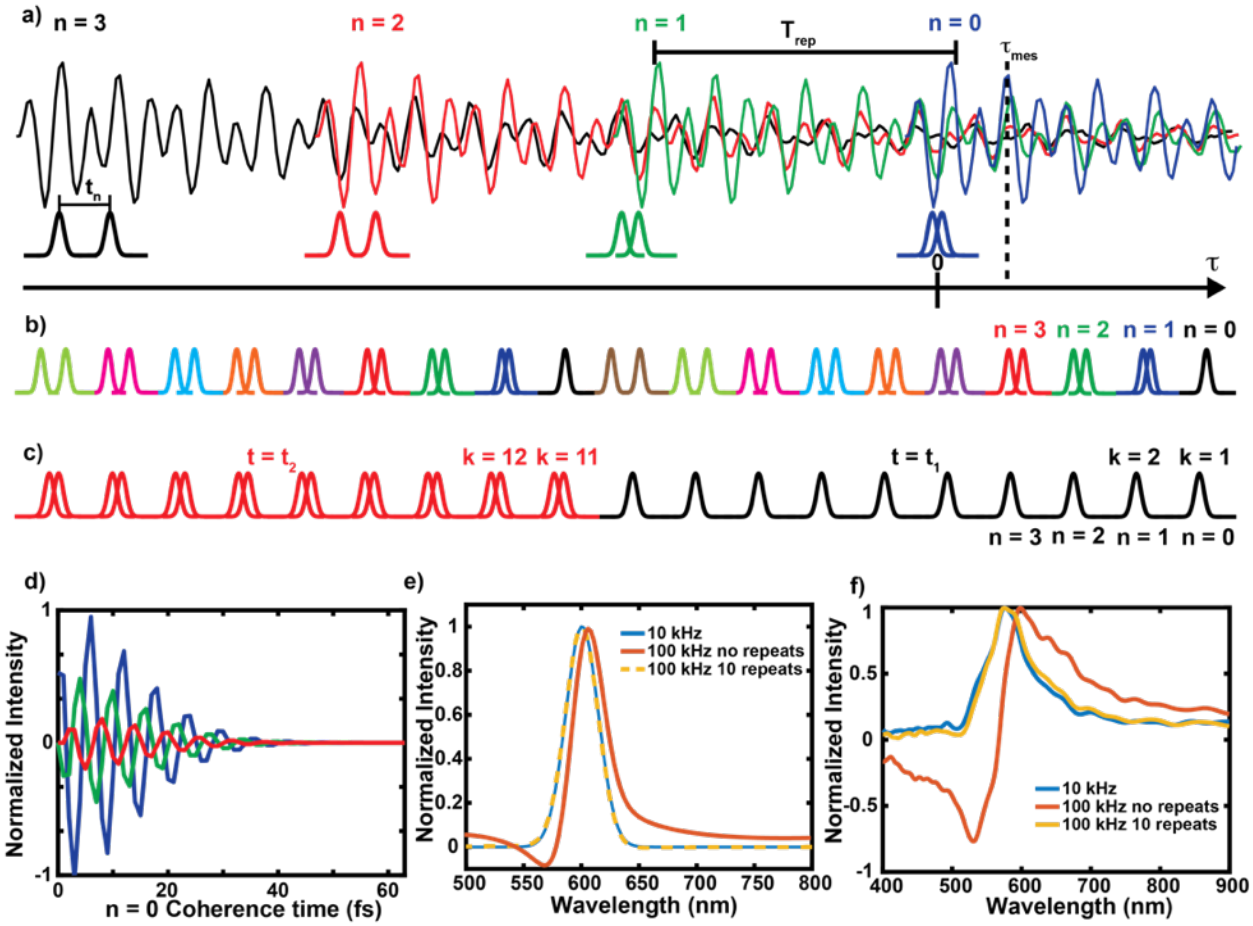

Figure 5.4. Simulation and experiments of AFM interference on FTPT measurements. (a) demonstrates the AFM cantilever oscillations originating from four different pulse pairs, n = 0-3, with corresponding delay times, t_n. The time between the pulses is shown as T_{rep}, and the time the AFM oscillation is measured is τ_{mes}. The pulse sequences are considered, the first (b) has a different delay time for every pulse pair. The second pulse sequence (c) repeats each delay time for ten pulses, so that pulses k = 1-10 have $t = t_1$, and pulses k = 11-20 have $t = t_2$. The contribution to the time-domain signal, $S(t_0)$, from pulse pairs n = 0-2 are shown in (d), with blue, green, and red corresponding to pulse pairs n = 0, 1, and 2 respectively. The simulation (e) and experiment on TIPS-Pn (f) for pulse sequence (b) at a repetition rate of 10 kHz and a repetition rate of 100 kHz are plotted in blue and orange, respectively. The simulation (e) and experiment (f) for pulse sequence (c) at a repetition rate of 100 kHz is plotted in yellow.

5.4.1 Effect of laser repetition rate on AFM response

As mentioned above, the AFM cantilever used in these experiments takes approximately 60 µs to return to rest. At a repetition rate of 100 kHz, the time between laser pulses is 10 µs. Thus, the AFM deflection is caused not only by the immediately preceding pair of pulses, but also the

prior pairs of pulses, each to a lesser degree. In this section, we show the effects of this fact and a means for minimizing its deleterious effects.

Figure 5.4a illustrates the issue by plotting the oscillations of the AFM cantilever for four consecutive pulse pairs, n = 0-3. For a FTPT measurement, there is a fixed time that is interrogated every 10 μs, or once every new pulse pair. This is referred to as the measurement time, τ_{mes}, and is shown as the dashed black line in Figure 5.4a. The first pulse pair, n = 0, is shown in blue. The blue pulse pair, t_0, contributes a discrete amplitude to the AFM oscillations at τ_{mes} that is dependent on the signal, $S(t_0)$, the time constant for the AFM oscillations decaying, τ_{AFM}, and the mechanical resonances of the AFM cantilever, ω_m. The contribution to the time-domain signal is shown in Figure 5.4d. The pulse pair in green, n = 1, also contributes a discrete amplitude to the AFM oscillations at τ_{mes}, which is dependent on $S(t_1)$. For a given value of $S(t_n)$, the contribution from n = 1 is less than the contribution at n = 0 because n = 1 is farther away in time from τ_{mes}, so the AFM response created by n = 1 will have decayed a greater amount. The effect of the AFM oscillations decaying is even more pronounced for pulses farther removed from τ_{mes}.

We can express the measured signal as the following:

$$S_{tot}(t) = \sum_k \sum_n e^{-\frac{\tau_{mes}+nT_{rep}}{\tau_{AFM}}} e^{i\omega_m(\tau_{mes}+nT_{rep})} \cdot S(t_{k+n}) \tag{5.6}$$

where k is the index for the number of times each delay time is repeated, n is the number of pulses before τ_{mes}, as illustrated in Figure 5.4, and T_{rep} is the time between laser pulses. Using this expression, we simulated the FTPT measurement for three different conditions. Situation one is when $T_{rep} = 100$ μs (10 kHz repetition rate) and k = 1 so that T_{rep} is longer than the AFM oscillations, and so the AFM only reads out the thermal response of the immediately preceding pair of pulses. Situation two is when $T_{rep} = 10$ μs (100 kHz), k=1, which is illustrated by the pulse sequence in Figure 5.4b, where multiple pulses contribute to the AFM readout. Situation three is

when $T_{rep} = 10$ μs (100 kHz), k=10, which is illustrated by the pulse sequence in Figure 5.4c. In situation three, only pulse pairs with two different delay times (Figure 5.4c black and red) will contribute to signal at a given τ_{mes}. For the simulations, we used a Gaussian distribution of frequencies centered at 600 nm with a width of 40 nm. The inverse Fourier transform was computed to obtain the time-domain response.

The simulations of situations one, two, and three are plotted in Figure 5.4e in blue, orange, and yellow respectively. The simulation of situation one results in the same Gaussian distribution that was input into the simulation, as there is no interference in situation one. The simulation of situation two illustrates that at 100 kHz, the AFM cantilever does not have time to return to equilibrium before the next pulse pair. As a result, the temperature rise from prior pulse pairs contributes to the signal with an intensity and phase set by the oscillation frequency of the AFM ringdown and the repetition rate of the laser. The multiple signals interfere, and for situation two, where the delay time for every pulse pair is different, this results in a distorted spectrum. For situation three, where all the interfering AFM oscillations originate from only two delay times, the simulated spectrum almost perfectly recreates the spectrum for situation one, where there was no interference.

The three simulated situations were also repeated experimentally, shown in Figure 5.4f. Just as shown in the simulation, the experiments at 10 kHz and 100 kHz with repeating delay times show no distortion (Figure 5.4f, blue and yellow respectively), but the experiment at 100 kHz with no repeating delay times does show a distorted spectrum (Figure 5.4f orange).

An alternative way to address the complication of interfering AFM oscillations is to reduce the laser repetition rate, as we demonstrated in the simulation and experiment (Figure 5.4d,e blue). However, it is preferable to operate at the maximum repetition rate of the pulse shaper, which is

100-200 kHz, in order to decrease the amount of time needed to average. In what follows, we use situation three, a repetition rate of 100 kHz and delay times repeated for ten consecutive laser shots, for all the reported spectra.

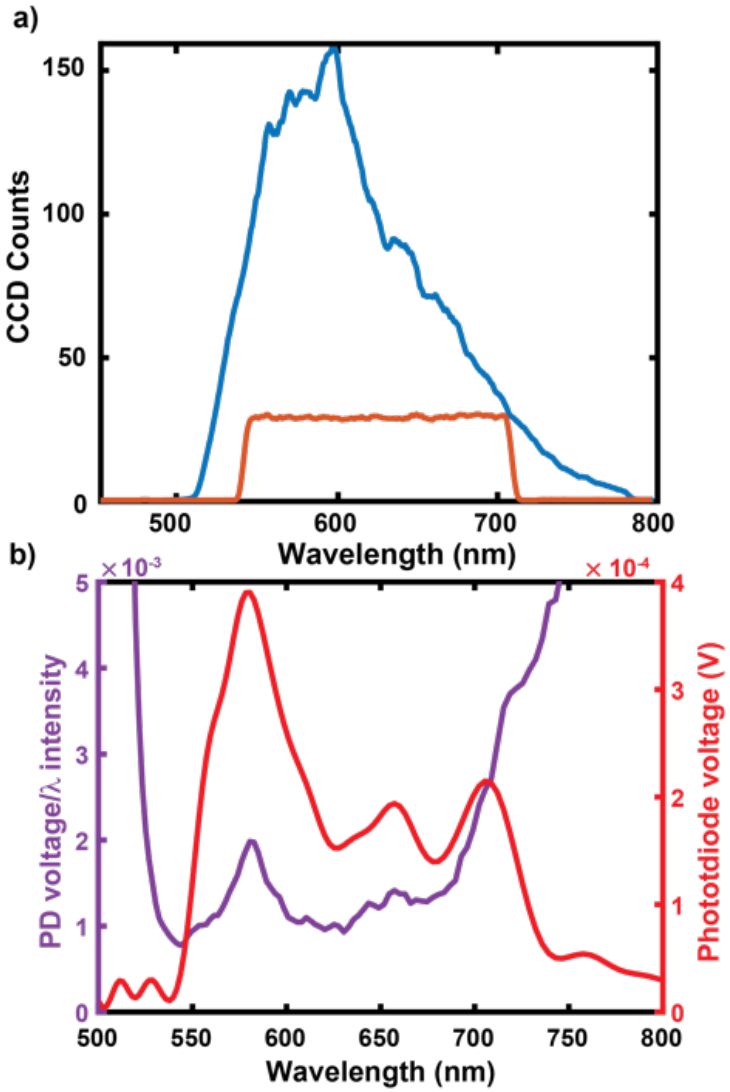

Figure 5.5. Pulse-shaping to flatten the laser spectrum. The spectrum of the laser pulse (a) is shown in blue. The AOM pulse shaper is used to modify the amplitude of the spectrum at each wavelength to create a square laser spectrum, shown in orange. FTPT spectra (b) on a TIPS-Pn microcrystal were measured using the full laser pulse, and then normalized for the intensity of the light at each wavelength (purple), and with a square laser spectrum (red).

5.4.2 FTPT of TIPS-Pn using a square spectral bandwidth for auto-normalization

In absorption spectroscopy, the optical density is typically reported by measuring the spectrum with (foreground) and without (background) the sample and dividing. That process deconvolutes the spectral variations in the intensity of the light source from the molecular information. Making an analogous background measurement with photothermal AFM is more difficult, because removing the sample eliminates any signal; a control sample is needed to create an expansion with a known thermal response. Moreover, it is technically difficult to exchange samples on an AFM while maintaining the precise alignment of the laser and the AFM probe. Indeed, in Figures 5.2 and 5.3 above, we did not present optical density and so the spectra were strongly modulated by the spectrum of the laser pulse.

Pulse shaping provides an alternative method. The pulse shaper is used to modify the amplitude of the laser spectrum such that the laser spectrum has the same intensity at every wavelength within a defined window and is zero for all other wavelengths, creating a flat spectrum, such as the square spectrum shown in Figure 5.5a (orange), created by shaping the laser pulse spectrum.

To illustrate the improvement of using a flat spectrum versus the full laser spectrum, Figure 5.5b in purple shows the FTPT spectrum on a TIPS-Pn microcrystal taken with the full laser spectrum, and then dividing by the relative laser intensity at each wavelength (Figure 5.5a, blue). There are two peaks at 580 and 650 nm, but the spectrum at the edges of the laser spectrum is not physical, due to division by small numbers. Also shown in Figure 5.5b (red) is the FTPT spectrum from the same spot, but with a square laser spectrum so that no normalization is required. With the square laser spectrum, the same two peaks at 580 and 650 nm are evident, as well as an additional peak at 700 nm that is not discernable in the normalized FTPT spectrum. The data presented in the remainder of the manuscript are collected using a square pulse spectrum.

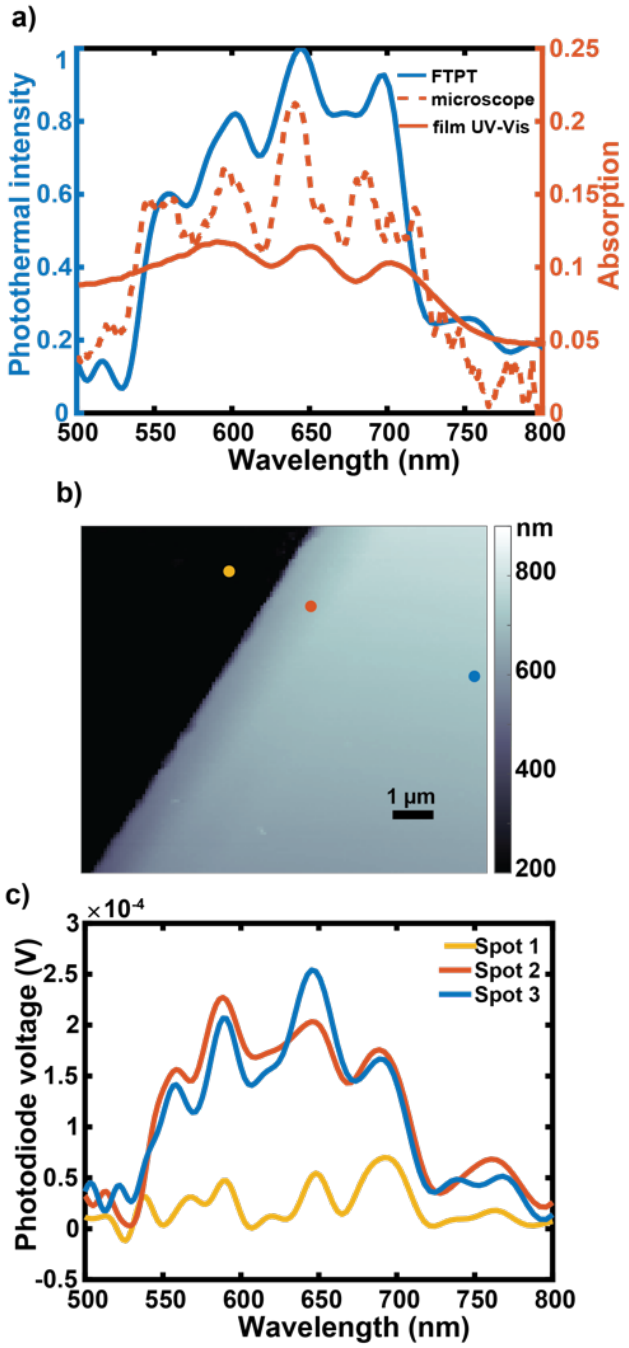

Figure 5.6. TIPS-Pn spectra measured via FTPT. (a) The bulk spectrum of TIPS-Pn (solid orange) agrees well with the optically detected microscope spectrum (dashed orange) and FTPT spectrum (blue). (b) shows the topography at the edge of a TIPS-Pn microcrystal. FTPT spectra were measured at three different spots (c) corresponding to the locations of the same colored dots in (b).

5.4.3 TIPS-Pn spectrum via FTPT

The spectroscopic capabilities of FTPT are demonstrated on TIPS-Pn microcrystals (Figure 5.6). In Figure 5.6a is plotted a bulk absorption spectrum of TIPS-Pn microcrystals (orange solid), an optically detected microscope spectrum from a TIPS-Pn microcrystal (orange dashed), and an FTPT spectrum from the same location as the optically detected spectrum (blue). The bulk absorption spectrum resembles those previously reported by our research group and in the literature.[6] The main spectroscopic feature is a vibronic progression, with three peaks each centered at 700, 650, and 590 nm. There is also broad continuous absorption at energies above the vibronic progression. All three spectra in Figure 5.6a have the expected three vibronic peaks at the same wavelengths. The intensity of the vibronic peaks relative to the continuous absorption is greater in the microscope and FTPT spectra versus the bulk absorption spectrum. This is likely due to the bulk spectrum being measured with unpolarized light, whereas the microscope and FTPT spectra were measured with linearly polarized light. We note that in the microcrystals, the TIPS-Pn molecules are oriented such that the transition dipole of the $S_{1,n}$ states are aligned roughly along the short axis of the crystal.[6]

Figure 5.6c shows the FTPT spectra at three different spots on a TIPS-Pn microcrystal (Figure 5.6b). Spot one (yellow) is off the crystal, and only small amounts of TIPS-Pn are measured, hardly above the noise of the measurement. Spots two and three are from near the edge and the center of the crystal respectively. We note that the relative intensity of the 650 nm peak at the edge of the crystal is much smaller than the center of the crystal. We have previously reported that the structure of TIPS-Pn at the edges of crystals have defects. We tentatively assign this change in intensity to the effects of those defects.[6,40]

5.4.4 Simultaneous photothermal and topographical imaging

Mn-phthalocyanine (MnPc) islands were used to test the spatial resolution of the photothermal microscope. When deposited as described in the methods, MnPc forms islands with diameters on the order of hundreds of nanometers, and heights of 70-120 nm, as shown in the topography image in Figure 5.7a. The islands formed are pancake in shape, with the diameter exceeding the height of the islands. The photothermal absorption from the MnPc film (Figure 5.7b) was collected simultaneously with the topography. The step size for the images in Figure 5.7 is 20 nm. As described in the experimental, the photothermal image shows the AFM deflection for an unmodified laser pulse. It is not feasible to measure a spectrum at every pixel, as each spectrum takes 2-5 minutes and there are over 65,000 pixels in a typical image. However, it is possible to use the pulse shaper to window the pulse to a specific spectral region and measure the photothermal expansion for that window (Figure 5.S1). The photothermal image shows absorption from all three islands, even though the diameter of the islands can be as small as 200 nm, which is near the diffraction limit of light. To determine the spatial resolution of the photothermal imaging, we have plotted a cross-section through the topography and photothermal images (Figure 5.7c), and determined the full-width at 10% of the maximum for the topography, W_{Top}, and the full-width at 10% of the maximum for the photothermal absorption, W_{PT}, and the difference between the two widths was calculated.[26] The average difference in the widths for 40 different cross-sections, 20 vertical and 20 horizontal, was 49 ± 36 nm. Additional cross-sections are shown in Figure 5.S2. The diffraction limit of the shortest wavelength of light in our laser spectrum, 550 nm, is 200 nm. Thus, the spatial resolution of AFM detected photothermal image is significantly below the diffraction limit.

Figure 5.7d. shows the normalized photothermal absorption divided by the topography for all pixels with at least 25% of the maximum photothermal intensity. The absorption relative to the

height of the islands is larger on one side of the islands, regardless of the direction the AFM was scanned, indicating this was not an artifact due to poor tracking of the AFM tip. A possible physical origin for the increased relative absorption on one side of the islands is that the crystals grow from one side as the solvent evaporates. We have previously measured crystallin disorder that depends on crystal growth.[40]

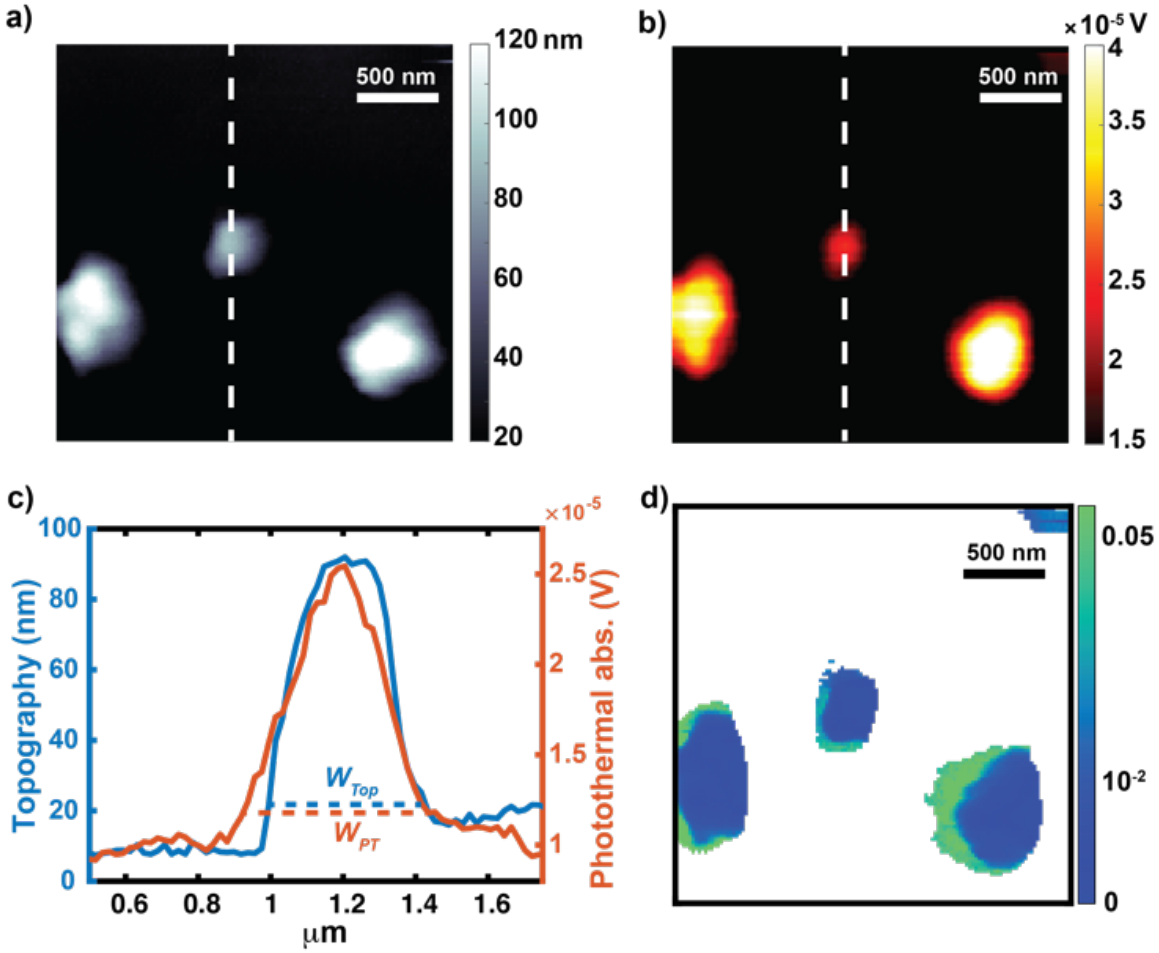

Figure 5.7. Photothermal imaging of MnPc islands. The topography and photothermal absorption images of MnPc islands are shown in (a) and (b) respectively. Cross-sections through the topography and photothermal absorption (c) demonstrate the sub-diffraction limit spatial resolution of AFM detected photothermal microscopy. (d) plots the photothermal absorption divided by the height for all pixels with at least 25% of the maximum photothermal signal, plotted on a log scale.

5.5 Conclusions

Fourier transform photothermal spectroscopy is a time-domain method for measuring spectroscopic information with sub-diffraction limit spatial resolution. Photothermal detection is a well-established method used in frequency domain AFM-IR and visible AFM experiments,[26,41] but operation in the time-domain allows for the use of ultrafast, broadband pulses. Utilizing a pulse shaper also enables pulse sequences that utilize phase cycling, a rotating frame, data collection with flat-intensity pulses, and arbitrary ordering of pulse delays for optimizing data collection to the repetition rate of the laser and the AFM decay time. We generate linear spectra, but the Potma group has performed AFM-detected pump-probe experiments.[42] Pump-probe and 2D optical spectroscopies are both third-order experiments. Thus, it should be possible to extend the FTPT measurements here to multi-dimensional spectroscopy by using the pulse shaper to generate more sophisticated pulse trains.

5.6 Supplementary Information

5.6.1 Further Explanation of Interfering AFM Oscillations.

The signal from the thermal expansion due to a given pulse pair is expressed in equation 1 and is derived in the main text.

$$S(t) \propto I_1 {\mu_{ge}}^2 + I_2 {\mu_{ge}}^2 + I_{12} e^{it(\omega_c - \omega_{ge})} e^{-i\Delta\varphi_{12}} {\mu_{ge}}^2 \tag{5.7}$$

This equation represents the signal electric field, and not the mechanical detection via the AFM photodetector voltage. Although the absorption and expansion from consecutive pulse pairs are independent of one another, the deflection of the AFM cantilever and subsequent oscillations from consecutive pulse pairs are mechanically tied to one another due to the relaxation time of the AFM cantilever being greater than the time between consecutive laser pulses. In the main text, we define an equation to describe the AFM oscillations interference, also shown here in equation 5.7:

$$S_{tot}(t) = \sum_k \sum_n e^{-\frac{\tau_{mes}+nT_{rep}}{\tau_{AFM}}} e^{i\omega_m(\tau_{mes}+nT_{rep})} \cdot S(t_{k+n}) \tag{5.7}$$

where k is the number of times each delay time is repeated, n is the index of the laser pulse pair preceding the laser pulse pair of interest, τ_{mes} is the time in the AFM oscillations that the measurement it made, T_{rep} is the time between laser pulses, τ_{AFM} is the time constant for the AFM oscillations decaying, and ω_m is mechanical resonance of the AFM cantilever. The first exponential term describes the exponential decay of AFM oscillations, and the second exponential term describes the oscillations. The two exponential terms together are an approximation of the AFM cantilever motion.

To better clarify the mathematical formulation of the AFM interference, we give the expressions for the total signal for the two cases measured in the manuscript at repetition rate of 100 kHz.

Case 1: the delay time is changed every laser pulse pair, i.e. k = 1, and we consider the nine previous laser pulse pairs, n = 0…9. The measured signal, S_{tot}, for the pulse with delay time t_1 is

$$S_{tot}(t_1) = e^{-\frac{\tau_{mes}}{\tau_{AFM}}} e^{i\omega_m \tau_{mes}} \cdot S(t_1) + e^{-\frac{\tau_{mes}+T_{rep}}{\tau_{AFM}}} e^{i\omega_m(\tau_{mes}+T_{rep})} \cdot S(t_2)$$
$$+ e^{-\frac{\tau_{mes}+2T_{rep}}{\tau_{AFM}}} e^{i\omega_m(\tau_{mes}+2T_{rep})} \cdot S(t_3) + e^{-\frac{\tau_{mes}+3T_{rep}}{\tau_{AFM}}} e^{i\omega_m(\tau_{mes}+3T_{rep})} \cdot S(t_4)$$
$$+ e^{-\frac{\tau_{mes}+4T_{rep}}{\tau_{AFM}}} e^{i\omega_m(\tau_{mes}+4T_{rep})} \cdot S(t_5) + e^{-\frac{\tau_{mes}+5T_{rep}}{\tau_{AFM}}} e^{i\omega_m(\tau_{mes}+5T_{rep})} \cdot S(t_6)$$
$$+ e^{-\frac{\tau_{mes}+6T_{rep}}{\tau_{AFM}}} e^{i\omega_m(\tau_{mes}+6T_{rep})} \cdot S(t_7) + e^{-\frac{\tau_{mes}+7T_{rep}}{\tau_{AFM}}} e^{i\omega_m(\tau_{mes}+7T_{rep})} \cdot S(t_8)$$
$$+ e^{-\frac{\tau_{mes}+8T_{rep}}{\tau_{AFM}}} e^{i\omega_m(\tau_{mes}+8T_{rep})} \cdot S(t_9) + e^{-\frac{\tau_{mes}+9T_{rep}}{\tau_{AFM}}} e^{i\omega_m(\tau_{mes}+9T_{rep})} \cdot S(t_{10}) \quad (5.8)$$

Each term in the sum contributes less and less to the total value due to the exponential decay term. For this case, each term results from an expansion due to a different delay time.

Case 2 is the situation where the repetition rate is still 100 kHz, and n = 0…9, but each delay time is repeated ten times in a row, i.e. k = 1…10. There are ten n terms for each k, so there are 100 total terms in the sum. To shorten the notation, we define

$$c_n \equiv e^{-\frac{\tau_{mes}+nT_{rep}}{\tau_{AFM}}} e^{i\omega_m(\tau_{mes}+nT_{rep})} \tag{5.9}$$

The ten terms for $k = 1$ for the pulse pair with time delay t_1 for case 2 are:

$$S_1(t_1) = c_0S(t_1) + c_1S(t_1) + c_2S(t_1) + c_3S(t_1) + c_4S(t_1) + c_5S(t_1) + c_6S(t_1) + c_7S(t_1) + c_8S(t_1) + c_9S(t_1) \tag{5.10}$$

The ten terms for $k = 2$ are:

$$S_2(t_1) = c_0S(t_1) + c_1S(t_1) + c_2S(t_1) + c_3S(t_1) + c_4S(t_1) + c_5S(t_1) + c_6S(t_1) + c_7S(t_1) + c_8S(t_1) + c_9S(t_2) \tag{5.11}$$

As the k index increases, there are additional terms that are dependent on delay time t_2, but unlike case 1, t_2 is the only additional delay time that will contribute to the total signal. The final expression for the total signal after considering all k indices and combining like terms is:

$$S_{tot}(t_1) = (10c_0 + 9c_1 + 8c_2 + 7c_3 + 6c_4 + 5c_5 + 4c_6 + 3c_7 + 2c_8 + c_9)S(t_1) + (c_1 + 2c_2 + 3c_3 + 4c_4 + 5c_5 + 6c_6 + 7c_7 + 8c_8 + 9c_9)S(t_2) \tag{5.12}$$

In case 2 only one additional delay time contributes to the measured signal for the delay time of interest, and the contribution from t_1 is 26 times greater than the contribution from t_2.

5.6.2 Photothermal imaging with spectrally windowed pulses

The AOM pulse shaper can be used to window the spectrum of the laser pulse used for imaging to only a portion of the absorption window of the sample. For Figure 5.S1, the windows 675-710 nm and 635-670 nm were used to image the first and second vibronic peaks of the TIPS-Pn respectively. By comparing to the total photothermal absorption image, it is clear that the two windowed images have a lower signal to noise, which would be expected when the total amount of light being absorbed is less in both windowed cases.

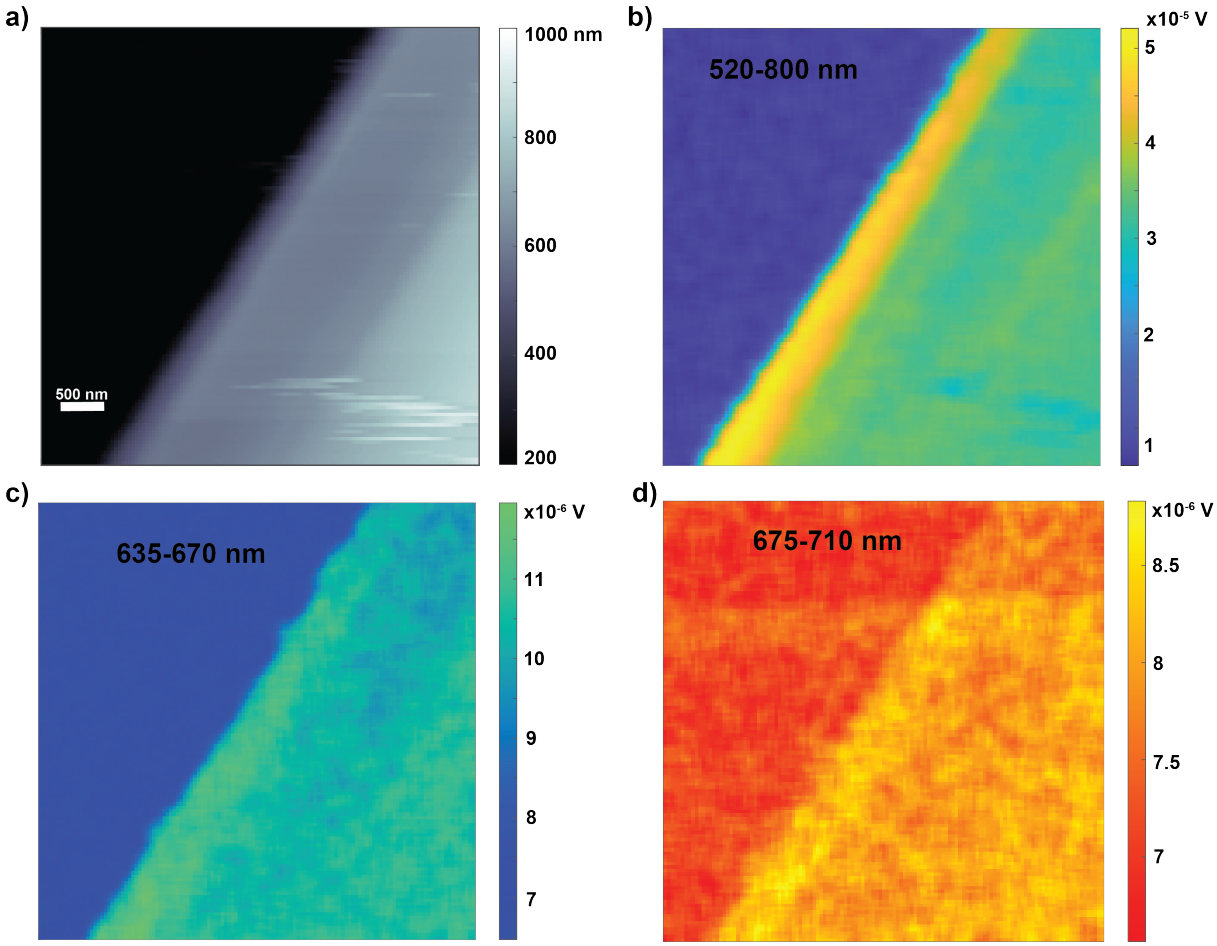

Figure 5.S1. a) shows the topography image of the edge of a TIPS-Pn microcrystal. b) shows the total photothermal absorption at the edge of the crystal, whereas c) and d) show the photothermal absorption images for only portions of the white light spectrum that correspond to the second and first vibronic peaks in the TIPS-Pn crystal spectrum respectively.

5.6.3 Imaging cross-sections through Mn-phthalocyanine nano-islands

We plot additional cross-sections through the topography and photothermal images presented in the main text, Figure 5.7. A vertical and horizontal slice is plotted through each of the three nano-islands.

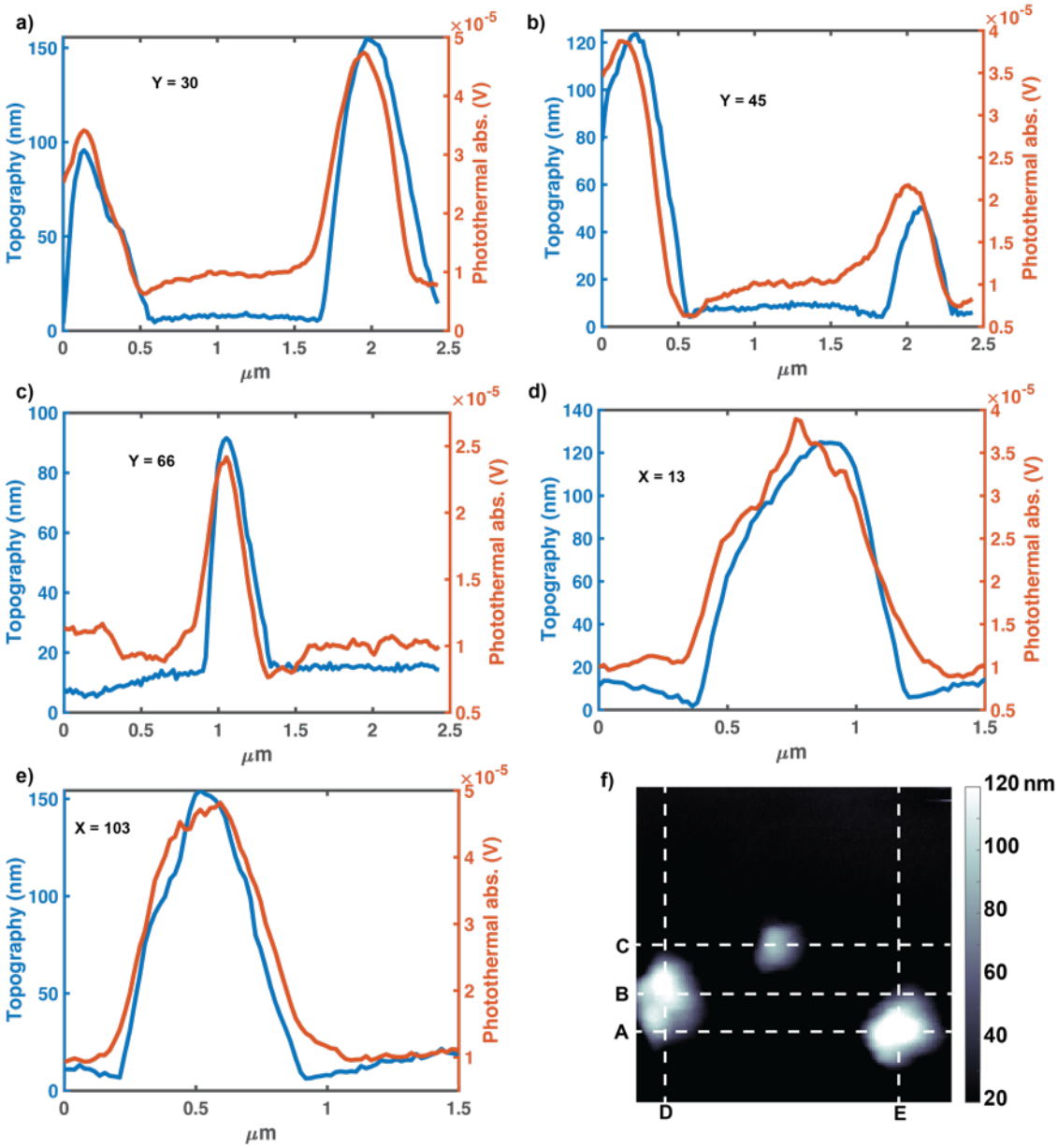

Figure 5.S2. a-e) show cross-sections through the topography (blue) and photothermal absorption (orange) for five additional slices, corresponding to the dashed white lines in f).

5.7 References

(1) Major, J. D. Grain Boundaries in CdTe Thin Film Solar Cells: A Review. *Semicond. Sci. Technol.* **2016**, *31* (9), 093001.
(2) Seager, C. H. Grain Boundaries in Polycrystalline Silicon. *Annu. Rev. Mater. Res.* **1985**, *15* (1), 271–302.
(3) Zong, Y.; Zhou, Y.; Zhang, Y.; Li, Z.; Zhang, L.; Ju, M.-G.; Chen, M.; Pang, S.; Zeng, X. C.; Padture, N. P. Continuous Grain-Boundary Functionalization for High-Efficiency Perovskite Solar Cells with Exceptional Stability. *Chem* **2018**, *4* (6), 1404–1415.
(4) Xie, T.; Jing, C.; Long, Y.-T. Single Plasmonic Nanoparticles as Ultrasensitive Sensors. *Analyst* **2017**, *142* (3), 409–420.
(5) Sambur, J. B.; Chen, P. Approaches to Single-Nanoparticle Catalysis. *Annu. Rev. Phys. Chem.* **2014**, *65* (1), 395–422.
(6) Jones, A. C.; Kearns, N. M.; Ho, J.-J.; Flach, J. T.; Zanni, M. T. Impact of Non-Equilibrium Molecular Packings on Singlet Fission in Microcrystals Observed Using 2D White-Light Microscopy. *Nat. Chem.* **2019**, 1–8.
(7) Hickey, C. L.; Grumstrup, E. M. Direct Correlation of Charge Carrier Transport to Local Crystal Quality in Lead Halide Perovskites. *Nano Lett.* **2020**, *20* (7), 5050–5056.
(8) Bender, J. A.; Raulerson, E. K.; Li, X.; Goldzak, T.; Xia, P.; Van Voorhis, T.; Tang, M. L.; Roberts, S. T. Surface States Mediate Triplet Energy Transfer in Nanocrystal–Acene Composite Systems. *J. Am. Chem. Soc.* **2018**, *140* (24), 7543–7553.
(9) Tavakoli, M. M.; Bi, D.; Pan, L.; Hagfeldt, A.; Zakeeruddin, S. M.; Grätzel, M. Adamantanes Enhance the Photovoltaic Performance and Operational Stability of Perovskite Solar Cells by Effective Mitigation of Interfacial Defect States. *Adv. Energy Mater.* **2018**, *8* (19), 1800275.
(10) Chen, W.; Wang, Y.; Pang, G.; Koh, C. W.; Djurišić, A. B.; Wu, Y.; Tu, B.; Liu, F.; Chen, R.; Woo, H. Y.; Guo, X.; He, Z. Conjugated Polymer–Assisted Grain Boundary Passivation for Efficient Inverted Planar Perovskite Solar Cells. *Adv. Funct. Mater.* **2019**, *29* (27), 1808855.
(11) Jiang, Y.; Wang, C.; Rogers, C. R.; Kodaimati, M. S.; Weiss, E. A. Regio- and Diastereoselective Intermolecular [2+2] Cycloadditions Photocatalysed by Quantum Dots. *Nat. Chem.* **2019**, *11* (11), 1034–1040.
(12) Li, Z.; Ji, S.; Liu, Y.; Cao, X.; Tian, S.; Chen, Y.; Niu, Z.; Li, Y. Well-Defined Materials for Heterogeneous Catalysis: From Nanoparticles to Isolated Single-Atom Sites. *Chem. Rev.* **2020**, *120* (2), 623–682.
(13) Rust, M. J.; Bates, M.; Zhuang, X. Sub-Diffraction-Limit Imaging by Stochastic Optical Reconstruction Microscopy (STORM). *Nat. Methods* **2006**, *3* (10), 793–796.
(14) Hell, S. W. Far-Field Optical Nanoscopy. *Science* **2007**, *316* (5828), 1153–1158.
(15) Wang, P.; Slipchenko, M. N.; Mitchell, J.; Yang, C.; Potma, E. O.; Xu, X.; Cheng, J.-X. Far-Field Imaging of Non-Fluorescent Species with Subdiffraction Resolution. *Nat. Photonics* **2013**, *7* (6), 449–453.
(16) Hofmann, M.; Eggeling, C.; Jakobs, S.; Hell, S. W. Breaking the Diffraction Barrier in Fluorescence Microscopy at Low Light Intensities by Using Reversibly Photoswitchable Proteins. *Proc. Natl. Acad. Sci. U.S.A.* **2005**, *102* (49), 17565–17569.
(17) Binnig, G.; Rohrer, H. Scanning Tunneling Microscopy. *Surf. Sci.* **1983**, *126* (1), 236–244.

(18) Giessibl, F. J. Advances in Atomic Force Microscopy. *Rev. Mod. Phys.* **2003**, *75* (3), 949–983.
(19) Kravtsov, V.; Ulbricht, R.; Atkin, J. M.; Raschke, M. B. Plasmonic Nanofocused Four-Wave Mixing for Femtosecond near-Field Imaging. *Nat. Nanotechnol.* **2016**, *11* (5), 459–464.
(20) Centrone, A. Infrared Imaging and Spectroscopy Beyond the Diffraction Limit. *Annu. Rev. Anal. Chem.* **2015**, *8* (1), 101–126.
(21) Knoll, B.; Keilmann, F. Near-Field Probing of Vibrational Absorption for Chemical Microscopy. *Nature* **1999**, *399* (6732), 134–137.
(22) Dazzi, A.; Prazeres, R.; Glotin, F.; Ortega, J. M. Local Infrared Microspectroscopy with Subwavelength Spatial Resolution with an Atomic Force Microscope Tip Used as a Photothermal Sensor. *Opt. Lett.* **2005**, *30* (18), 2388.
(23) Dazzi, A.; Glotin, F.; Carminati, R. Theory of Infrared Nanospectroscopy by Photothermal Induced Resonance. *J. Appl. Phys.* **2010**, *107* (12), 124519.
(24) Lahiri, B.; Holland, G.; Centrone, A. Chemical Imaging Beyond the Diffraction Limit: Experimental Validation of the PTIR Technique. *Small* **2013**, *9* (3), 439–445.
(25) Chae, J.; An, S.; Ramer, G.; Stavila, V.; Holland, G.; Yoon, Y.; Talin, A. A.; Allendorf, M.; Aksyuk, V. A.; Centrone, A. Nanophotonic Atomic Force Microscope Transducers Enable Chemical Composition and Thermal Conductivity Measurements at the Nanoscale. *Nano Lett.* **2017**, *17* (9), 5587–5594.
(26) Katzenmeyer, A. M.; Holland, G.; Kjoller, K.; Centrone, A. Absorption Spectroscopy and Imaging from the Visible through Mid-Infrared with 20 Nm Resolution. *Anal. Chem.* **2015**, *87* (6), 3154–3159.
(27) Dong, R.; Fang, Y.; Chae, J.; Dai, J.; Xiao, Z.; Dong, Q.; Yuan, Y.; Centrone, A.; Zeng, X. C.; Huang, J. High-Gain and Low-Driving-Voltage Photodetectors Based on Organolead Triiodide Perovskites. *Adv. Mater.* **2015**, *27* (11), 1912–1918.
(28) Katzenmeyer, A. M.; Canivet, J.; Holland, G.; Farrusseng, D.; Centrone, A. Assessing Chemical Heterogeneity at the Nanoscale in Mixed-Ligand Metal–Organic Frameworks with the PTIR Technique. *Angew. Chem.* **2014**, *53* (11), 2852–2856.
(29) Kennedy, E.; Al-Majmaie, R.; Al-Rubeai, M.; Zerulla, D.; Rice, J. H. Quantifying Nanoscale Biochemical Heterogeneity in Human Epithelial Cancer Cells Using Combined AFM and PTIR Absorption Nanoimaging. *J. Biophotonics* **2015**, *8* (1–2), 133–141.
(30) Schwartz, J. J.; Jakob, D. S.; Centrone, A. A Guide to Nanoscale IR Spectroscopy: Resonance Enhanced Transduction in Contact and Tapping Mode AFM-IR. *Chem. Soc. Rev.* **2022**, *51* (13), 5248-5267
(31) Kurouski, D.; Dazzi, A.; Zenobi, R.; Centrone, A. Infrared and Raman Chemical Imaging and Spectroscopy at the Nanoscale. *Chem. Soc. Rev.* **2020**, *49* (11), 3315–3347.
(32) Huth, F.; Govyadinov, A.; Amarie, S.; Nuansing, W.; Keilmann, F.; Hillenbrand, R. Nano-FTIR Absorption Spectroscopy of Molecular Fingerprints at 20 Nm Spatial Resolution. *Nano Lett.* **2012**, *12* (8), 3973–3978.
(33) Frogley, M. D.; Lekkas, I.; Kelley, C. S.; Cinque, G. Performances for Broadband Synchrotron Photothermal Infrared Nano-Spectroscopy at Diamond Light Source. *Infrared Phys. Technol.* **2020**, *105*, 103238.
(34) Chan, K. L. A.; Lekkas, I.; Frogley, M. D.; Cinque, G.; Altharawi, A.; Bello, G.; Dailey, L. A. Synchrotron Photothermal Infrared Nanospectroscopy of Drug-Induced Phospholipidosis in Macrophages. *Anal. Chem.* **2020**, *92* (12), 8097–8107.

(35) Jones, A. C.; Kearns, N. M.; Bohlmann Kunz, M.; Flach, J. T.; Zanni, M. T. Multidimensional Spectroscopy on the Microscale: Development of a Multimodal Imaging System Incorporating 2D White-Light Spectroscopy, Broadband Transient Absorption, and Atomic Force Microscopy. *J. Phys. Chem. A* **2019**, *123* (50), 10824–10836.
(36) Jones, A. C.; Bohlmann Kunz, M.; Tigges-Green, I.; Zanni, M. T. Dual Spectral Phase and Diffraction Angle Compensation of a Broadband AOM 4-f Pulse-Shaper for Ultrafast Spectroscopy. *Opt. Express,* **2019**, *27* (26), 37236–37247.
(37) Hamm, P.; Zanni, M. T. *Concepts and Methods of 2d Infrared Spectroscopy*; Cambridge University Pres: Cambridge ; New York, 2011.
(38) Shim, S.-H.; Zanni, M. T. How to Turn Your Pump–Probe Instrument into a Multidimensional Spectrometer: 2D IR and Vis Spectroscopiesvia Pulse Shaping. *Phys. Chem. Chem. Phys.* **2009**, *11* (5), 748–761.
(39) Park, B.; Lee, S.; Kwon, J.; Kim, W.; Jung, S.; Kim, C. Dual-Pulse Photoactivated Atomic Force Microscopy. *Sci. Rep.* **2021**, *11* (1), 17097.
(40) Armstrong, Z. T.; Kunz, M. B.; Jones, A. C.; Zanni, M. T. Thermal Annealing of Singlet Fission Microcrystals Reveals the Benefits of Charge Transfer Couplings and Slip-Stacked Packing. *J. Phys. Chem. C* **2020**, *124* (28), 15123–15131.
(41) Dazzi, A.; Prater, C. B. AFM-IR: Technology and Applications in Nanoscale Infrared Spectroscopy and Chemical Imaging. *Chem. Rev.* **2017**, *117* (7), 5146–5173.
(42) Kim, B.; Khan, R. M.; Fast, A.; Fishman, D. A.; Potma, E. O. Nanoscale Excitation Dynamics of Carbon Nanotubes Probed with Photoinduced Force Microscopy. *J. Phys. Chem. C* **2020**, *124* (21), 11694–11700.

Appendix

A. List of Publications

[8] **Bohlmann Kunz M**, Podorova Y, Armstrong ZT, Zanni MT, **2022.** "Time-domain photothermal AFM spectroscopy via femtosecond pulse shaping." *Anal. Chem.*

[7] **Bohlmann Kunz M**, Flach JT, Jones AC, Kim H-S, Hagfeldt A, Zanni MT, **2021.** "2D White-Light Spectroscopy: Application to Lead-Halide Perovskites with Mixed Cations." *Emerging Trends in Chemical Applications of Lasers*

[6] Armstrong ZT, **Bohlmann Kunz M**, Zanni MT. **2021**. "Ultrafast Fluctuations in PM6 Domains of Binary and Ternary Organic Photovoltaic Thin Films Probed with Two-Dimensional White-Light Spectroscopy." *J.Phys.Chem.Lett.*

[5] Armstrong ZT, **Bohlmann Kunz M**, Jones AC, Zanni MT. **2020.** "Thermal Annealing of Singlet Fission Microcrystals Reveals the Benefits of Charge Transfer Couplings and Slip-Stacked Packing." *J. Phys. Chem. C*

[4] Petti MK, Ostrander JS, Birdsall ER, **Bohlmann Kunz M**, Armstrong ZT, Alperstein AM, Zanni MT. **2020.** "A Proposed Method to Obtain Surface Specificity with Pump-Probe and 2D Spectroscopies." *J. Phys. Chem. A*

[3] Jones AC, **Bohlmann Kunz M**, Tigges-Green I, and Zanni MT. **2019**. "Dual spectral phase and diffraction angle compensation of a broadband AOM 4-f pulse shaper for ultrafast spectroscopy." *Opt. Express*

[2] Jones AC, Kearns NM, **Bohlmann Kunz M**, Flach JT, and Zanni MT. **2019**. "Multidimensional Spectroscopy on the Microscale: Development of a Multimodal Imaging System Incorporating 2D White-Light Spectroscopy, Broadband Transient Absorption, and Atomic Force Microscopy." *J. Phys. Chem. A*

[1] Kearns NM, Jones AC, **Bohlmann Kunz M**, Allen RT, Flach JT, and Zanni MT. **2019.** "Two-Dimensional White-Light Spectroscopy Using Supercontinuum from an All-Normal Dispersion Photonic Crystal Fiber Pumped by a 70 MHz Yb Fiber Oscillator." *J. Phys. Chem. A.*

B. Pulse shaper alignment tips

The first step for ensuring maximum shaper output is to maximize the white-light generation and confirming the white-light collimation. Here is a list of steps with pictures for different reference points.

B.1 White-light generation alignment

1. Check that the fundamental NIR beam is passing through the center of the irises before the pump-probe beam splitter, and the irises after the beam splitter.
2. Place an 800 nm short-pass filter after the white-light collimating parabolic, and a power meter after the short-pass filter.
3. Rotate the YAG crystal to a new position on the crystal.
4. Adjust the last iris before the lens to maximize the white-light power, then adjust the waveplate in the variable attenuator to maximize the white-light power. Rotate between adjusting these two parameters until the highest white-light power that is stable is achieved.
5. Remove the power and short-pass filter, and insert a flat mirror to direct the beam all the way down the table. SAFETY RISK! Make sure to alert all other people in the lab that there is an open beam extending past the table. Always wear safety glasses for the 1040 nm fundamental when there is a chance of stray reflections.
6. Ideally with two people, have one person monitor the beam mode of the white-light, while the other person adjusts the position of the parabolic. In Figure B1, there are two pictures, the first shows a poorly collimated beam, the second shows a well collimated beam.

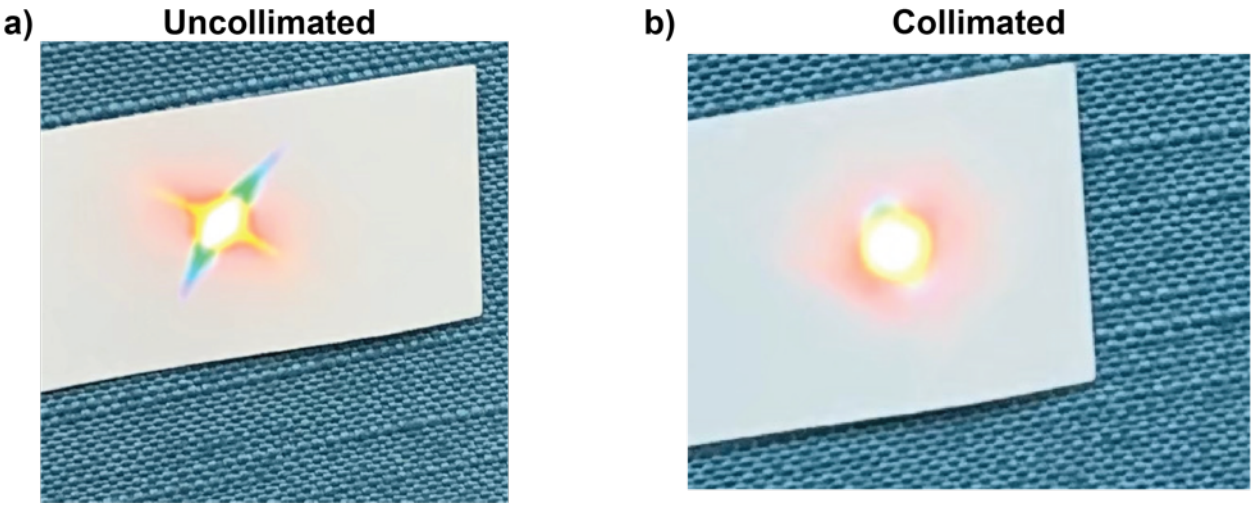

Figure B1. a) uncollimated beam after white-light generation, b) collimated beam after white-light generation.

7. Once the white-light has been collimated, remove the inserted flat mirror, and align the white-light through the chirped mirrors and periscope to the last mirror before the pulse shaper.
8. With a card blocking the beam, adjust the focus of the collimating parabolic so that the white-light goes through a focus right before entering the pulse shaper.

Once the white-light has been maximized and collimated, the shaper alignment can be adjusted.

B.2 Routine pulse shaper alignment

For a full alignment guide for building a pulse from scratch, I would direct the read to the dissertation of Nick Kearns, a former Zanni Group member. Here I will describe the routine process for aligning the quartz AOM pulse shaper that I used for the research in this dissertation.

1. Align the white-light through the two irises leading into the shaper.
2. Place a card in front of the second grating, blocking both the zeroth-order and first-order diffractions.
3. Using the last mirror going into the shaper after the two irises but before the first grating, adjust the horizontal position of the white-light to maximize the first-order diffraction (by

eye). Adjust the card blocking the second grating so that only the zeroth-order diffraction is blocked.

4. Place an iris after the second grating but before the first mirror after the grating. The first mirror may need to be removed to fit the iris. The iris should be at the same height as the two irises at the entrance to the shaper.
5. Using the last mirror going into the shaper, adjust the vertical height of the beam so that it passes through the center of the inserted iris. Remove the iris and replace the mirror if it was removed.
6. To ensure maximum efficiency, place a power meter immediately after the shaper. Using the last mirror before entering the shaper, adjust the horizontal position to maximize the power. Monitor the position of the beam on the power meter to ensure that the beam is not walked off the meter and that only the first-order diffraction is hitting the meter.
7. With the power meter still in place, final adjustment can be made to the iris immediately preceding the white-light generation to maximize the power output through the shaper.

Steps 4-7 are optional for day-to-day alignment of the shaper but can be done when the shaper output has dropped below the expected magnitude. The maximum achieved shaper output has been 70 μW, but 40 μW is a standard output for the shaper as of May 2022.

C. AOM calibration procedure

To properly shape a pulse with the AOM pulse shaper, the correlation between the frequency of light and the position on the AOM must be known. This calibration process is done with two measurements and a Matlab script. The first measurement deflects a small window of light from known AWG pixels. The reference measurement correlates the AWG pixels from the reference to the measured wavelength with the spectrometer. The calibration measurement then

measures the wavelength for peaks that are evenly spaced with respect to the AWG pixels. Since the wavelength for the reference peak is known, the wavelengths of the remaining peaks from the calibration can be mapped to the AWG pixels. The wavelength of light is converted to frequency, and the frequency of light across the AWG as a function of the pixel is fit with a second order polynomial. The process is described in a step-by-step guide.

1. Align the deflected light from the pulse shaper into the spectrometer.
2. Apply a 2-frame mask sequence called “Pump-probe single.” The first mask has zero amplitude at all AWG pixels. The second mask has an amplitude of one for a user defined width of AWG pixels centered at a user defined pixel. Typical width and center pixel values are 10 and 1200 respectively. An example of the single-peak mask is shown in Figure C1. Measure both frames in the spectrometer and subtract the zero-amplitude frame from the single-peak frame. This can be done using the two-frame phase-cycle setting in the camera program for the setup used in this dissertation. This measurement is referred to as the “reference.”

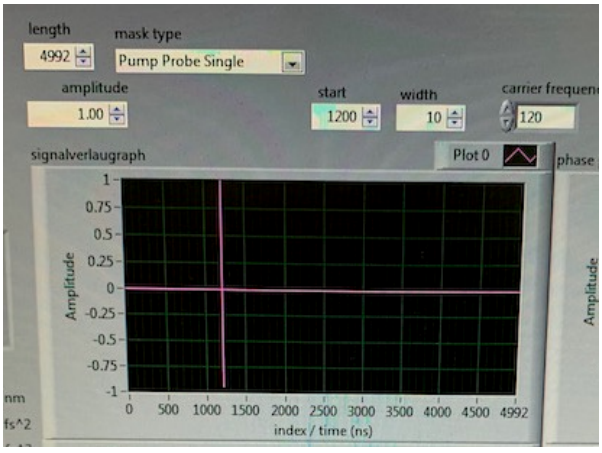

Figure C1. The pump-probe mask used for the reference measurement.

3. Apply a 2-frame mask sequence called “Pump-probe multiple.” The first mask has zero amplitude at all AWG pixels. The second mask creates windows of pixels with a user

defined width and user defined spacing of amplitude one across the AWG pixels. Typical widths and spacings are 10 and 200 respectively. An example of the multiple peak mask is shown in Figure B2. Measure both frames similarly to the reference. This measurement is referred to as the “calibration.”

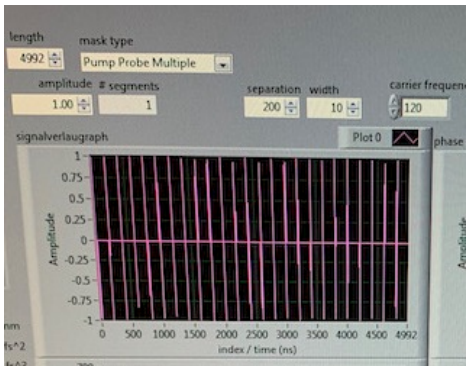

Figure C2. The pump-probe mask used for the calibration measurement.

4. Once the reference and calibration mask sequences have been measured, run the Matlab script “frequency_calibration.m” shown below.

```
%% load files
calfile = input('Calibration file name?','s'); %e.g. freq_cal_100_10_630_0.sprt
cal = load(calfile);
cal = squeeze(mean(cal,2));
cal = cal(1:1024);
reffile = input('Reference file name?','s'); %e.g. freq_ref_1000_10_630_0.sprt
ref = load(reffile);
ref = squeeze(mean(ref,2));
ref = ref(1:1024);

%% load wavelength axis
sep = input('Mask peak separation?'); %e.g. 100
refpx = input('Reference peak location?'); %e.g. 1000
wave = 439.0536+0.5622*(1:1024)-6.0854e-6*(1:1024).^2; %ensure spectrometer calibration is correct

%% plot and find peaks
figure(1)
plot(wave,cal,wave,ref)
title('pump spectrum')
xlabel('wavelength (nm)')
ylabel('intensity (au)')

height = input('Minimum peak height?'); %e.g. 3
distance = input('Minimum peak separation?'); %e.g. 4
cal_smooth = smooth(cal,'moving',5);
ref_smooth = smooth(ref,'moving',5);
%finds locations of the peaks in the calibration file
[peaks1 locs1] = findpeaks(cal_smooth(86:878),'minpeakheight',height,'minpeakdistance',distance);
%finds the location of the peak in the reference file, should only find one
%peak
[peaks2 locs2] = findpeaks(ref_smooth(86:878),'minpeakheight',height,'minpeakdistance',distance);
```

```
ref_diff = abs(locs1-locs2);
ref_index = find(ref_diff==min(ref_diff));
wavepeaks = wave(locs1+85);
freqpeaks = 299.792458./wavepeaks;
pix_left = refpx-sep*(ref_index-1):sep:refpx; %count peaks to left of reference peak
pix_right = refpx+sep:sep:refpx+sep*(length(peaks1)-ref_index); %count peaks to right of reference peak
pix = [pix_left pix_right];

%% fit peaks
figure(2)
plot(pix,freqpeaks)
title('aom calibration')
ylabel('frequency (PHz)')
xlabel('time (ns)')
params = polyfit(pix,freqpeaks,2);
```

5. Insert the calculated calibration parameters into the AWG LabVIEW program.

D. Flat spectrum fitting procedure

Fitting a white-light pulse to a flat spectrum is a quick procedure that requires one measurement of the white-light in the spectrometer, and a Matlab script. A flat spectrum white-light pulse is utilized in Chapter 5 for FTPT measurements to remove the need for deconvolution of the measured spectrum and the white-light spectrum.

1. Align the diffracted white-light into the spectrometer.
2. Use the mask sequence “Amplitude scan.” Set the “delay step” to 0.01 and the final delay to 1.00. The amplitude scan will create 100 masks with an amplitude of 0.01 to 1 in steps of 0.01.
3. In the LabVIEW program to operate the camera, change the number of masks to 100 in the “Camera controls full-sensor” tab. Make sure the phase-cycle switch is off.
4. Measure the amplitude scan and run the Matlab script “amplitude_scan_fit.m,” which is shown below. Before running the script, ensure that the spectrometer calibration, AOM calibration, flat spectrum window, and final file name are set correctly.

```
%% Plot amplitude scan
%load WL spectrum
clear all
close all
rawWL_spectrum = load("amp_scan_0.01_step_1_final_delay_scan_0_delay_0.sprt"); %insert file name
PxlWave = [448.8687 0.5149 4.6147e-5];%insert current spectrometer calibration
Camera_wave = PxlWave(1)+PxlWave(2)*(1:1024)+PxlWave(3)*(1:1024).^2;
WL_spectrum_amplitude = rawWL_spectrum(1:1024,:);
WL_spectrum_amplitude_smooth = smoothdata(WL_spectrum_amplitude,'movmean',7);
AmpStep = 0.01;
AmpArray = [AmpStep:AmpStep:1];
figure(1),pcolor(Camera_wave,AmpArray,WL_spectrum_amplitude_smooth') %plot full ampltidue array
shading flat, colorbar, colormap('jet')

%create AOM wavelength array
AOM_params = [3.1363e-9 -5.7073e-5 0.5927]; %from AOM calibration
AOM_index = [1:4992];
AOM_pixels_freq = polyval(AOM_params,AOM_index); %PHz
AOM_pixels_wave = 299.792458./AOM_pixels_freq; %nm
%interpolate WL to AOM and determine square pulse correction
for i = 1:length(AmpArray)
WL_spectrum_AOMaxis(:,i) = interp1(Camera_wave,WL_spectrum_amplitude_smooth(:,i),AOM_pixels_wave);
end

%choose flat spectrum window
WaveMin = 540; %nm
WaveMax = 710; %nm
[~,AOM_PixMinI] = min(abs(AOM_pixels_wave-WaveMin));
[~,AOM_PixMaxI] = min(abs(AOM_pixels_wave-WaveMax));
EndPoint_counts = [WL_spectrum_AOMaxis(AOM_PixMinI,100) WL_spectrum_AOMaxis(AOM_PixMaxI,100)];
minCounts = min(EndPoint_counts); %determine the counts each frequency will fit to


AOM_pix_amp = zeros(1,4992);
for i = AOM_PixMinI:AOM_PixMaxI
    [~,J] = min(abs(WL_spectrum_AOMaxis(i,:)-minCounts)); %find amplitude for each frequency to match "minCounts"
    AOM_pix_amp(i) = AmpArray(J);
end

AOM_pix_amp_smooth = smoothdata(AOM_pix_amp,'movmean',11);
AOM_pix_amp_smooth = AOM_pix_amp_smooth/max(AOM_pix_amp_smooth);
figure(2),plot(AOM_pixels_wave,AOM_pix_amp,AOM_pixels_wave,AOM_pix_amp_smooth,'LineWidth',2)
hold on
dlmwrite('AOM_square_pulse_compressed_540_710nm_20220809.dat',AOM_pix_amp_smooth,'\t'); %write the flat amplitude to a file
```

5. Load the flat spectrum file into the AWG program and check the “square pulse” setting to use the generated flat spectrum.